NTNU – Trondheim
Norwegian University of
Science and Technology

Denting of coated and uncoated offshore steel pipes

Nicolay Line Holm
Eivind Torgunrud Røshol

Department of Structural Engineering
Faculty of Engineering Science and Technology
NTNU- Norwegian University of Science and Technology
MASTER THESIS 2015

SUBJECT AREA:	DATE:	NO. OF PAGES:
Computational Mechanics	06.06.2015	14 + 102 + 4

TITLE: **Denting of coated and uncoated offshore steel pipes**
Inntrykking av offshore rørledninger med og uten isolasjonslag av polymer

BY:

Eivind Torgunrud Røshol and
Nicolay Line Holm

SUMMARY: In the present thesis, numerical and experimental investigations of coated offshore pipelines were conducted. The objective was to investigate how the polypropylene coating affected the global response of the pipes. The present work was a continuation of previous theses done on X65 steel pipes without coating, and part of an ongoing research program between SIMLab (NTNU) and Statoil.

The experimental work consisted of material testing and component tests. A tensile test of the X65 steel was conducted, along with a compression test of the PP foam from the coating. The component tests consisted of quasi-static denting of pipes with and without coating, and a compression test of the coating component consisting of all the layers combined.

Numerical simulations of all the tests were carried out with Abaqus/Explicit. A parameter study with a method called Factorial Design was conducted for the coating component. Dent depths of the bare steel pipes were estimated with the recommended practice, DNV-RP-111. Lastly, a new alternative model that takes the PP coating into account was proposed.

The experimental tests showed that for a given level of energy, the coated steel pipes had a significantly lower inner displacement compared to the pipes without coating. The material model for the PP foam underestimated the resistance of the coating.

The coating layer in the numerical model initially consisted of one layer based on the PP foam. The Factorial Design indicated that a numerical model including the inner and outer solid PP layers, would not yield a significantly higher resistance.

Numerical simulations of the coated steel pipes proved to be difficult. Large deformations in the coating layer lead to contact and distortion problems. The remeshing method ALE improved the simulation significantly, but did not solve the problems with the model entirely.

Estimations done on the bare steel pipes with DNV-RP-111 showed good correlation with the experiments, for a displacement up to 5-6% of the outer diameter. The proposed alternative model for the steel pipes with coating seemed to be a good start in exploring how polymer coating can be implemented in a recommended practice or standard.

Institutt for konstruksjonsteknikk
Fakultet for ingeniørvitenskap og teknologi
NTNU- Norges teknisk- naturvitenskapelige universitet

MASTEROPPGAVE 2015

TITTEL:

Inntrykking av offshore rørledninger med og uten isolasjonslag av polymer

Denting against coated and uncoated offshore steel pipes

UTFØRT AV:

Eivind Torgunrud Røshol og
Nicolay Line Holm

SAMMENDRAG: Numeriske og eksperimentelle undersøkelser av støt mot offshore stålrør med og uten et isolasjonslag laget av polypropylen (PP) er presentert i denne avhandlingen. Hensikten var å undersøke hvordan isolasjonslaget påvirket den globale responsen av rørene. Oppgaven er en videreføring av tidligere masteroppgaver skrevet om X65 stålrør, og er en del av pågående forskning mellom SIMLab (NTNU) og Statoil.

Arbeidet besto av å gjennomføre materialtester og komponenttester. Materialtestingen bestod av en strekkprøve av X65 stålet og en trykkprøve av det midterste skumlaget i isolasjonslaget. I komponenttestene, ble rør med og uten isolasjonslag utsatt for en kvasistatisk inntrykking. Det ble også gjennomført trykkprøver av det totale tverrsnittet av isolasjonslaget.

De numeriske simuleringene ble utført i Abaqus. En parameterstudie, kalt "Factorial Design" ble utført på en komponent av isolasjonslaget. Et estimat av den indre deformasjonen ble gjennomført ved hjelp av den anbefalte praksisen fra Det Norske Veritas, DNV-RP-111. En alternativ modell som tar hensyn til isolasjonslaget ble også foreslått.

De eksperimentelle forsøkene viste at rørene med isolasjonslag fikk en betraktelig mindre indre deformasjon sammenlignet med stålrørene, for en gitt mengde energi. Materialmodellen som ble etablert for isolasjonslaget undervurderte motstanden sammenlignet med forsøkene.

I de numeriske simuleringene var isolasjonslaget modellert som ett lag med materialegenskaper basert på kun det midterste skumlaget. Parameterstudien indikerte at en numerisk modell, som inkluderer de indre og ytre lagene, ikke ga en betraktelig høyere motstand mot inntrykking.

De numeriske simuleringene av rørene med isolasjonslag viste seg å være utfordrende. Store deformasjoner i isolasjonslaget førte til kontaktproblemer og problemer med elementer som ble forvrengt. En metode som genererer en ny mesh under simuleringene, ALE, forbedret simuleringene betraktelig. Metoden løste imidlertid ikke problemene fullstendig.

Estimeringen med DNV-RP-11 viste god korrelasjon opp mot eksperimentene på stålrørene uten isolasjonslag, frem til en ytre deformasjon som tilsvarer 5-6% av diameteren til røret. Den alternative metoden som ble foreslått kan virke som å være en god start i veien mot en modell som også kan inkludere isolasjonslaget i den analytiske beregningen.

FAGLÆRER:Tore Børvik

VEILEDER(E): Tore Børvik, Magnus Langseth, Martin Kristoffersen (NTNU). Mario Polanco-Loria (Statoil).

UTFØRT VED:SIMLab, Institutt for konstruksjonsteknikk, NTNU

MASTER'S THESIS 2015

for

Nicolay Line Holm og Eivind Røshol

Impact against coated and uncoated offshore steel pipes

1. INTRODUCTION

After discussions with Statoil and Gassco, a need for increased knowledge regarding behaviour, modelling and design of subsea constructions exposed to impact loading from e.g. trawl gear or falling objects has been identified. Metallurgical investigations have shown that fracture may initiate within the pipe wall the impacting object struck, making such fractures hard to discover – which in turn may result in severe economic and environmental consequences. In this master thesis, steel pipes will be tested quasi-statically and dynamically, with and without a polymer coating. The intention is to observe potential difference in behaviour due the loading being dynamic and due to the presence of the coating. Further, material testing of the steel and of the polymer coating will be conducted. This will be done in conjunction with advanced numerical simulations. Accurate numerical models will be an invaluable aid when predicting the deformation after an impact event.

2. OBJECTIVES

The main objective of the research project is to determine how coated and uncoated steel pipes behave under impact loading, and to validate to which extent this can be predicted using computational tools.

3. A SHORT DESCRIPTION OF THE RESEARCH PROJECT

The main topics in the research project will be as follows;

1. A literature review should be conducted to understand the pipe impact event, impact load design, testing facilities, constitutive modeling of metallic and polymer materials exposed to extreme loadings, and explicit finite element methods.
2. Specimens are extracted from the two materials (X65 steel and a polymer coating material) and tested in uniaxial tension and/or compression. Diameter reduction measurements are used to obtain mechanical properties of the materials.
3. Proper constitutive relations are chosen and calibrated based on the material tests.
4. The SIMLab Kicking Machine test facility will be used to expose the pipes to impact loading. The impact experiments will be used to investigate typical dynamic responses of the pipes.
5. Non-linear FE numerical simulations of the impact tests will be performed, and the numerical results shall be compared and discussed based on the experimental findings.
6. Estimations using DNV-RP-111 should be checked.

Supervisors: Tore Børvik, Martin Kristoffersen and Magnus Langseth (NTNU). Mario Polanco-Loria (Statoil).

The thesis must be written according to current requirements and submitted to the Department of Structural Engineering, NTNU, no later than June 10th, 2015.

NTNU, January 14th, 2015

Tore Børvik
Professor

Acknowledgment

Abstract

In the present thesis, numerical and experimental investigations of coated offshore pipelines were conducted. The objective was to investigate how the polypropylene coating affected the global response of the pipes. The present work was a continuation of previous theses done on X65 steel pipes without coating, and part of an ongoing research program between SIMLab (NTNU) and Statoil.

The experimental work consisted of material testing and component tests. A tensile test of the X65 steel was conducted, along with a compression test of the PP foam from the coating. The component tests consisted of quasi-static denting of pipes with and without coating, and a compression test of the coating component consisting of all the layers combined.

Numerical simulations of all the tests were carried out with Abaqus/Explicit. A parameter study with a method called Factorial Design was conducted for the coating component. Dent depths of the bare steel pipes were estimated with the recommended practice, DNV-RP-111. Lastly, a new alternative model that takes the PP coating into account was proposed.

The experimental tests showed that for a given level of energy, the coated steel pipes had a significantly lower inner displacement compared to the pipes without coating. The material model for the PP foam underestimated the resistance of the coating.

The coating layer in the numerical model initially consisted of one layer based on the PP foam. The Factorial Design indicated that a numerical model including the inner and outer solid PP layers, would not yield a significantly higher resistance.

Numerical simulations of the coated steel pipes proved to be difficult. Large deformations in the coating layer lead to contact and distortion problems. The remeshing method ALE improved the simulation significantly, but did not solve the problems with the model entirely.

Estimations done on the bare steel pipes with DNV-RP-111 showed good correlation with the experiments, for a displacement up to 5-6% of the outer diameter. The proposed alternative model for the steel pipes with coating seemed to be a good start in exploring how polymer coating can be implemented in a recommended practice or standard.

x

Contents

1 | Introduction

1.1 Background and Motivation

Offshore pipelines are used in huge amounts all over the world to transport oil and gas over vast distances. To ensure the flow in the pipe, the temperature has to be kept high to ensure low viscosity. Pipes coated with low density polypropylene offers not only insulation, but also mechanical resistance.

From time to time, pipelines are subjected to impact loads from falling objects from maintenance or installations, anchors or trawl gear. In November 2007, Statoil had to temporarily shut down the production after a pipeline at the Kvitebjørn oil field had been impacted and dragged approximately 56 m by an anchor [1]. Production was resumed in January 2008. However, a small leak was discovered in August 2008 and production was once again stopped immediately. The pipeline was repaired and ready for use in January 2009.

Accidents like the one at Kvitebjørn can lead to acute environmental damage and also huge economic losses. As a result, a research collaboration between the Structural Impact Laboratory, SIMLab at NTNU and Statoil was initiated.

At this point, six master's theses [2, 3, 4, 5, 6, 7] and one PhD thesis by M. Kristoffersen [8] have been written as part of this ongoing research program. They have thoroughly examined a wide range of parameters concerning impacts of bare steel pipes. There has been a focus on simulating the impact, hooking, pull-over and release [9] by using a pendulum acceleration and a bending machine. Different cases of loading and boundary conditions have been tested. Metallurgical investigations have been conducted and different parameters for a material model for the steel, including various fracture criteria have also been examined.

1.2 Outline of Thesis

This thesis has done experiments on coated pipes. The coating is a new factor and will consequently have the leading role throughout this study.

Chapter 2 presents a short introduction to the theory of materials mechanics, Digital Image Correlation (DIC) and Finite Element Analysis. This should give the reader the knowledge needed to understand the assumptions and decisions done in the thesis.

Chapter 3 consists of the preliminary studies conducted. A summary of the previous theses and information about the X65 steel is given. A study of the coating is also presented.

Chapter 4 elaborates on the material tests conducted on the coating and the steel.

Chapter 5 indicates how the material models used for numerical simulations are made and validated.

Chapter 6 is where the component tests are described and the results are presented. Quasi-static denting of pipes with and without coating was conducted together with a compression test on the full coating sandwich (all layers of the coating).

Chapter 7 presents a parameter study of the coating with a method called Factorial Design. Three parameters were examined. The hardening and yield strength of the PP foam in the coating were two quantitative parameters studied. The effect of modeling the coating with only one layer was the last qualitative parameter.

Chapter 8 lays out how the numerical models in Abaqus/Explicit were made, what problems occurred and the results of the simulations. The coating was the source of more numerical problems than expected.

Chapter 9 reviews how the DNV-RP-111 [9] (Det Norske Veritas Recommended Practice) can be used to estimated the dents depths of steel pipes from an impact. Only dents in bare steel pipe or steel pipes with stiff coating can be estimated through this model offered by DNV-RP-111. Therefore, an invented alternative model is provided. The alternative model is meant to start a discussion in how a new model can be implemented in a recommended practice or standard.

Chapter 10 ends this thesis by presenting discussions, some conclusions and recommendations for further work.

2 | Theory

Experimental testing, interpreting the results and reproducing the experiments by numerical simulations demand vast knowledge in the fields of structural analysis. The objective of this chapter is to give a basis of this knowledge so the reader can understand why certain choices and conclusions are made in this thesis.

The theory in this thesis consists of three parts. Materials mechanics and the digital image correlation (DIC) method are important in regard of understanding how the materials act and how the experiments should be analysed. Finite element analysis (FEA) theory is needed to understand the numerical simulations carried out.

2.1 Materials Mechanics

This thesis has tried not to get too entangled in the vast jungle of materials mechanics. However, a major part of understanding the simulations of coated pipes is the theory of plasticity, used to describe the irreversible deformations. Consequently the yield criterion, the plastic flow rule and the isotropic hardening are described in this section.

The theory is based on the compendium written for the course TKT4135 Materials Mechanics by Hopperstad and Børvik [10].

2.1.1 The Yield Criterion

The yield criterion describes whether the material deforms elastically or plastically. The transition between the elastic and plastic domain happens when the material has reached its initial yield limit, σ_0. This yield limit is described by the yield criterion as:

$$f(\boldsymbol{\sigma}) = 0 \tag{2.1}$$

where $f(\boldsymbol{\sigma})$ is the yield function. The material is in the elastic region when $f(\boldsymbol{\sigma}) < 0$. A state when $f(\boldsymbol{\sigma}) > 0$ introduces theory describing rate-depending plastic behaviour called viscoplasticity, but this state is assumed inadmissible for the materials used in

this thesis, implying that all plastic deformation takes place when $f(\boldsymbol{\sigma}) = 0$. These three states can be visualized in a two dimensional stress space as illustrated by Fig. 2.1. In the figure, $\boldsymbol{\sigma_1}$, $\boldsymbol{\sigma_2}$ and $\boldsymbol{\sigma_3}$ represent stress states in the elastic domain, the plastic surface, denoted the yield surface, and in the inadmissible region, respectively.
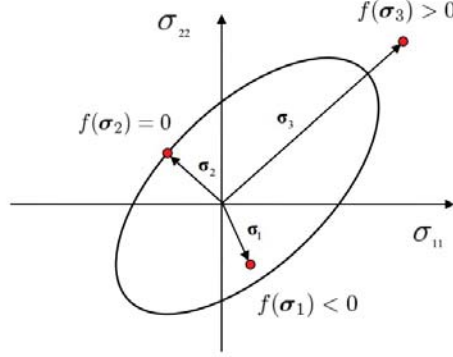
Figure 2.1: *Elastic domain, yield surface and inadmissible region [10].*

The yield surface may vary in shape depending on the yield criterion. In this thesis, von Mises yield criterion has been utilized as it is well incorporated in Abaqus/Explicit and widely used for isotropic materials.

von Mises Yield Criterion

The von Mises criterion assumes that the material is isotropic and pressure insensitive.

A convenient form to express the yield function is:

$$f(\boldsymbol{\sigma}) = \varphi(\boldsymbol{\sigma}) - \sigma_0 \tag{2.2}$$

where the equivalent stress $\sigma_{eq} = \varphi(\boldsymbol{\sigma})$ measures the magnitude of the stress state the material is subjected to. σ_0 is as defined earlier, the yield stress of the material. This is a material property, determined by mechanical experiments.

In the von Mises yield criterion, the yield function $f(\boldsymbol{\sigma})$, can be written in terms of principal stresses as:

$$f(\sigma_1, \sigma_2, \sigma_3) = \left(\frac{1}{2}\left((\sigma_1 - \sigma_2)^2 + (\sigma_2 - \sigma_3)^2 + (\sigma_3 - \sigma_1)^2\right)\right)^{\frac{1}{2}} - \sigma_0 \tag{2.3}$$

meaning that the equivalent stress for this criterion, denoted von Mises equivalent stress, σ_{eq}^m is expressed as:

$$\sigma_{eq}^m = \left(\frac{1}{2}\left((\sigma_1 - \sigma_2)^2 + (\sigma_2 - \sigma_3)^2 + (\sigma_3 - \sigma_1)^2\right)\right)^{\frac{1}{2}} \tag{2.4}$$

4

and thus, yielding occurs when

$$f(\sigma_1, \sigma_2, \sigma_3) = \sigma_{eq}^m - \sigma_0 = 0 \tag{2.5}$$

A graphical illustration of the von Mises yield surface, elastic domain and inadmissible region is given in Fig. 2.2.
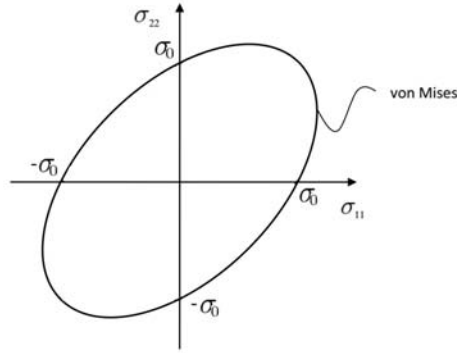
Figure 2.2: *Illustration of von Mises yield criterion[10].*

2.1.2 Plastic Flow Rule

Plastic deformation is an energy dissipative process. A dissipative process is irreversible, hence new energy is needed to reverse the plastic deformation. The plastic flow rule defines the plastic strain tensor $\dot{\varepsilon}_{ij}^p$ so that non-negative dissipation is ensured. In general, the plastic flow rule is defined by:

$$\dot{\varepsilon}_{ij}^p = \dot{\lambda} h_{ij} \tag{2.6}$$

where h_{ij} is the flow function, depending on the stress state of the material. $\dot{\lambda}$ is a non-negative scalar and denoted the plastic parameter. If it is assumed that h_{ij} is derived from a plastic potential function, and this function is defined by the yield function f, the plastic flow rule is called the associated flow rule and can be expressed as:

$$\dot{\varepsilon}_{ij}^p = \dot{\lambda} \frac{\partial f}{\partial \sigma_{ij}} \tag{2.7}$$

The associated flow rule implies that the incremental strain vector is normal to the yield surface and is therefore sometimes called the normality rule. The normality rule also implies that the shape of the yield surface determines the stress state *and* the direction of the plastic flow. Fig. 2.3 shows a graphical representation of the associated flow rule for the von Mises yield criterion used in this thesis.
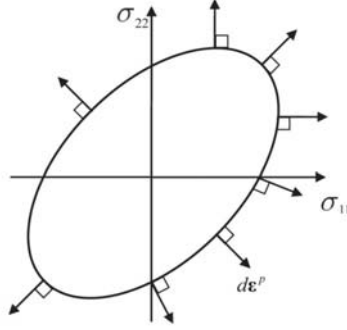
Figure 2.3: *Graphical representation of the associated flow rule for the von Mises yield criterion [10].*

Equivalent Plastic Strain

The equivalent plastic strain p (denoted PEEQ in Abaqus/Explicit), sometimes called accumulated plastic strain because it is monotonically increasing, is important regarding the loading history. If $\dot{p} = \dot{\lambda}$ is assumed, the equivalent plastic strain can be expressed as:

$$p = \int_0^t \dot{p} \, \mathrm{d}t = \int_0^t \dot{\lambda} \, \mathrm{d}t \qquad (2.8)$$

2.1.3 Isotropic Hardening

Isotropic hardening is the increase of the elastic domain due to plastic deformation. This increase comes from the dislocation density of the material. Mathematically, a isotropic hardening variable, R, is implemented in the yield criterion and the criterion can be expressed as:

$$f(\boldsymbol{\sigma}, R) = \varphi(\boldsymbol{\sigma}) - \sigma_y(R) = \sigma_{eq}(\boldsymbol{\sigma}) - [\sigma_0 + R(p)] \qquad (2.9)$$

where R is a function depending on the accumulated plastic strain p and σ_y is the flow stress. Fig. 2.4 shows how the elastic region is enlarged during plastic deformation from the increase of R and thus the flow stress σ_y.

Isotropic hardening means the elastic domain is equally expanding in all direction in the stress space. This implies that plastic deformation due to compression gives a higher yield stress in tension.

Two common ways to estimate the isotropic hardening are through the Power Law or Voce Rule, however in this thesis, tabulated values directly from the experiments were used.

Kinematic hardening is another hardening mechanism which is related to loading cycles. One example of this is when a material is first subjected to compression and then
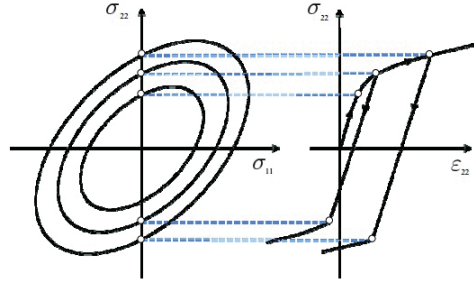
Figure 2.4: *Expansion of the yield surface from isotropic hardening [10].*

tension. Since this is not the case of this thesis, kinematic hardening will not be discussed any further.

2.1.4 Large Deformations

True stress and true strain

At large deformations the cross-sections of test specimens deform drastically. Engineering stress and strain are based on the initial gauge length or specimen length, L_0, and cross-section, A_0. Thus, engineering stress and strain are not able to describe the true behavior of the material. A more correct description of the behavior is with true stress, σ_t, and true strain, ε_t, from the following equations:

$$\sigma_t = \frac{F}{A} \tag{2.10}$$

$$\varepsilon_t = \int_{L_0}^{L} \frac{dL}{L} = ln\frac{L}{L_0} \tag{2.11}$$

where F is the applied force, A is the actual cross-section, L is the actual gauge or specimen length and L_0 is the initial gauge or specimen length. For metals, the volume is assumed to be preserved during plastic deformations. However, for polymers like the PP foam in this thesis, it is not always the case [11]. This will be discussed further in Chapter 5.

If preserving of the volume is assumed:

$$A_0 L_0 = AL \tag{2.12}$$

From this the true strain and true stress can be calculated, respectively, as:

$$\varepsilon_t = ln\frac{L}{L_0} = ln\left(\frac{L_0 + \Delta L}{L_0}\right) = ln(1 + \varepsilon_e) \tag{2.13}$$

$$\sigma_t = \frac{F}{A} = \frac{F}{\frac{A_0 L_0}{L}} = \frac{FL}{A_0 L_0} = \sigma_e \frac{L}{L_0} = \sigma_e (1 + \varepsilon_e) \qquad (2.14)$$

If the initial gauge length L_0 and cross-section area A_0 is known, and it is possible to measure the force F and the current cross-section A or the change in length ΔL, the true stress and true strain can be calculated.

2.1.5 Necking and the Bridgman Analysis

More about necking and the Bridgman Analysis can be found in the literature by Børvik [12], Dey [13] and Dieter [14].

Necking

Necking is an important aspect of the Bridgman Analysis and is therefore briefly explained in this section.

Physically, necking occurs when the increase of stress from the decrease in cross-section area becomes greater than the ability of the material to carry the load. More technically, when the ultimate tensile strength is reached in a test specimen, deformation becomes localized and the phenomena of necking occurs. This localized deformation introduce a triaxial stress state and the true stress estimated from Eq. (2.14) is higher than the stress that is required to cause flow [12].

Bridgman Analysis

To be able to calculate the stress beyond the maximum load, where necking occurs, this triaxial stress state needs to be corrected for. The mathematical model by Bridgman [14] is based on 4 assumptions:

- The neck has a contour approximated by the arc of a circle.

- The cross-section of the necked region remains circular throughout the test.

- The von Mises yield criterion applies.

- The strains are constant over the cross-section of the neck.

The equivalent stress after necking is expressed as:

$$\sigma_{eq} = \frac{\sigma_t}{(1 + \frac{2R}{a}) ln(1 + \frac{a}{2R})} \qquad (2.15)$$

and Le Roy's empirical model [15] yields:

$$\frac{a}{R} = 1.1(p - \varepsilon_{lu}^p) \qquad (2.16)$$

where ε_{lu}^p is the plastic strain at necking [12] and p is the equivalent true strain. The parameters a is the radius of the current cross-section. R is the radius of the curvature at the neck. Illustration of this can be seen in Fig. 2.5
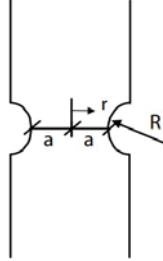
Figure 2.5: *Sketch of necked specimen [4].*

The triaxial stress state σ^* is given as:

$$\sigma^* = \frac{\sigma_H}{\sigma_{eq}} \tag{2.17}$$

where σ_H is the hydrostatic stress and σ_{eq} is the equivalent stress. The hydrostatic stress is defined as the mean principal stress. Dey has shown that the initial triaxilality ratio at the center of the notched specimen, i.e. the maximum value when $r = 0$, is given as [13]:

$$\sigma_{eq}^* = \frac{1}{3} + ln\left(1 + \frac{a}{2R}\right) \tag{2.18}$$

A typical result from a Bridgman correction is illustrated in Fig. 2.6.
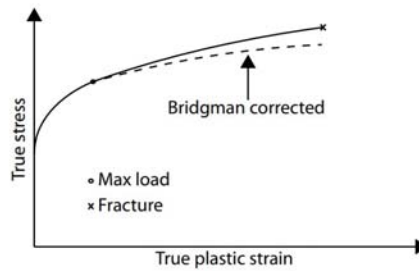
Figure 2.6: *True stress - true plastic strain with a Bridgman corrected curve [4].*

2.2 Digital Image Correlation

This brief introduction to DIC is based on two articles by Fagerholt et al. [16, 17].

The DIC method is basically a point tracker. The algorithm tracks a specific point on the test specimen through a series of images. This is made possible by painting a specimen with a speckled pattern as indicated in Fig. 2.7a. DIC finds the correlation between these images by tracking the pattern as it deforms.
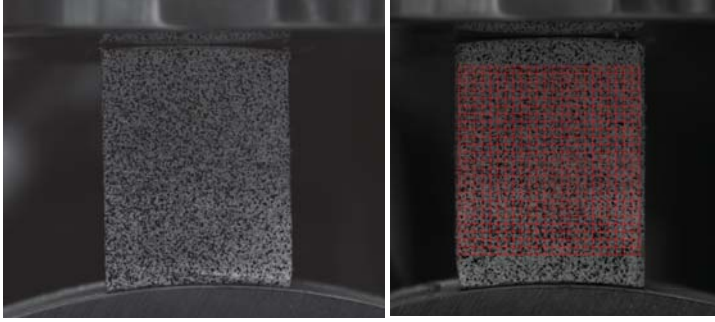
(a) *The characteristic speckled pattern*   (b) *Finite Element Mesh for DIC*

Figure 2.7: *DIC speckled pattern and FE mesh.*

More technically, the traditional way to find this correlation is by minimizing the sum of the grey-scale difference between two images within a particular local pixel subset [17]. However, a global correlation can be found for a set of nodes in a finite element mesh [16], see Fig. 2.7b. Nodal displacement is found by minimizing the gray-scale residual in the mesh region. From nodal displacements the displacement fields can be estimated. From this it is possible to calculate strain fields.

2.3 Finite Element Analysis

This chapter gives a brief introduction and presentation of the Finite Element Method Theory. The numerical simulations were performed in Abaqus/Explicit. The following section is mostly based on the following references [18], [19] and the lecture notes from Mathisen [20].

2.3.1 Dynamic Equilibrium

The general equation of motion for a system with multiple degrees of freedom may be

$$\{\mathbf{R}^{ine}(t)\} + \{\mathbf{R}^{dmp}(t)\} + \{\mathbf{R}^{int}(t)\} = \{\mathbf{R}^{ext}(t)\} \tag{2.19}$$

The inertia force vector can be expressed by the mass matrix and the nodal point accelerations.

$$\{\mathbf{R}^{ine}(t)\} = [\mathbf{M}]\{\ddot{\mathbf{D}}(t)\} \tag{2.20}$$

The damping force vector representing the energy dissipation in the system may be expressed by the damping matrix and the nodal point velocities:

$$\{\mathbf{R}^{dmp}(t)\} = [\mathbf{C}]\{\dot{\mathbf{D}}(t)\} \tag{2.21}$$

The internal force vector may be expressed by the stiffness matrix and the nodal point displacements.

$$\{\mathbf{R}^{int}(t)\} = [\mathbf{K}]\{\mathbf{D}(t)\} \tag{2.22}$$

The equation of motion may then be written in terms of:

$$[\mathbf{M}]\{\ddot{\mathbf{D}}(t)\} + [\mathbf{C}]\{\dot{\mathbf{D}}(t)\} + [\mathbf{K}]\{\mathbf{D}(t)\} = \{\mathbf{R}^{ext}(t)\} \tag{2.23}$$

This equation of motion can be solved by using either an implicit or explicit method. The explicit method was chosen for the simulations in this thesis. Although the method is conditionally stable, meaning that it requires a very small time step, it has several advantages that is suitable for the simulations that are done in thesis. These being:

- Equation solving is not necessary

- Equilibrium iterations not necessary

- Contact better taken care of

- Usually reliable for problems involving discontinuous nonlinearities

These advantages made the explicit method preferable.

2.3.2 Explicit Direct Integration

The expression for the equation of motion, Eq. (2.22), can be solved by using the method of central differencing. For simplicity, the following theory will be derived from a single degree of freedom system. Taking a Taylor series expansion of the displacement u_{n+1} and u_{n-1} about the time t_n yields:

$$u_{n+1} = u_n + \Delta t \, \dot{u}_n + \frac{\Delta t^2}{2} \, \ddot{u}_n + \frac{\Delta t^3}{6} \, \dddot{u}_n + \ldots \tag{2.24}$$

$$u_{n-1} = u_n - \Delta t \, \dot{u}_n + \frac{\Delta t^2}{2} \, \ddot{u}_n - \frac{\Delta t^3}{6} \, \dddot{u}_n + \ldots \tag{2.25}$$

Subtracting Eq. (2.25) from Eq. (2.24) and neglecting the higher order terms, an approximate equation for the velocity is obtained:

$$\dot{u}_n = \frac{u_{n+1} - u_{n-1}}{2\Delta t} \tag{2.26}$$

Similarly, adding the two equations together yields an approximation for the accelera-

tion.

$$\ddot{u}_n = \frac{u_{n+1} - 2u_n + u_{n-1}}{\Delta t^2} \tag{2.27}$$

Substituting these equations into the equation of motion and collecting all terms containing u_{n+1} on the left hand side yields:

$$\left(\frac{m}{\Delta t^2} + \frac{c}{2\Delta t}\right) u_{n+1} = P_n - \left(\frac{m}{\Delta t^2} - \frac{c}{2\Delta t}\right) u_{n-1} - \left(k - \frac{m}{\Delta t^2}\right) u_n \tag{2.28}$$

In a multiple degree of freedom system.

$$\left(\frac{1}{\Delta t^2}[\mathbf{M}] + \frac{1}{2\Delta t}[\mathbf{C}]\right) \{\mathbf{D}\}_{n+1} = \{\mathbf{R}^{ext}\}_n - \left(\frac{1}{\Delta t^2}[\mathbf{M}] + \frac{1}{2\Delta t}[\mathbf{C}]\right) \{\mathbf{D}\}_{n-1} - \left([\mathbf{K}] - \frac{1}{\Delta t^2}[\mathbf{M}]\right) \mathbf{D}_n \tag{2.29}$$

As can be seen from Eq. (2.29), there are two matrices on the left hand side. Unless the mass and damping matrices are diagonal, the effective stiffness matrix has to be factorized to obtain the displacements. Utilizing a lumped mass matrix and a damping that corresponds to a mass proportional damping yields matrices with entries solely along the diagonal. Hence, the displacements may be computed efficiently. However, mass-proportional Rayleigh damping damps out mainly the lower modes. This may lead to a dynamic response with high-frequency numerical noise [20].

A method that yields a solution where only the mass matrix ends up on the left hand side can be utilized. This is done by establishing the approximations used above with the velocity lagging half a step. Without further elaborating the derivation of this, the following equation of motion yields from using this improved central differencing approximation:

$$m \ddot{u}_n + c \dot{u}_{n-^1/_2} + k u_n = P_n \tag{2.30}$$

$$\frac{m}{\Delta t^2} u_{n+1} = P_n - k u_n + \frac{m}{\Delta t^2} \left(u_n + \Delta t \dot{u}_{n-^1/_2}\right) - c \dot{u}_{n-^1/_2} \tag{2.31}$$

Similarly, for a multiple degree of freedom system:

$$\frac{1}{\Delta t^2}[\mathbf{M}]\{\mathbf{D}\}_{n+1} = \{\mathbf{R}^{ext}\}_n - [\mathbf{K}]\{\mathbf{D}\}_n + \frac{1}{\Delta t^2}[\mathbf{M}](\{\mathbf{D}\}_n + \Delta t\{\dot{\mathbf{D}}\}_{n-^1/_2}) - [\mathbf{C}]\{\dot{\mathbf{D}}\}_{n-^1/_2} \tag{2.32}$$

In the first step when $n = 0$, some initial calculations have to be done to be able to calculate the displacements at $n = 1$. The velocity in step $n = -^1/_2$ can be calculated by using a backward difference approximation:

$$\{\dot{\mathbf{D}}\}_{-^1/_2} = \{\dot{\mathbf{D}}\}_0 - \frac{\Delta t}{2}\{\ddot{\mathbf{D}}\}_0 \tag{2.33}$$

By solving the equation of motion at time t_0, an approximation for the acceleration can be obtained as well:

$$\{\ddot{\mathbf{D}}\}_0 = [\mathbf{M}]^{-1}(\{\mathbf{R}^{ext}(t)\}_0 - [\mathbf{K}]\{\mathbf{D}\}_0 - [\mathbf{C}]\{\dot{\mathbf{D}}\}_0) \tag{2.34}$$

2.3.3 Stability and Accuracy

The primary error term is proportional to Δt^2. This is due to the fact that in the Taylor series expansion in the previous derivation, terms containing Δt to the power higher than second order are neglected. This leads to a second-order accuracy for the displacement.

The central difference scheme is conditionally stable. This means that the time step Δt has to be lower than the stable time increment Δt_{cr}. If this condition is not satisfied, the solution gets unstable and this will lead to oscillations in the response history.

For practical problems the critical stable time increment can be expressed in terms of the damping ratio ξ, and the highest natural frequency ω_{max}.

$$\Delta t_{cr} \leq \frac{2}{\omega_{max}} \left(\sqrt{1 - \xi^2} - \xi \right) \tag{2.35}$$

For an undamped material:

$$\Delta t_{cr} \leq \frac{2}{\omega_{max}} = \frac{L}{c_d} \tag{2.36}$$

Where L is the length of the smallest element in the mesh and c_d is the speed of sound in the material, the dilatational wave speed. This speed is dependent on the Young's modulus E and the mass density ρ.

$$c_d = \sqrt{\frac{E}{\rho}} \tag{2.37}$$

From Eq. (2.36) it can be seen that length of the smallest element, combined with the density and stiffness of the material are the parameters that affect the stable time increment. It is therefore important that the mesh does not contain an element that is significantly smaller than the other elements, as this will make the stable time increment small for the entire model.

Since the frequency is in the denominator in Eq. (2.36), a high frequency will lower the stable time increment. Higher order elements should therefore be avoided as they have higher frequencies than lower order elements.

2.3.4 The Arbitrary Lagrangian-Eulerian Formulation

The coating will undergo large deformations. In the numerical simulations, this may lead to a mesh of distorted elements. One way to remedy this problem can be to use the Arbitrary Lagrangian-Eulerian (ALE) formulation. It combines the Lagrangian formulation and the Eulerian formulation. The former is where a specific point of the material corresponds one-to-one with the mesh. The latter formulation is where the material flows through a fixed mesh. Both formulation and the combined one is showed in Fig. 2.8. Further description of the ALE formulation can be found in M. Kristoffersen [8].
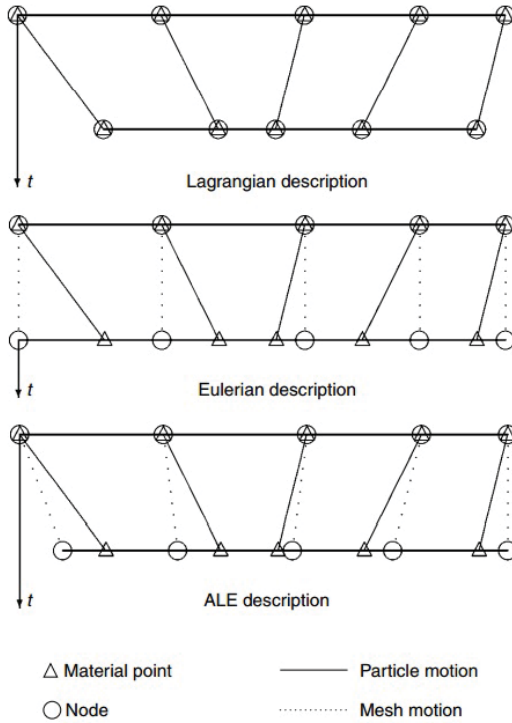
Figure 2.8: *Example of Lagrangian mesh, Eulerian mesh, ALE mesh and particle motion [8].*

In practice, ALE is a technique were a new smoother mesh is created by sweeping and relocating nodes iteratively over an adaptive mesh domain [21]. The purpose is to reduce element distortion. An example of the effect of ALE can be seen in Chapter 8, Fig. 8.10.

Three parameters may be varied using this formulation:

- The number of *initial mesh sweeps* in the first step ALE is active.

- The *number of sweeps* in each adaptive meshing increment.

- The *frequency* is at what number of increments in the simulations the adaptive meshing will be performed.

2.3.5 Contact

The theory in this section is taken from various places in the literature [22, 21, 23, 20].

Contact Algorithms

Abaqus/Explicit offers two contact algorithms: General contact makes it possible to define contact between all the regions of the model with one interaction as demonstrated in Fig. 2.9a. With contact pairs it is needed to define contact between the surfaces, see Fig. 2.9b.
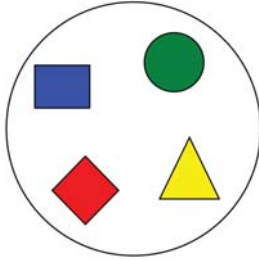
(a) *One contact domain in general contact [22]*   **(b)** *Multiple contact pairs [22]*
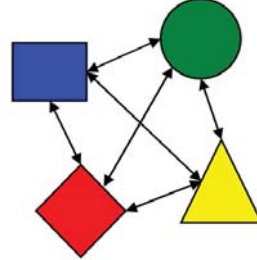
Figure 2.9: *The two different contact algorithms in Abaqus/Explicit.*

The two contact algorithms provide and demand some different properties. General contact is usually a bit faster and recommended for models with complex geometry. However, it can not be used with the kinematic constraint or ALE, which is discussed further in Chapter 8. Contact pairs is recommended in cases where specific contact features are desired. It is also needed if the analysis is dependent on the use of the ALE technique.

General contact and contact pairs may be used together. General contact then avoids processing interactions defined by the contact pairs.

Contact Constraints

The large and sudden change in the stiffness matrix when two or more bodies make contact is solved with different contact constraints. The two provided by Abaqus/Explicit are the penalty constraint method and the kinematic constraint method.

The penalty method is usually the preferred method. It leaves the number of unknowns constant in an explicit analysis, thus no additional equation solving is needed. It is also better suited for contact involving rigid bodies and it is the only one that can model rigid-to-rigid contact. However, the kinematic method provides a more stringent enforcement of the contact constraint than the penalty method.

The penalty method was the initial method in this thesis. It imposes the contact conditions by augmenting the potential energy of the system, by a penalty term. For the single degree of freedom system in Fig. 2.10 the contact formulation is deduced in the equations that follow.
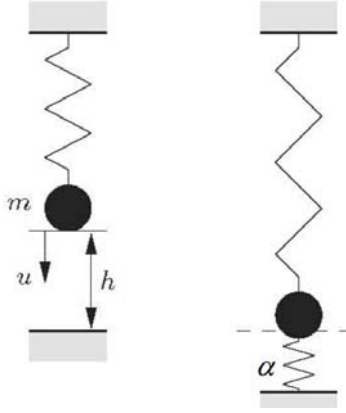
Figure 2.10: *Single degree of freedom spring system [20].*

$$\Pi_p^* = \Pi_p + \underbrace{\frac{1}{2}\alpha[C(u)]^2}_{\text{Penalty term}} = \frac{1}{2}ku^2 - mgu + \frac{1}{2}\alpha[C(u)]^2 \tag{2.38}$$

The parameter α can be interpreted as a spring stiffness in the contact interface, due to the fact that the energy expression for the penalty term is on the same form as the energy equation for the spring. For the solution to be stationary, the change in potential energy with respect to the displacement has to be equal to zero. Hence, the following equation has to be satisfied and yields the following expression for the displacement.

$$\left\{ \frac{\partial \Pi_p^*}{\partial u} \right\} = 0 \quad \Rightarrow \quad (k + \alpha)u = mg + \alpha h \tag{2.39}$$

$$u = \frac{mg + \alpha h}{k + \alpha} \tag{2.40}$$

The contact force occurs when the displacement u is bigger than h. It may be written as:

$$C(u) = u - h = \frac{mg - kh}{k + \alpha} \tag{2.41}$$

The contact force, expressed as λ, equals the interface spring force in the system.

$$\lambda = \alpha C(u) = \frac{\alpha}{(k + \alpha)}(mg - kh) \tag{2.42}$$

The penalty parameter, α, plays an important role. There are two limiting cases that can be distinguished. A very large parameter yields a very large penalty spring stiffness. This means that the penetration into the rigid surface will be small, and can also lead to an

ill-conditioned stiffness matrix. On the other hand, a very small penalty parameter will yield a large penetration into the rigid surface. This extremity is only valid in the case of no contact, since the contact equation, Eq. (2.41), is not satisfied sufficiently.

2.3.6 Locking

Fully integrated first order elements may behave overly stiff in bending applications [18]. This phenomenon is called locking. Two different types of locking will be briefly explained in this next section.

Shear locking

This section is written based on theory presented in [18]. Fig. 2.11 shows how the deformation of a material subjected to a bending moment M should be. Lines initially parallel to the horisontal axis get a constant curvature, and the angle between the initially perpendicular lines remain at 90°.
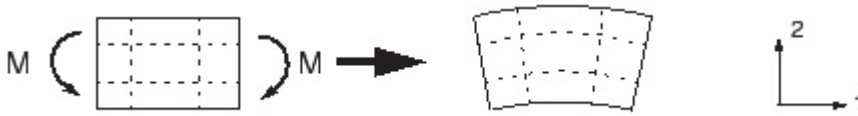
Figure 2.11: *Deformation of material subjected to a bending moment M [18].*

However, in a linear element, the edges are unable to curve and the material deforms as shown in Fig. 2.12.

Figure 2.12: *Deformation of a linear element subjected to a bending moment, M [18].*

Using a full integration scheme on this sort of problem introduces an increased artificial stiffness contribution. Since the edges of the element are unable to curve, the upper line has to increase in length, whereas the length of the lower curve has to decrease. This is generally unproblematic as this is consistent with the expected state of stress of a small piece subjected to bending. It can be seen that σ_{11} is compressive at the bottom and in tension at the top. However, at each integration point the angle between the vertical and horizontal lines has changed. This indicates that σ_{12}, the shear stress, is nonzero. An element in pure bending has zero shear stress. This effect is called shear locking.

Volumetric Locking

Volumetric locking is another type of locking problem that occurs when using a fully integrated linear element, subjected to bending. The element is not able to bend without changing the volume at each integration point. Looking at a case of pure bending in the thickness direction, a linear field of normal strains will be present in the element. To compensate for this field, a linear field has to be created in the perpendicular direction. However, the fully integrated element is not able to create this. The element is not able to represent bending, without also changing the volume. This will introduce and additional stiffness that will have a magnitude dependent on the Poisson ratio.

2.3.7 Hourglassing

To address these types of artificial stiffness contributions, reduced integration is employed. Having an integration point in the center of the element, leads to no change in angle, which was the problem that introduced artificial shear stress. The linear field of normal strains associated with the volumetric locking, is also taken care of by having the integration point placed in the middle. In addition to adressing the locking problem, the reduced integration element also increases the computational efficiency substantially. However, it has its own numerical difficulties that leads to errors, a phenomona called hourglassing.
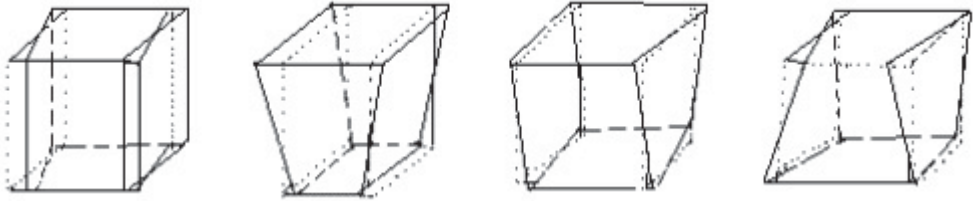
Figure 2.13: *Examples of hourglass modes [24].*

Fig. 2.13 demonstrates four different hourglass mode examples. Since the reduced integration elements only have one integration point in the middle, some deformations may cause the middle point to neither move or rotate, leading to zero normal stresses and zero shear stresses. It has no contribution what so ever to the strain energy and if this effect is not controlled it can lead to results that can not be used. These modes can also propagate and thus include several elements giving this a even bigger error on the global response. Abaqus/Explicit has several ways to discover and control these hourglass modes. The integral viscoelastic form of hourglass control is the default form on all reduced integration elements.

The Abaqus documentation [19] defines the viscoelastic approach as the following.

Let q be an hourglass mode magnitude and Q be the force or moment conjugate to Q. The integral may be defined as:

$$Q = \int_0^t sK(t)(t-t')\frac{\mathrm{d}q}{\mathrm{d}t'}\,\mathrm{d}t' \qquad (2.43)$$

where K is the hourglass stiffness selected by Abaqus/Explicit, and s consists different scaling factors. These factors are dimensionless and can relate to specific displacement degrees of freedom.

- s^s for solid and membrane elements, scales all hourglass stiffnesses.

- s^s for shell elements, scales hourglass stiffnesses related to the in-plane displacement degrees of freedom.

- s^r scales the hourglass stiffnesses related to the rotational degrees of freedom.

- s^w for small strain elements, scales the hourglass stiffness related to the transverse displacement for small-strain shell elements.

By default all these factors are set to 1.0.

2.3.8 Energy Balance

Ensuring that the solution is obtained using a sufficiently small time step, does not necessarily assure that the solution obtained is physically meaningful. Comparing the numerical simulations with the experiments conducted in the laboratory, may not be sufficient to ensure that the numerical model is valid. In addition to the comparison with the experiments, an energy balance check is conducted.

An energy balance for the entire model may be written as [25]:

$$E_K + E_{SE} + E_{PD} + E_{AE} + E_{VD} + E_{FD} - E_{WK} - E_{PW} - E_{CW} = E_{TOT} = Constant \quad (2.44)$$

Where the different energy denotations is summarized in Table 2.1.

Table 2.1: *Table explaining the different energy denotations [25].*

Energy quantities	
E_K	Kinetic energy
E_{SE}	Elastic strain energy
E_{PD}	Energy dissipated through plastic work
E_{AE}	Artificial strain energy
E_{VD}	Energy dissipated through viscous damping
E_{FD}	Energy dissipated through friction
E_{WK}	Work done by external forces
E_{PW}	Work done by contact penalties
E_{WK}	Work done by constraint penalties
E_{TOT}	Total energy

3 | Preliminary Studies

A preliminary study was conduced to get an introduction to the problem, and to get useful insight in the different obstacles that might occur. First, a summary of the previous masters theses and the doctoral thesis by M. Kristoffersen [8] on impact of X65 steel pipes are presented. Then two studies concerning the two essential parts of the pipes tested, namely the X65 steel and the coating.

3.1 Previous Work

3.1.1 Summary of Previous Theses

The first thesis written at SIMLab about the impact against X65 steel pipes was done by Slåttedalen and Ørmen [2]. An impact test in the kicking machine [26] was conducted to simulate an anchor interfering with the pipe. The pipes were impacted and then stretched back to their initial configuration. The simulation was found to correlate sufficiently with the global response. However, a finer mesh was needed to simulate the fracture. The material model did not include kinematic hardening and was recommended to be investigated further.

The same impact test was conducted on empty and water-filled pipes by Fornes and Gabrielsen [3]. The pipes were filled with water to study the effect of internal content. Kinematic hardening was investigated and included in the material model. The tests revealed a slightly higher force level on the filled pipes. However, it was uncertain if this was caused by the higher thickness in the pipe wall.

In the subsequent thesis by Hovdelien and Aune [4], the same tests were conducted with the objective of examining the microstructural behavior of pipes exposed to a complex stress rate. The incipient fracture was investigated. A more extensive material model that included kinematic and isotropic hardening was created. However, it yielded little improvement from the previous thesis.

Asheim and Mogstad [5] conducted experiments on three pipes. Two different tests in a bending rig were done, both with and without applied axial load. The numerical simulations of the pure bending was replicated with a good correlation. However,

stretching the pipes back to their initial configuration did not correlate in a satisfactory manner.

As a continuation of Asheim and Mogstad [5] work, Jakobsen [6] conducted three different experiments in the stretch-bending rig. The first test was done without any axial load applied. Further, the last two pipes were stretched with a constant load and a linearly increasing load, respectively. The numerical results corresponded well with the experimental results, including comparing of plastic strains with strains from Digital Image Correlation (DIC).

Fracture has been found in pipes dynamically impacted, so Digerud and Lofthaug [7] conducted two quasi-static tests to investigate whether or not this formation of cracks (internal and external) could be found under the quasi-static conditions. No signs of fracture was found in the pipes tested quasi-statically.

3.1.2 X65 Steel Pipes

Unfortunately, no material certificate was provided. However, after conversations with the supplier of the pipe (Statoil), the steel was assumed to be of the X65 steel grade. The material tests conducted later in Chapter 4, indicated that this assumption may be valid.

Manes et al.[27] thoroughly analyzed pipes made from rolled and welded pipes with the API (American Petroleum Institute) steel grade X65, probably similar to the one used in this thesis. The process of making the welded pipes however, is different. The pipes in this study are made seamless, i.e without welding. A heated solid cylinder is inserted between two rollers. Stresses induced by the rollers causes the center of the solid cylinder to fracture. The next step is to make the cylinder into a shell by piercing it with a plug. Then the shell is worked to meet the buyers' specifications in terms of diameter and thickness. This method is called the Mannesmann effect [28], and it may give different material properties compared to pipes made from welded plate strips. The previous master theses Slåttedalen and Ørmen [2], Hovdelien and Aune [4] and the doctoral thesis by M. Kristoffersen [8], conducted extensive material testing and found that the seamless pipes can be assumed isotropic and homogeneous in contrast to the welded pipes that indicated anisotropy.
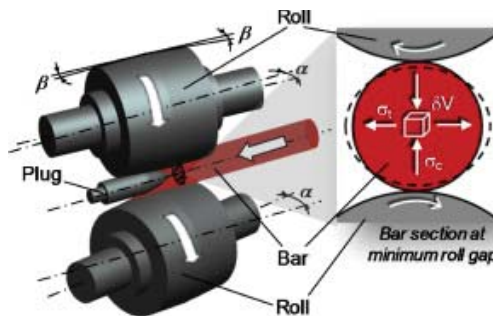

Figure 3.1: *The Mannesmann process [28].*

The X65 steel grade is one of the most popular steel grades in the oil and gas industry. Low cost, excellent weldability and high strength and ductility, makes it a good choice in an industry that uses extreme amounts of pipes x65 [29]. Material testing by M. Kristoffersen [8] found the nominal yield stress to be 478 MPa and the ultimate tensile strength to be 572 MPa. The Young's Modulus and Poisson ratio was found to be 208000 MPa and 0.3, respectively.

3.2 Study of the Coating

Coated pipes have not been studied in the previous masters theses nor the doctoral thesis by M. Kristoffersen [8]. It was therefore a natural focus point in this thesis. The coating layers are made of polypropylene. This is a polymer used in numerous applications including textiles, packaging, labeling, polymer bank notes and furniture. It can be manufactured in various ways, ending up with different densities and strength [30]. Experiments conducted on similar coating done by M.Polanco-Loria [31] showed that the polypropylene materials used in this thesis probably exhibit pressure sensitivity and anisotropy.

Information provided in this section comes from the websites of the two global providers of pipe coating solutions, Bredero Shaw [32] and Tenaris [33], and also from a visit at Bredero Shaw's factory in Orkanger, Norway.

The Coating Layers

The coating studied in this thesis, is a multi-layer solution called Thermotite®. The main purpose for this kind of coating solution is to provide thermal insulation for heated liquids. These pipes can operate within a temperature range of $-35°C$ to $150°C$ and can be used at depths up to 1000 m. The multi-layer solution also gives great anticorrosive and mechanical protection. The focus in this thesis, with regard to the coating, was the mechanical properties.

The multi-layer coating consisted of 5 different layers that are described in the list below and can be seen in Fig. 3.2.

1. The Fusion Bond Epoxy (FBE) is a powder coating mainly to provide anticorrosive protection.

2. Adhesive layer to create the adherence necessary between the first and third layer.

3. The main purpose of the solid polypropylene (PP) layer is to give anticorrosive and mechanical protection to the steel pipe. In a 3-layer solution, this would be the outer layer.

4. A layer of PP foam gives the best thermal insulation. This layer can be adjusted in terms of both mechanical properties and thickness.

5. The outer solid layer of PP shields the more porous PP foam.
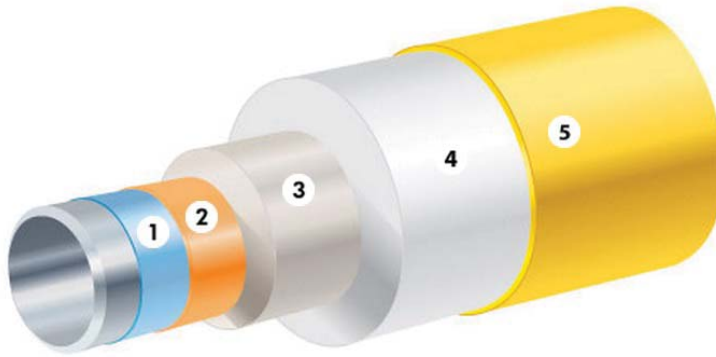
1. Fusion Bonded Epoxy 2. Adhesive 3. Solid PP 4. PP Insulation 5. Outer Shield

Figure 3.2: *The different layers of the coating [32].*

The Manufacturing Process

The coating was added to the pipes by Bredero Shaw at their factory in Orkanger, Norway. Bredero Shaw is a global manufacturer of pipe coating solutions for the oil, gas and water industries. They have factories spread over the world and more than 400.000 km ($\approx$ 10 times around equator) of pipelines are protected by their coating solutions.

A trip to the Bredero Shaw factory at Orkanger, was conducted by a group consisting of the two authors of this thesis, together with supervisor Martin Kristoffersen and two laboratory engineers at SIMLab, Tore Wisth and Trond Auestad. A guided tour at the manufacturing site was given by Senior Development Engineer at Bredero Shaw, Trond Schjelderup. This gave insight in how the coating is applied the steel pipes and how this process may affect the material properties of the coating.

The process follows the steps seen in Fig. 3.3 and can be divided in three steps, or physically, three lines of production. The pipes are always rotating while they are in the coating production lines.

A recapitulation of the steps on how the coating is applied:

- Pipes are preheated and cleaned for corrosion by abrasive blasting. Surface defections are fixed before a visual inspection is carried out.

- They are heated up to 220-230 °C so that the FBE powder coating melts and covers the whole surface including the pores. The adhesive layer and the inner solid PP layer is stretched around while the pipes are still hot. This process has a line speed of 2 m/min and can produce around 900-1000 kg of plastic per hour.

- On the last line of production, the PP foam and and the outer shield layer are added by two nozzles that encircle the pipes. The PP foam and shield layer holds a temperature of about 200 °C and is cooled down by water. The line speed is between 150-300 mm/min depending on the thickness of the PP foam added. Lastly, an electrical inspection makes sure the pipes have no flaws in the coating.
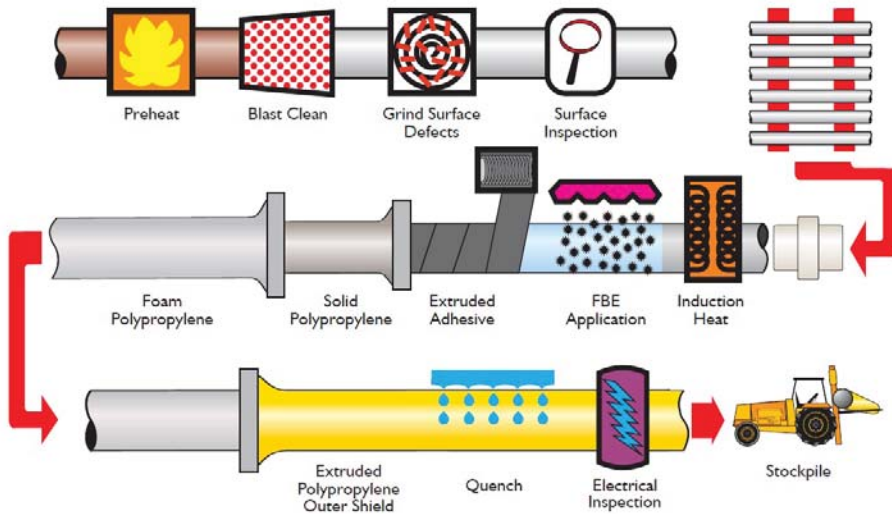
Figure 3.3: *The process of adding coating to the steel pipes [32].*

When production is done, the pipes leave the factory to be joined together (a process not discussed in this thesis) before being rolled up and shipped out.

A section of both pipe *S* and *L* is presented in Fig. 3.4. As seen in this figure, the coating for pipe *S* consisted of one layer of PP foam and one outer shield layer. With increased thickness in the warm PP foam, more mechanical issues will arise. This is mostly due to the creep while the PP foam cools down, and it may disturb the material properties. For this reason, pipe *L* consisted of two of these layers. This means that the pipe *L* has gone through the process of adding PP foam and the shield layer one more time after the first layer cooled down.
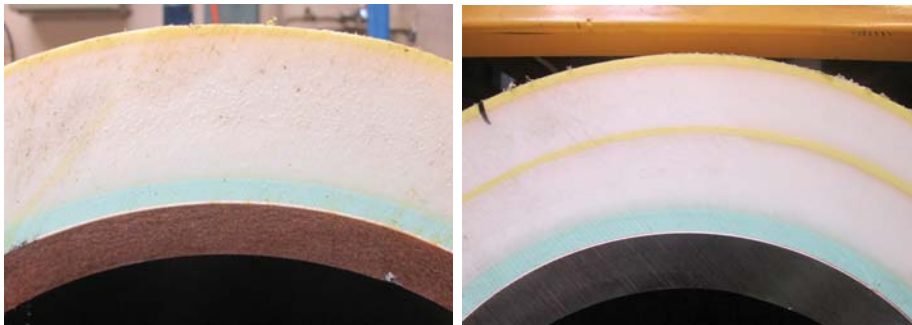
(a) *Pipe S has one layer of PP foam*   **(b)** *Pipe L has two layers of PP foam*

Figure 3.4: *The two different coated pipes supplied by Statoil.*

The material properties of different coated pipes vary from various reasons. The thickness of the PP foam and the surrounding temperature in the factory vary, making the cooling time alter and the creep differ. The pipes are also rotating throughout the pro-

cess and this can create some anisotropy in the coating. It was therefore not expected to find the same material properties in the PP foam from pipe S and L. This was later confirmed by the material tests, see Chapter 4.

4 | Material Testing

The objective of the material test program was to characterise both the steel and the PP foam from the offshore pipelines provided by Statoil. Two different coated pipes was provided, one pipe denoted L and one smaller pipe denoted S. The steel has been widely tested in the previous work done on the X65 pipes and most of the effort was invested in characterizing the PP foam.

4.1 Measurements

(a) *Steel specimen*   **(b)** *PP foam specimens*
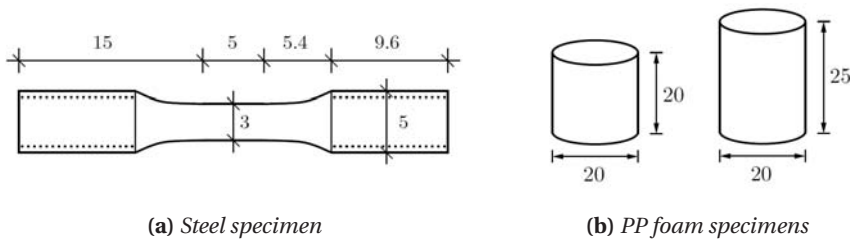
Figure 4.1: *The different specimens used in the tensile (steel) and compression (PP foam) tests of the respective materials. Measurements in mm.*

Axisymmetric specimens were cut out from the steel at four different positions (North, South, East and West) shown in Fig. 4.2. The specimens were cut out from both pipes, which makes eight specimens in total. The geometry of the steel specimens is shown in Fig. 4.1a.

Cylindrical specimens of the PP foam were cut out in the radial direction at two different positions. These are shown in Fig. 4.2. Two different height to diameter ratios were used. The two different geometries are shown in Fig. 4.1b. Three specimens of both heights were cut out from each of the two pipes. Eight of these were tested. Half of them were tested at an elevated initial strain rate. The Digital Image Correlation (DIC) technique was utilized.

It was of great importance that the PP foam specimens were cut out so that their main axis were in the radial direction of the pipe and coating. This was done so that mate-
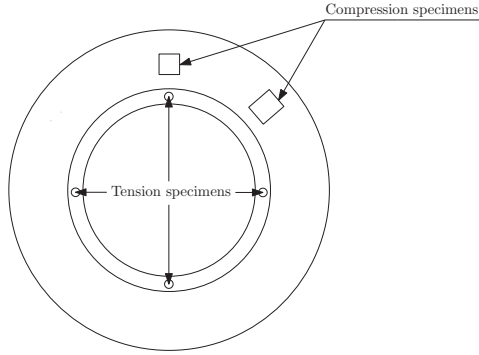
Figure 4.2: *Location of where the specimens were taken out.*

rial behavior would be comparable to what happened in the component tests. This is illustrated in Fig. 4.2.

4.2 Experimental Set-up

4.2.1 Steel Tensile Test

Quasi-static tests were conducted in a Zwick 30 kN stretching rig. As explained in the previous section, the test specimens were taken from different locations in both pipe *S* and pipe *L*. The specimens were stretched with a deformation rate of $\dot{u} = 0.15$ mm/min, corresponding to an initial strain rate of $\dot{\epsilon} = 5 \cdot 10^{-4}$ s^{-1}. The overview of the experimental test set-up is shown in Fig. 4.3a. The diameter reduction was measured by a laser that kept track of the smallest diameter in two orthogonal directions [34]. The laser set-up can be seen in Fig. 4.3b. This measurement made it possible to compute the true stress-true strain beyond necking. All of the specimens were initially ordered with a thickness of 3 mm, as shown in Fig. 4.1a. The specimens were grinded and polished to ensure a smooth surface for the laser measurements. Because of this, the specimens had a slightly narrower cross section, at about 2.88 mm. The lab technician conducting the test wiped off the specimens for the sake of removing small dust particles in the necking area.

(a) *Zwick 30kN testing machine overview*   (b) *Laser measurement*
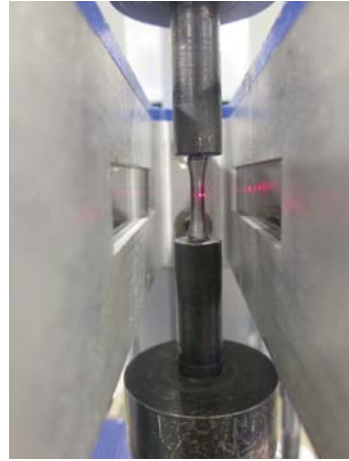
Figure 4.3: *Overview of the steel tensile test set-up.*

In Fig. 4.4 the test specimens are shown before and after fracture. The specimens had a cup-cone like fracture surface.

(a) *Initial test specimen*   (b) *After fracture*

Figure 4.4: *A specimen before and after fracture.*

4.2.2   PP Foam Compression Test

The compression tests were conducted on an Instron 100kN machine. The specimen was placed between two steel cones. To minimize the inevitable effects of friction, slick tape and lubricant were applied to both ends of the specimens. The experimental set-up is shown in Fig. 4.5b.

(a) *Initial test specimens*

(b) *Set-up of PP foam compression test*

Figure 4.5: *PP foam specimens and set-up of the compression test.*

Eight specimens were tested, four taken from pipe S and four taken from pipe L. The tests were carried out with different heights and deformation rates. The specific information about each specimen, including measured density, initial strain rate and the cross section area used in further calculations, can be seen in Table 4.1. A precision weighting scale was used to weigh the specimens. Along with logging force and displacement, the DIC technology was utilized with two cameras at different angles.

Table 4.1: *Information and measurements of the coating specimens.*

Specimen #	Pipe	Height [mm]	$\dot{u}$ [mm/s]	$\dot{\epsilon}$ [s^{-1}]	ρ [kg/m^3]	Area [mm^2]
1	S	20	1.2	10^{-3}	704	314
2	S	20	12	10^{-2}	704	314
3	S	25	12	$8 \cdot 10^{-3}$	717	314
4	S	25	1.2	$8 \cdot 10^{-4}$	710	314
5	L	20	12	10^{-2}	707	314
6	L	20	1.2	10^{-3}	748	314
7	L	25	1.2	$8 \cdot 10^{-4}$	734	314
8	L	25	12	$8 \cdot 10^{-3}$	759	314

4.3 Results

4.3.1 Steel

The results from the steel tensile tests are presented in Fig. 4.6. The tests from pipe S and pipe L are divided into two plots, each showing the relation between the true stress-true plastic strain. Comparing Fig. 4.6a with Fig. 4.6b, the latter shows less scatter in

the four specimens tested. Table 4.2 shows the yield stress at 0.2% plastic strain and the ultimate tensile strength for all the tests. Looking at the standard deviation for the small pipes compared with the large pipes, the numbers underline what is also shown in Fig. 4.6. Although the tests vary to some extent, the average yield stress is the same for both pipes. The ultimate tensile strength is a little bit higher for the large pipes.

(a) *Different locations in pipe S*   **(b)** *Different locations in pipe L*
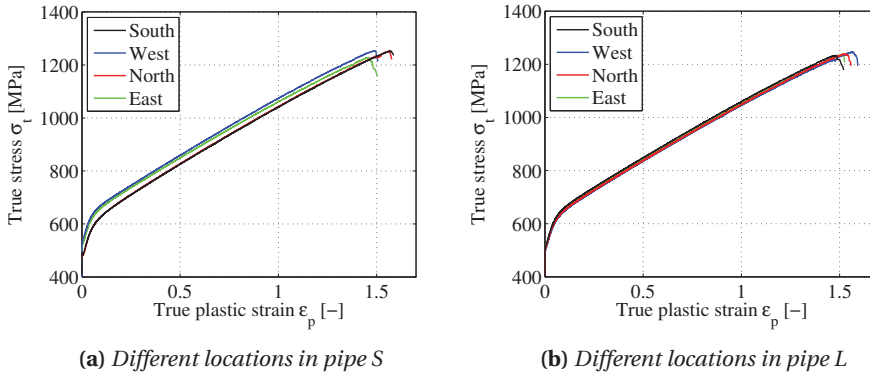
Figure 4.6: *Force-displacement for Pipe S and Pipe L.*

Table 4.2: *Results from steel test [MPa].*

Location	Small pipes		Large pipes	
	σ_{02}	σ_u	σ_{02}	σ_u
South	482	569	504	597
West	528	608	493	585
North	487	569	508	588
East	515	598	507	592
Average	503	586	503	591
Std. Dev.	22.11	20.05	6.88	5.2

4.3.2 PP Foam Compression Test

Fig. 4.7 shows one of the coating specimens at different time stages during the compression test. As can be seen in this figure, the radial elongation at the bottom of the specimen is greater than the radial elongation at the top. This was typical for most of the eight tests and it may be an indication of a variance in friction. Meaning that the friction between the top cone and the specimen may be higher than the friction at the bottom. This difference in friction gave some unfortunate shear forces in the specimens that will be discussed later in this chapter.
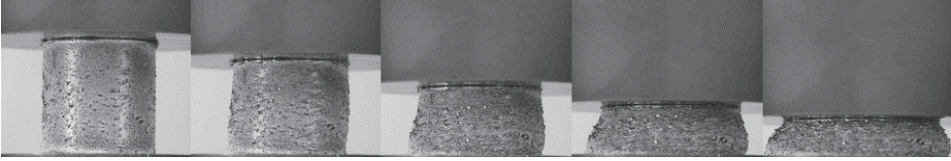
Figure 4.7: *Photo series from PP foam compression test, specimen 6.*

Force-displacement curves taken from the load cell and crosshead and the engineering stress-strain can be seen in Fig. 4.8. A crack noise was heard during the test of specimen 1. It is possible that something happened in the rig, but it is hard to determine what the specific cause was. The result was a dip in the force-displacement curve, seen in the magnified area in Fig. 4.8a.

(a) *Force - displacement curves*

(b) *Engineering stress - strain curves*
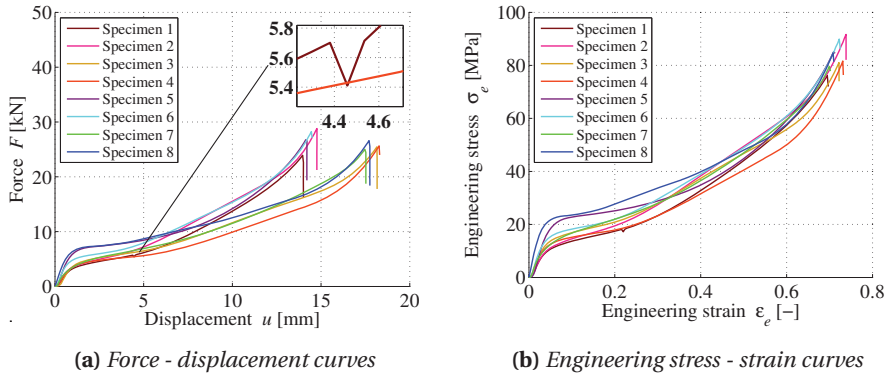
Figure 4.8: *Results from the PP foam compression tests.*

To establish a material model, true stress and true strain had to be obtained. DIC would be the preferred tool to use, but the quality of the speckled pattern was not optimal. It was decided to calculate true stress-true strain using the well established formulas shown in Eq. (4.1). This was also the method conducted by Statoil in a similar experiment [31].

$$\epsilon = \ln(1 + \epsilon_e) \qquad \sigma = \sigma_e(1 + \epsilon_e) \qquad (4.1)$$

32

It is important to remember that this is a compression test and therefore the ϵ_e must be negative as it follows the negative displacement. For visualisation purposes, all plots are in absolute values of the estimated true stress and true strain. The estimated true stress-true strain curves established are shown in Fig. 4.9. The results of the specimens with height of 25 mm are plotted with dashed lines. The gap between certain curves is pretty distinct and is examined further in this chapter.
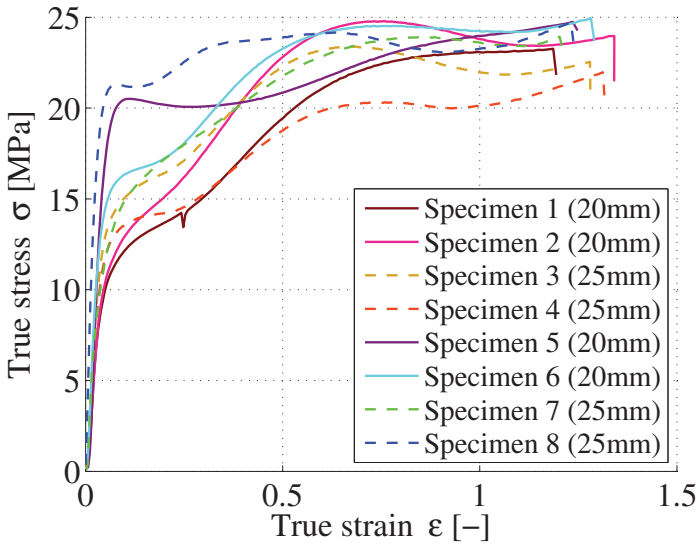
Figure 4.9: *Estimated true stress - true strain curves.*

The true stress-true strain curves are based on the assumption of preserved volume and that there is no barreling nor shear deformation in the specimens. Preservation of volume in a porous foam is not likely, but the values from Eq. (4.1) might still give an acceptable approximation depending on the magnitude of the volume change.

Visual examination of the tested specimens was carried out to see if barreling and shear forces were a big problem. A difference in the physical response of the specimens with a height of 25 mm and 20 mm could be seen. Fig. 4.10 and Fig. 4.11 shows that the deformation of all the taller specimens are more affected by shear forces than the shorter specimens. The eccentricity is normally larger with a longer specimen, and this is probably the reason for this difference in deformation. All the specimens show barreling. This means that the specimens have a triaxial stress state, that is not taken into account in the estimations of the true stress and true strain. The specimen that shows the least amount of barreling is specimen number 5 which can be seen on the far right in Fig. 4.10. The difference in friction at the top and bottom of this specimen also looks small, and might be the cause of this uniform deformation.

To see if the result was dependent on the height of the specimen, all the specimens with height of 25 mm were compared with all the specimens with height 20 mm. The result is the dashed versus the regular lines in Fig. 4.9.

Figure 4.10: *Deformation of the 20 mm specimens.*

Figure 4.11: *Deformation of the 25 mm specimens.*

The result did not show any consistent difference between the taller and smaller specimens. How the true stress-true strain curve would look like if the specimens did not show signs of shear force disruption or barreling is hard to say, however a material model needed to be established and it was decided to use all the tests in the further investigations.

Some of the true stress-true strain curves differ significantly from each other. Trying to find a trend, the curves were separated with respect to different parameters, similarly to what was done with the height. Statoil found a correlation between response and density of different batches of PP foam [31]. As described in Chapter 3, the coating of the big pipes is applied over an already coated pipe and this might cause different properties in the material.

Since the densities in the foam taken from pipe *S* and pipe *L* differed, it seemed logical to separate specimens taken from pipe *S* and pipe *L*. Strain rates usually give rise to difference in the response, and this was checked as well. The results from these two comparisons can be seen in Fig. 4.12.
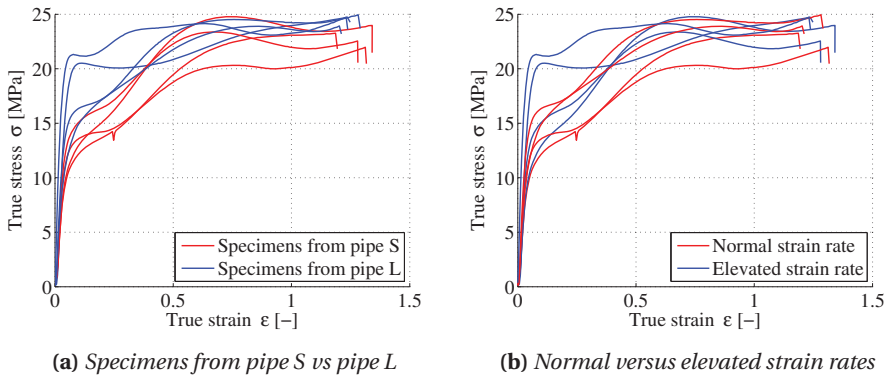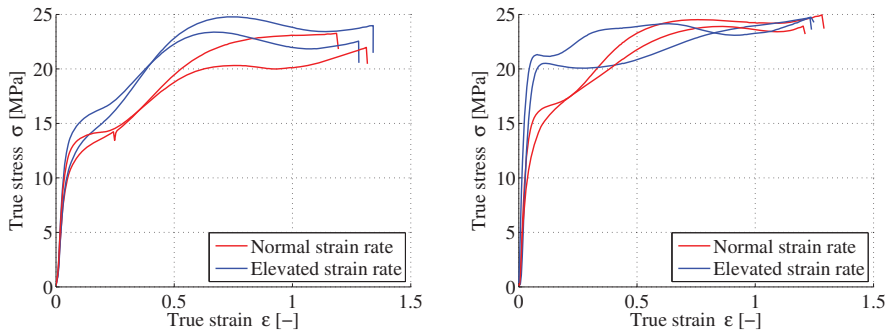

(a) *Specimens from pipe S vs pipe L*

(b) *Normal versus elevated strain rates*

Figure 4.12: *Effect of specimens from different pipes and with different strain rates.*

A trend in the difference in response was seen when testing foam from the different pipes. The trend was especially visible up to a strain of $\epsilon \approx 0.4$. However, normal strain rate versus elevated strain rate did not show any significant trend comparing all the eight specimens.

To study the strain rate more closely, the response from pipe S and pipe L was separated. By doing this, the effect of elevating the strain rate became clearer as seen in Fig. 4.13. It looks like the elevated strain rate gave a higher yield stress for the specimens taken from pipe L. However, it did not seem to affect the maximum strength significantly.

For the specimen taken from pipe S the curves are pretty similar, although the peak is a bit higher for the elevated strain rate tests. At large displacements, most of the tests end up at the same level of about 22-23 MPa, except for specimen 4 which is slightly below the other curves.

(a) *Effect of strain rate at coating from pipe S*   **(b)** *Effect of strain rate at coating from pipe L*

Figure 4.13: *Effect of strain rate when separating pipe S and pipe L.*

The Young's modulus was estimated for each of the specimens by visually inspecting the engineering stress versus engineering strain curve. Microsoft Excel was used to inspect the elastic area of the curves. The logging of force and displacement was only done every 4 seconds. This made the points that were in the elastic area few. This can be shown in 4.14 and made it hard to establish exactly where the elastic area starts and ends. However, points were chosen in what seemed like a linear part for all specimens and linear regression was done. Some polymers can show nonlinear elastic behaviour [35], but this was not explored further. The yield stress was estimated by inspecting the curve as well. The end of the linear elastic part was found and the stress value at the corresponding strain was chosen. The average yield stress and Young's modulus show a clear difference between pipe S and pipe L.

Table 4.3 shows the specimens separated in pipe S and pipe L, their initial strain rate and their estimated yield stress and Young's modulus.
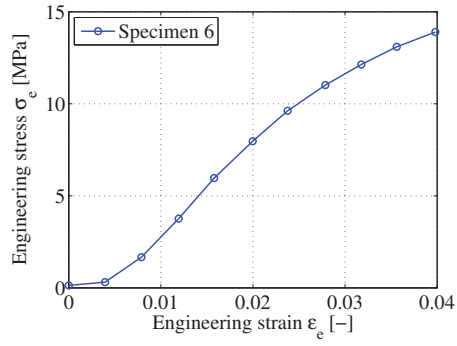
Figure 4.14: *Showing the engineering stress - engineering strain for specimen 6 as an example.*

Table 4.3: *Information and measurements of the coating specimens.*

Specimen #	From pipe	$\dot{\varepsilon}$ [s^{-1}]	ρ [kg/m^3]	σ_y [MPa]	E [MPa]
1	S	10^{-3}	704	5.1	354
2	S	10^{-2}	704	6.3	382
3	S	$8 \cdot 10^{-3}$	717	8.8	430
4	S	$8 \cdot 10^{-4}$	710	7.1	438
Average			709	6.8	401
5	L	10^{-2}	707	10.1	630
6	L	10^{-3}	748	8.1	544
7	L	$8 \cdot 10^{-4}$	734	5.5	495
8	L	$8 \cdot 10^{-3}$	759	11.2	762
Average			737	8.7	608

5 | Material Model

5.1 Steel

The X65 steel has been studied in depth in the previous work. Hence, the main focus was to simply conduct a basic tension test. A material model for the steel was established based on the results obtained from the tension test. The material model is an elasto-plastic model that does not take into account neither temperature nor viscoplasticity. A validation with respect to the tension test and quasi-static component test of the uncoated pipe S was done.

The hardening and yield stress were both deduced from the tension test, shown in Fig. 4.6. The other material parameters were chosen from well established values from earlier research [8]. Validation of the chosen value of the Young's modulus was done with the results from the tension test, see Fig. 5.1b. In Fig. 5.1a, the material parameters are presented and describes the elastic region of our material model.

Parameter	Basis model
E	208000 MPa
σ_0	503 MPa
ν	0.3
ρ	$7.8 \cdot 10^{-9}$ ton/mm^3

(a) *Elastic properties*
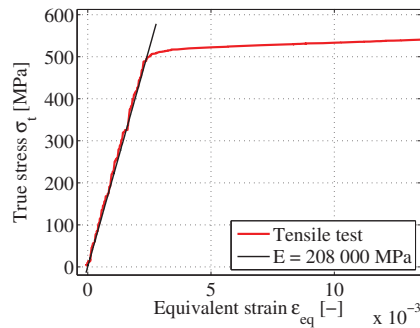
(b) *Youngs modulus correlation*

Figure 5.1: *Elastic properties and validation of the Youngs Modulus.*

Slåttedalen and Ørmen [2] conducted tests and concluded that the X65 steel can be assumed to be isotropic and homogeneous. Dynamic tensile tests conducted by Slåttedalen and Ørmen [2] showed that the flow stress was affected by the strain rate. However, since all the component tests were conducted quasi-statically at a low strain rate,

the strain rate sensitivity was not included in the material model. To depict the hardening one representative true stress-strain curve from the tension test was chosen. The true stress obtained from this test was merely the stress in the loading direction. Estimating the average equivalent stress was done using a Bridgman correction, see Chapter 2. The corrected true stress-true strain curve was then tabulated as the hardening relation in Abaqus/Explicit. Fig. 5.3a shows the uncorrected true stress-true strain curve as well as the corrected and chosen hardening curve.
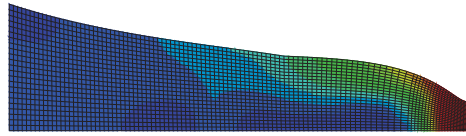
Figure 5.2: *Axisymmetric model for the tensile test simulation.*

An axisymmetric model, Fig. 5.2, made in Abaqus/Explicit was provided and employed with the material parameters presented in Fig. 5.1a and the hardening curve for the material model shown in Fig. 5.3a.

The model was run with five different mesh sizes. The different sizes was 5, 10, 20, 50 and 100 elements over the radius of the specimen. The responses are presented in Fig. 5.3b. It can be seen how the increasingly refined mesh made the response more compliant and that the solution eventually converged. The coarsest mesh gave a markedly stiffer response from where necking occurred and throughout the analysis.

(a) *Bridgman correction*

(b) *Response with refined mesh*
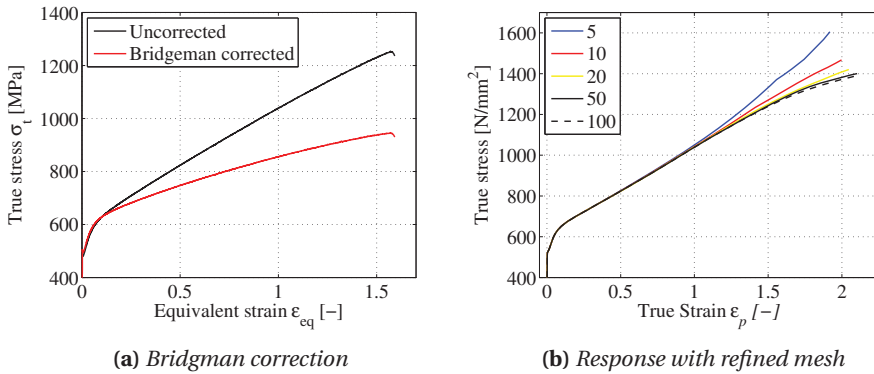
Figure 5.3: *The hardening model and response from the tensile test with refined mesh.*

5.1.1 Validation of Material Model

The material properties in Table 5.1a combined with the hardening model in Fig. 5.3a amounted the steel material model. Fig. 5.4 shows how this model correlated with the results obtained from the tension test program. How the steel correlated with the quasi-static component test of pipe *S*, is shown in Chapter 8, Fig. 8.5a. The dotted blue plots in Fig. 5.4 shows the true stress-true strain relation from all the tensile specimens. Plotted in solid black, the converged solution from the numerical simulation is shown.
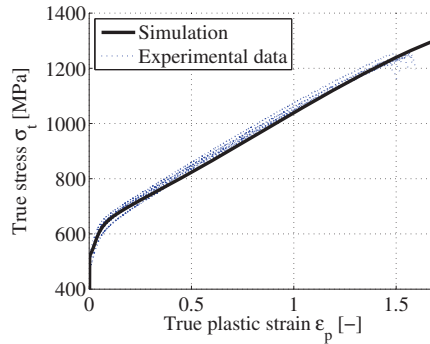
Figure 5.4: *Validation of the steel tensile test.*

5.2 Coating

As seen in Subsection 4.3.2, the estimated true stress-true strain curves vary depending on what pipe the specimens are taken from, and the initial strain rate of the specimen. Because of the large variation, the number of curves needed to be reduced before fitting a material model.

The material model would be used in the numerical simulations of pipe *S* and pipe *L*, as well as in the factorial design simulations of the sandwich specimens. Consequently, two factors became important when deciding what results to use in the material model.

- Both the PP foam specimens and the sandwich specimens were taken from pipe *S*.

- Deformation rate of the PP foam specimen 1 and 4 and sandwich specimen 1 and 2 were created so they would have a similar initial strain rate. (Ranging from $7 \cdot 10^{-4}$ s^{-1} to 10^{-3} s^{-1})

The Young's modulus and the yield stress did not show any trends from the difference in strain rates. Therefore, it was decided to use an average from all of the four specimens taken from pipe *S* to find these parameters. The density was also calculated by taking the average of the four specimens. The Poisson ratio was taken from Statoil's report by M.Polanco-Loria [31]. These material properties can be seen in Table 5.1.

Table 5.1: *Properties for the coating material model.*

Parameter	Material model for the coating
E	401 MPa
σ_0	6.8 MPa
ν	0.3
ρ	$7.3 \cdot 10^{-10}$ ton/mm^3

The hardening input for the material model is based on specimen 1 and 4 as can be seen in Fig. 5.5a. For simplicity and to get a smooth graph, values were taken from specimen 4, but with higher hardening to match specimen 1 better. Fig. 5.5b shows the material model used for the numerical simulations together with all four specimens taken from pipe S. Although material models from both pipe L and pipe S could have been created, it was decided that one material model would be adequate. The material model is an elasto-plastic model with von Mises yield criterion. It does not take into account neither temperature nor viscoplasticity. The values for the isotropic hardening is tabulated from the black plot seen in Fig. 5.5b. The values from the last point and out are extrapolated perfectly-plastic.

All of the specimens have been tested with different strain rates and the material model was initially meant to take strain rates into account. However, since the dynamic tests were delayed and not conducted in time, this was left out of the material model.
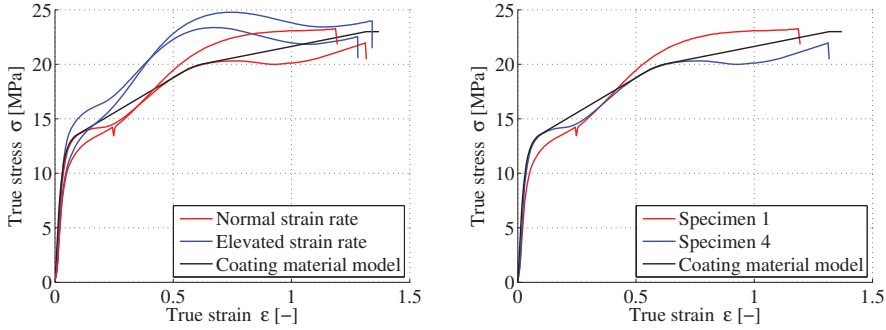
(a) *Coating model with all specimens from S*   **(b)** *Coating model with specimens 1 and 4*

Figure 5.5: *Fitting the material model to the appropriate foam specimens.*

5.2.1 Validation of the Material Model

To validate the material model, the specimens were simulated in Abaqus/Standard. The test were quasi-static and a Static, General analysis was used. The specimens were created axisymmetric. As mentioned in Subsection 4.3.2, no shear forces were assumed. To satisfy this assumption, the tests were run with no friction between the specimen and the top and bottom plate. A simulation of specimen 4 can be seen in Fig. 5.6. To see the effects of friction, simulations were carried out with different friction coefficients,

$\mu = 0.1$ and $\mu = 0.025$. Fig. 5.7 shows what the simulations looked like with the different friction coefficients. The force-displacement curves can be seen in 5.8a. The results show no significant difference whether friction is used or not.
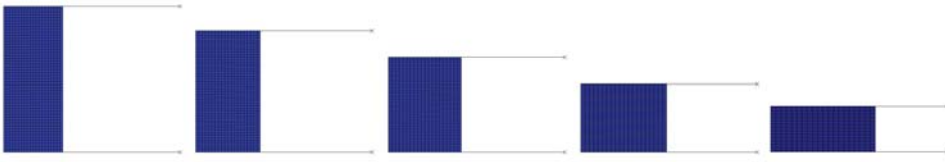
Figure 5.6: *Axisymmetric simulation of foam specimen with $\mu = 0$.*
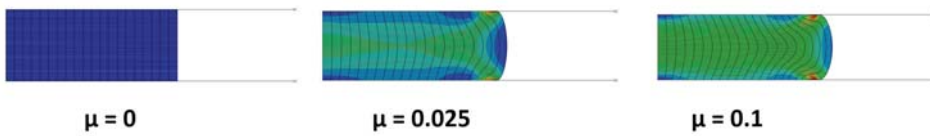
Figure 5.7: *Axisymmetric simulation of foam specimen with different values of friction.*

(a) *Effect of different friction coefficients*

(b) *Comparing simulations and experiment*
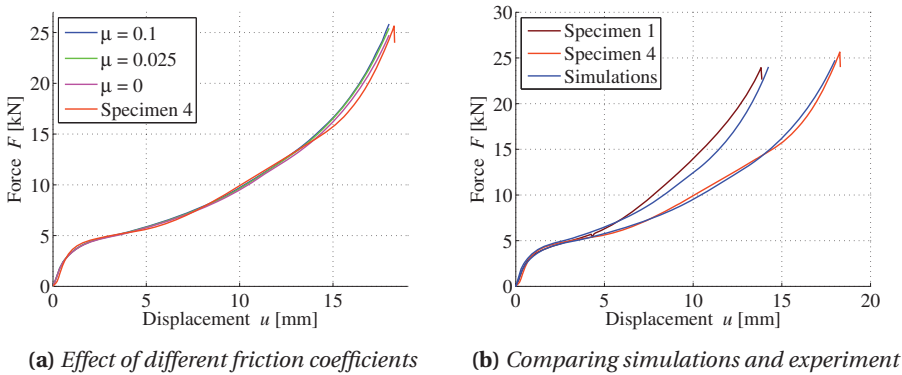
Figure 5.8: *Examination of different friction coefficients and validation of the material model.*

The force-displacement curves from Abaqus/Standard together with the force-displacement from specimen 1 and 4 are shown in Fig. 5.8b. The material model seems satisfactory, despite all the assumptions that underlie the model. Specimen 1 is somewhat underestimated, but this makes sense since the estimated true stress-true strain curve for the same specimen has a higher peak than the one used to establish the material model.

6 | Component Tests

To identify and analyze the different behaviour of pipes with and without coating, component tests were conducted. Tests were done on two types of pipes with different thickness, with and without coating. Two relatively long coated pipes with different dimensions were provided by Statoil. The pipes were cut in specimens of about 1 m and denoted with names R1 through R8. The coating was removed manually from four of the specimens to do tests on the bare steel. The pipes are referred to as pipe *L* and pipe *S*, where the abbreviation describes the size of the pipe - large and small. In this chapter the experimental results will be presented from all the tests conducted. A short description of the measurements of the pipes will be presented as well.

The following experiments were initially planned:

- A quasi-static denting test.
- A dynamic test in the kicking machine.
- A component test on the coating sandwich (all layers of the coating).

The two first tests were planned to be done on pipes with and without coating. The dynamic test in the kicking machine was not conducted due to postponed delivery of the right measurement equipment.

6.1 Quasi-Static Denting

6.1.1 Measurements of the Pipes

Prior to testing, different types of control measurements had to be done. The eight pipes R1 to R8 were measured. Statoil provided two different pipe configurations, whose geometries are shown in Fig. 6.1.

The nominal dimensions of the pipes from the manufacturer are shown in Fig. 6.2a. The thickness of the steel was measured using a Limit Blade Micrometer in four different places (North, South, East and West) in both ends, see Fig. 6.1. The diameter was measured with a digital caliper.
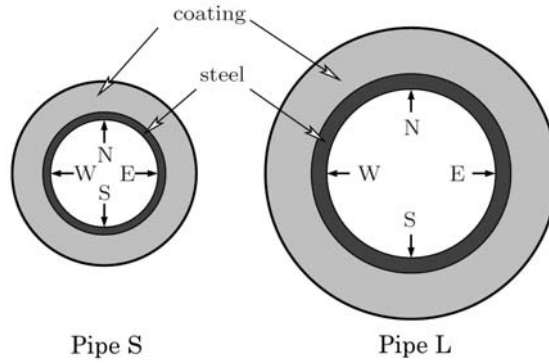
Figure 6.1: *The two pipe configurations.*

Since the coating was manually removed, there was some residue of coating on the steel pipes. To obtain an as accurate measurement as possible, the remains of the coating was polished off. Sources of error in the measurements were inevitable. Among others, making sure the caliper was in a perpendicular position when measuring the diameter was one of them.

To figure out a standard deviation in the measurements, the thickness and diameter was measured at the same location 30 times each. All the measurements are included in Appendix-A.

	Pipe S	Pipe L
D_i	244.50	254.00
D_0	273.10	305.00
D_c	369.10	465.80
t_p	14.30	25.50
t_c	48.00	80.40

(a)

(b)
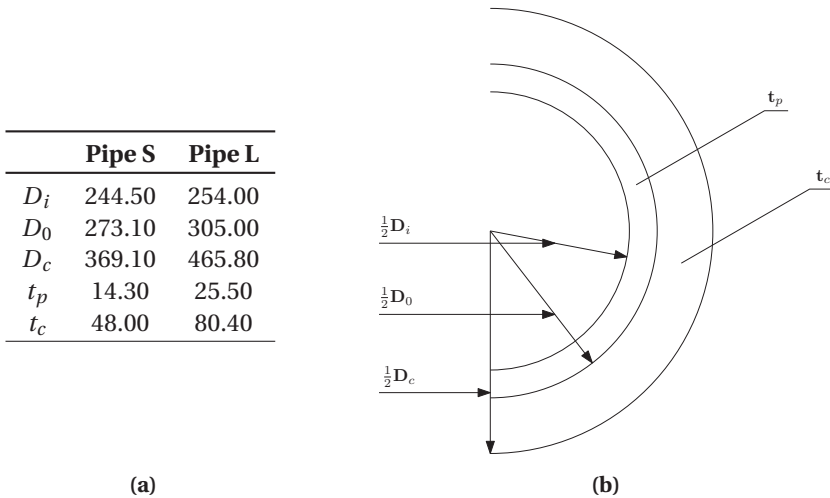
Figure 6.2: *Table and figure of the nominal pipe dimensions.*

Fig. 6.3 shows the measurements of the indenter used in the experiments. The indenter was supposed to simulate the trawl gear.

44

(a) *Front view*

(b) *Side view*
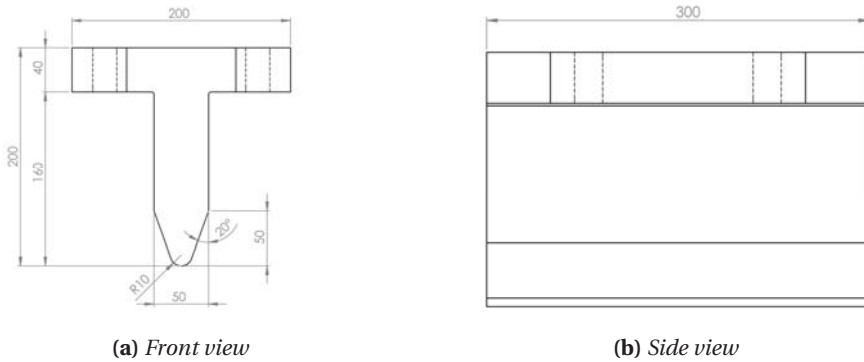
Figure 6.3: *Overview of the dimentions of the indenter.*

6.1.2 Experimental Set-up

The set-up for the quasi-static experiments is shown in Fig. 6.4 and 6.5. The set-up was the same for the coated and uncoated pipes. The pipes were resting on a rigid steel base and was kept in their initial position by two wooden supports. To measure the internal displacement, a linear variable differential transformer, denoted LVDT, was placed inside the pipes directly underneath the indenter. To measure the outer displacement, another LVDT was connected to the indenter by a magnetic base where the pipes were resting. Since this steel base followed the rig, the source of error related to the displacement in the rig was kept at a minimum. Fig. 6.4a shows an overview explaining the different parts of the set-up.

The force was applied from a 1800 kN Instron machine. The hydraulic pressure could be increased and the pipes were tested up to a force of 2300 kN. The indenter was loaded and unloaded with increments of 300 kN. The deformation rate was set to 10 mm/min. In Fig. 6.4b a picture of the set-up is shown as well.
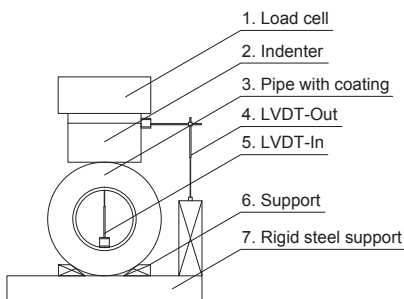
(a) *Drawing of the parts in the set-up*

(b) *Quasi-static set-up*

Figure 6.4: *Illustrations of the quasi-static set-up.*
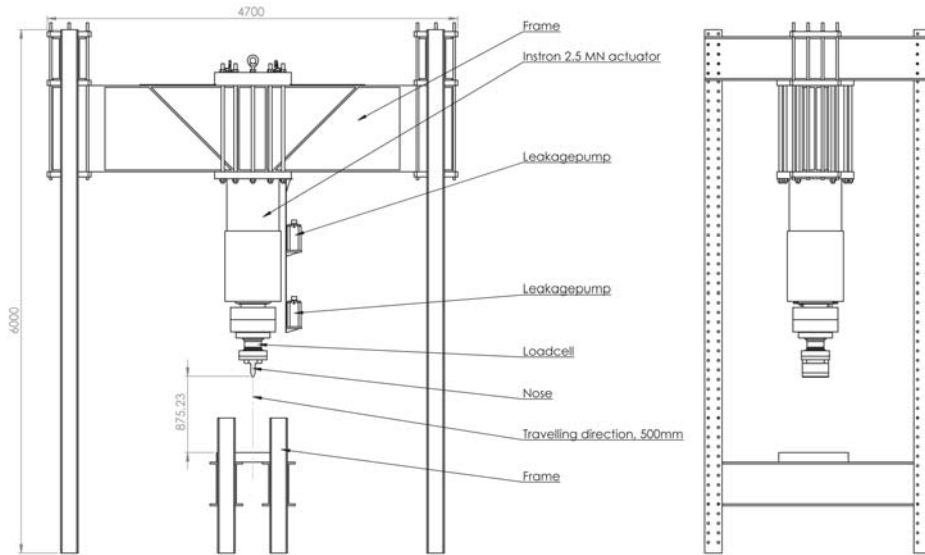
Figure 6.5: *Instron Machine. Front and side view.*

6.1.3   Results of the Coated Pipes

Tab. 6.1 shows an overview of the component tests conducted on the pipes with coating. The table describes important properties about the tests. The direction column describes which direction the indenter was loaded in parallel to. A total of 5 tests were done as described in the previous set-up section. This section contains the results from all tests. Test number 3 and 5 are the results that are used for comparison throughout this thesis. This is because test 3 was of the large pipe with coating subjected with the highest load. Test 5 was the only small pipe with coating that was tested.

Table 6.1: *Overview of tests conducted on the coated pipes.*

Test number	Pipe	Size	Direction	Description	Max. Load [kN]	Approx. Energy [kJ]
1	R8	Large	N / N-E	Normal procedure	1741	70.5
2	R8	Large	N / N-E	Pipe R8 retested	2083	33.2
3	R7	Large	W / S-W	Normal procedure	2228	73.1
4	R7	Large	S / S-E	Pipe R7 rotated 90°	2217	75.4
5	R4	Small	N	Normal procedure	1210	79.8

Fig. 6.6 shows an overview and a close up of the coated pipes after denting. Since the width of the indenter was smaller than the diameter of the coated pipes, it cut into the coating at each side. The indenter compressed the coating up to a certain point, before it penetrated and the coating layers fractured under and along the sides of the indenter. The final state of the coating and the fracture can be seen in Fig. 6.6b.

(a) *Overview*　　　　　　　　　　(b) *Close up*
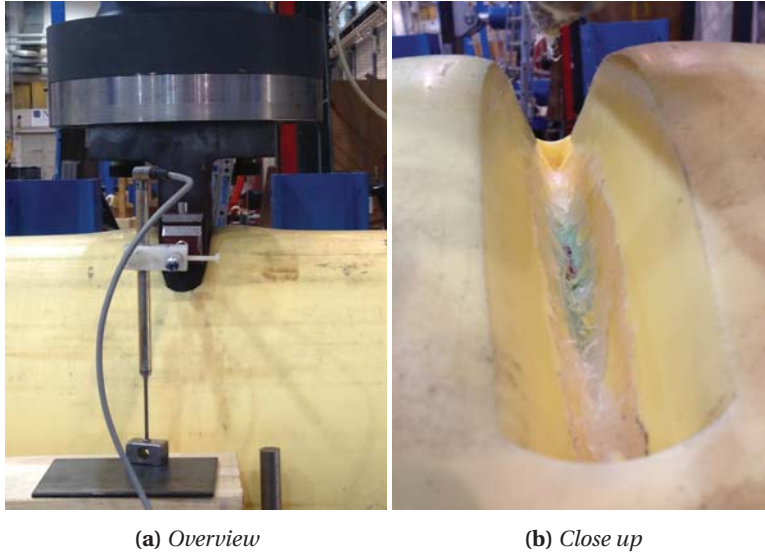
Figure 6.6: *Overview of the deformation of coated pipes.*

Load Path

Fig. 6.7 shows the force-displacement curve from pipe *L* (R7). This pipe is the one that is used for comparison for the large coated pipe. In this section the load path is described.

- The initial path from 0 to 1 shows a linear response. At point 1 unloading of the pipe starts. When it is reloaded, the loading curve creates a characteristic loop. This is called a hystereses loop and comes from viscoelastic behaviour in the coating material [31]. The theory of viscoelasticity is not explained any further in this thesis. Looking at the reloading after the first unloading, one can see that the stiffness has increased slightly compared to the initial stiffness. This may be a consequence of increased density after compressing the coating material.

- The path 1 to 2 shows the continuation of the linear response with little deviation from the linearity in the initial path.

- In the path from 2-3 it can be observed that the response is not a smooth curve anymore. The small oscillations in the curve may be characterized by incremental local failure in the polymeric foam, seen in Fig. 6.6b. The polymer was ripped apart by increasingly load, and this can be seen by how the force falls slightly before increasing again, repeatedly.

- Point 3-4 shows the continuation of this effect. In point 4 the coating fractured entirely and the indenter hit the steel pipe.

- The path from 4 to 5 shows the force-displacement after the indenter has penetrated the coating and is in contact with the steel. The response is dominated by the steel material between these points.
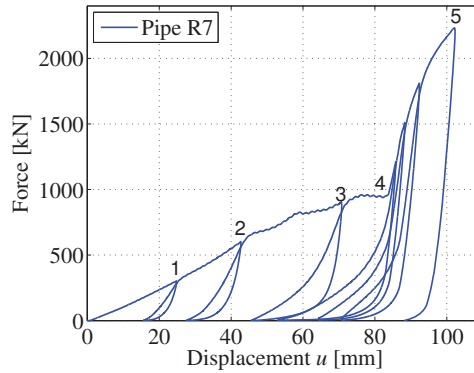
Figure 6.7: *Force - outer displacement load path of pipe R7.*

Inner Displacement

Fig. 6.8 shows the force-inner displacement curve.

- The inner displacement is relatively small in the first loading increments. Looking at Fig. 6.7 that shows the response of outer displacement, 6 load increments are seen. Only 3 of these increments are clearly visible and distinguished in Fig. 6.8. These 3 first load increments all go back to about zero displacement at the end of the unloading steps. This implies that these increments are in the elastic region of the steel.

- The rest of the path shows that the steel is in the plastic area. The loading and unloading shows the same hystereses loop mentioned earlier, however, the hystereses area is smaller than the one seen on the coating.
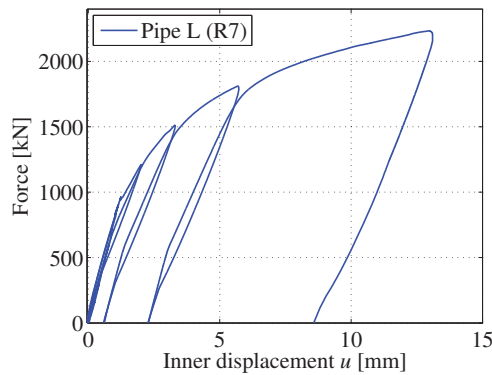

Figure 6.8: *Force - inner displacement of pipe R7.*

Pipe L

Fig. 6.9 shows the force-displacement curves from the first component tests. The first test was loaded up to 1800 kN. The sudden drop in force in point 1 in Fig. 6.9a was due to a manual control of the force. There was some confusion regarding what load increment the loading and unloading should take place. However, this did not impact the result significantly.

The test rig was supposed to exert a force up to a maximum of 2100 kN. The first test was only loaded up to about 1800 kN, and it was of interest to load the pipe with as much force as possible. The same pipe was tested again, this time without the incremental loading and unloading, and the force-displacement can be seen in Fig. 6.9b.

(a) *First round* **(b)** *Second round*
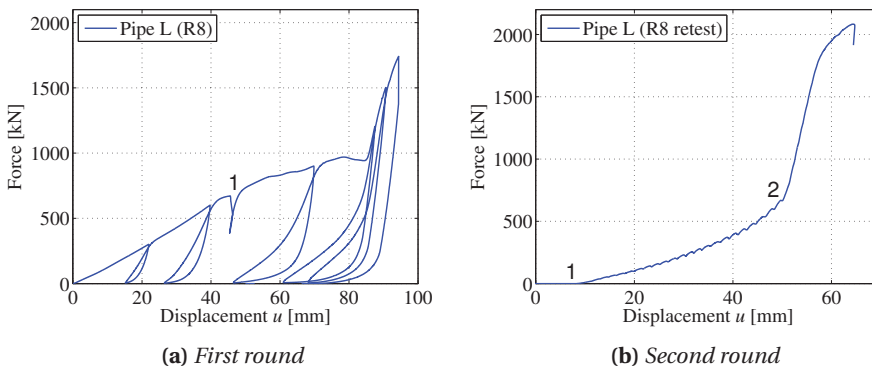
Figure 6.9: *Force - displacement curves of pipe R8.*

The path between point 1 and 2 (Fig. 6.9b) shows the path where the indenter is loaded in the same coating crack. The force shows some sort of oscillation and this may be from the indenter hitting some of the coating on the way down, since the crack closed slightly after the indenter was unloaded. In point 2 a clear kink is shown and represents the point where the indenter fractured the last of the coating layer and hit the steel pipe.

One of the top beams in the test rig was not supported enough laterally and buckled when the load exceeded 2050 kN. The data retrieved from the experiment is valid up to this point. The rig was later supported sufficiently and the continuation of the testing could continue without any further problems.

To compare the two results, Fig. 6.10 shows a part of the force-displacement curve for both tests. The retest curve, shown in red, seems to follow the path similar to the loading curve from the first test up to a certain point. However, the response after the indenter hits the steel is somewhat stiffer for the second test. In the first run, when the indenter hits the steel, it is also in contact with the coating on the sides. In the second round, there is probably more space for the indenter. This time it hits mainly steel, and a smaller portion of the coating. This may be the reason for the difference in stiffness for the two curves.
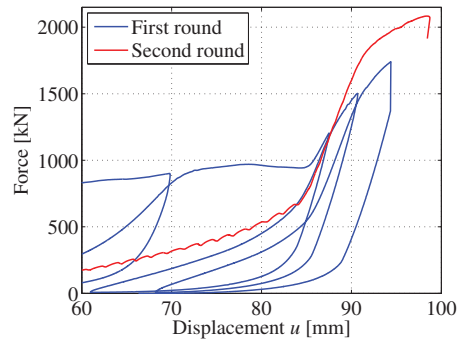
Figure 6.10: *Comparison of pipe R8 first and second round.*

Fig. 6.11 shows the force-displacement curve for R7 and R7 rotated. The first test, shown in blue, shows a load path similar to the one explained in the earlier section. The pipe was rotated 90° and tested again. This result is shown in red.
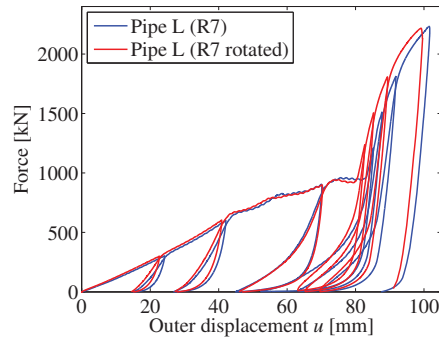
Figure 6.11: *Comparison of test R7 and R7 rotated.*

The two curves are almost identical. However, pipe R7 hits the steel before pipe R7 rotated. This may have occurred because the coating on one side of the pipe had already fractured, and this affected the response since the indenter penetrates coating that is adjacent to the crack from the first test.

Pipe S

In Fig. 6.12 the force-displacement curves for pipe S with coating (R4) are shown. The small pipe was loaded up to 1200 kN. The load path is similar to the one seen for the large pipe - a linear behaviour up to a point where the indenter hit the steel. The characteristic kink is also present in the curve. A loud and sudden mechanical sound from the rig was heard during the test. This resulted in a sudden drop in force seen in point 1 in both curves, Fig 6.12. The cause of this sound was not clear, however, it might have been something in the rig. It did not affect the result significantly.

(a) *Outer displacement*   **(b)** *Inner displacement*
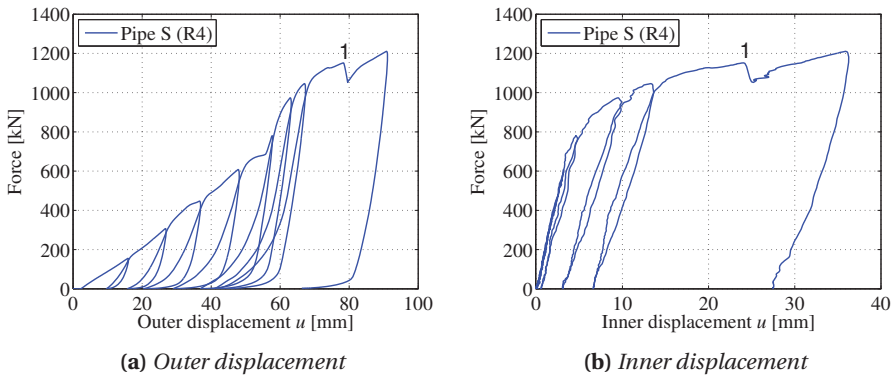
Figure 6.12: *Force - displacement curves of pipe S (R4).*

6.1.4 Results of the Uncoated Pipes

Table 6.2 shows an overview of the two component tests done on the bare steel pipes. The steel pipes were tested to quantify the effect of the coating as well as comparing the result with the estimations with DNV-RP-111. The latter is done in Chapter 9.

Table 6.2: *Overview of tests done on uncoated pipes.*

Test Number	Pipe	Size	Orientation	Description	Approx. Energy [kJ]
1	R6	Large	S / S-W	Normal procedure	48.6
2	R1	Small	W / S-W	Normal procedure	59.1

The force - displacement curves for the uncoated pipes are shown in Fig. 6.13 and 6.14. The curves show expected results for the steel pipes - the smaller pipe deform more than the larger pipe.

6.1.5 Comparison

Fig 6.15 shows a comparison of the force-inner displacement curve for pipe *S* and pipe *L*. In both tests of the steel pipes, the LVDT measuring the inner displacement had to be removed at a certain displacement to not get destroyed by the dent. This is why the maximum load level for the inner and outer displacement on the steel pipes do not coincide in Fig. 6.15 and 6.16.

Fig. 6.15 shows how the coated pipes get a smaller inner displacement at the same load level compared to the same pipes in bare steel. To look at how the energy absorption for the steel pipes and coated pipes differed, a comparison was done and can be seen in Table 6.3.

The inner displacements at a load level of 800 kN for pipe S without coating and 1500 kN for pipe L without coating were extracted. The energy absorbed by the pipes without

(a) *Pipe R6*

(b) *Pipe R1*
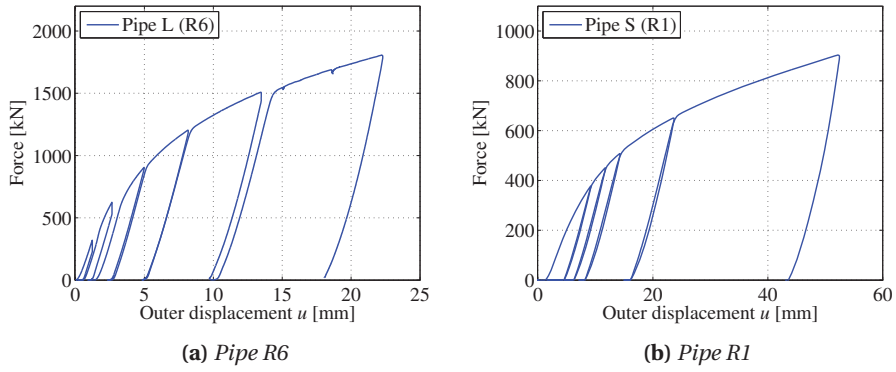
Figure 6.13: *Force - outer displacement curves of uncoated pipes.*

(a) *Pipe R6*

(b) *Pipe R1*
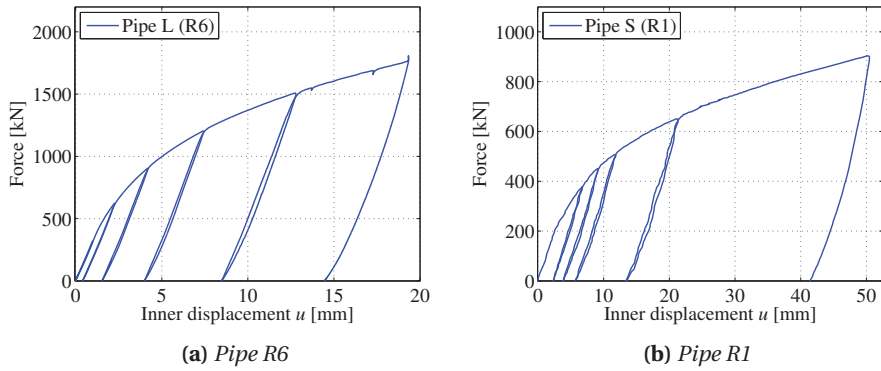
Figure 6.14: *Force - inner displacement curves of uncoated pipes.*

coating was found by integrating the force-outer displacement curves up to these load levels. Then the inner displacements for the pipes with coating, at the same energy level absorbed, were found.

The inner displacement, corresponding to the dent depth, was found and compared for pipe *S* and pipe *L*. The results are shown in Tab. 6.3.

Table 6.3: *Difference in dent depth at the same energy level.*

	Pipe S [mm]	Pipe L [mm]
Inner displacement - Steel pipe	35.7	12.8
Inner displacement - Coated pipe	3.4	0.7
Dent depth difference	32.3	12.1

(a) *Pipe S*

(b) *Pipe L*
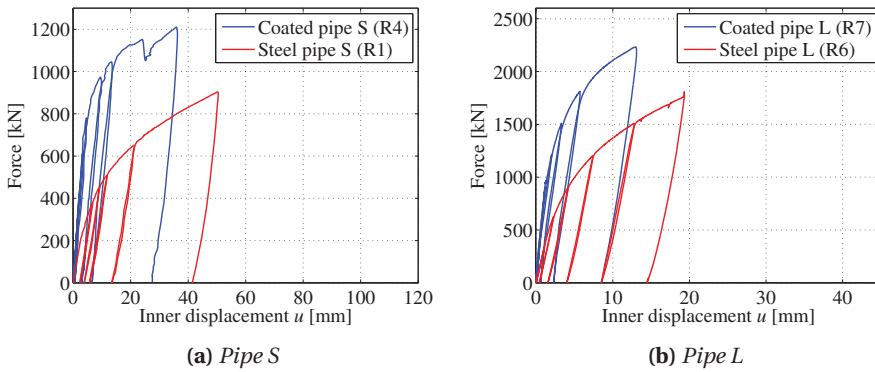
Figure 6.15: *Force - inner displacement comparison with and without coating.*

(a) *Pipe S*

(b) *Pipe L*
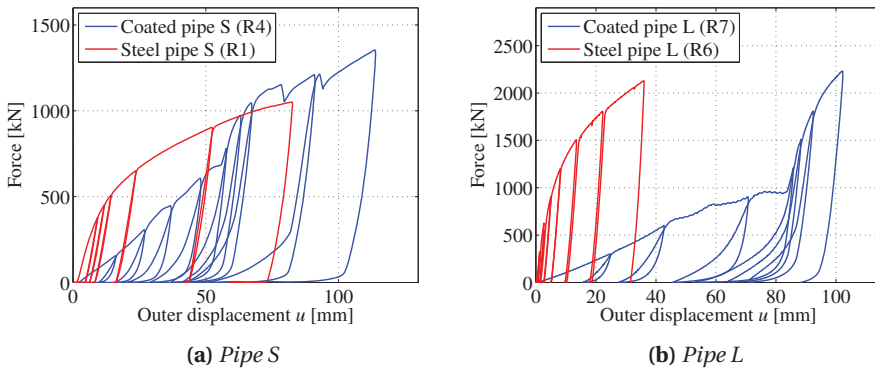
Figure 6.16: *Force - outer displacement comparison with and without coating.*

6.2 Sandwich Coating Component Test

6.2.1 Measurement of the Components

A simple compression test was done on the polymer coating. Three samples were cut out of pipe *S*, giving the specimens a height of approximately 48 mm. The specimens were cut out in the shape shown in Fig. 6.17a and as seen, the width of the component was approximately 37 mm. In the longitudinal direction the length of the specimen was 50 mm. These component specimens are in this thesis sometimes referred to as sandwich specimens.

The compression test on the full coating sandwich (the inner solid PP layer, the PP foam and the outer shield layer) was performed to investigate the effect of the inner and outer layers. The main goal with the component test of the coating sandwich, was to obtain the force-displacement curve which is used for the factorial design in Chapter 7.
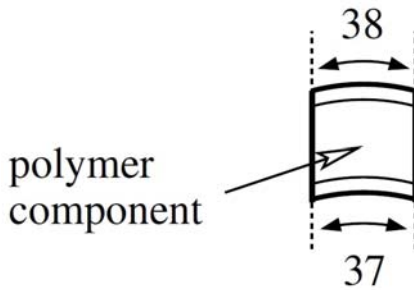
(a) *Sandwich component*
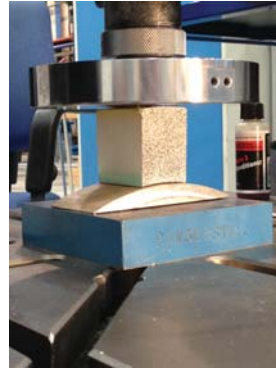
(b) *Compression test set-up*

Figure 6.17: *Illustrations of the coating sandwich component and the compression test set-up.*

6.2.2 Experimental Set-up

Since the specimens are not flat at the bottom, a small steel piece was manufactured from pipe S to support the specimen as seen in Fig. 6.17a.

The component was then loaded quasi-statically in compression with a flat steel plate, which covered the entire surface area. The deformation rate was $\dot{u} = 2$ mm/min corresponding to an initial strain rate of approximately $\dot{\epsilon} = 7 \cdot 10^{-4}$ s^{-1}. Force-displacement from the load cell and crosshead was logged and the DIC technology was utilized during the tests. However, only the force-displacement curves were used further, hence DIC was merely used to obtain the lateral displacement in the factorial design.

6.2.3 Results

One of the sandwich tests can be seen in Fig. 6.18. The pictures show that the vertical elongation is greater for the PP foam than for the inner PP solid layer and the outer shield layer. This was expected as Statoil had found a higher Young's modulus and yield stress for both of these materials [31].
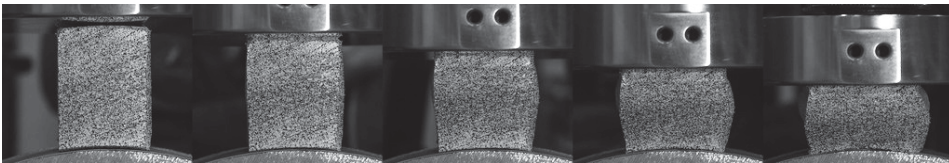
Figure 6.18: *Picture series of sandwich specimen 2 compression test.*

Fig. 6.19 shows force-displacement as logged by the load cell and crosshead, as well as the engineering stress-engineering strain curve. Because of the difference in the inner and outer radius of the coating, the height of the specimen differ a little over the length. The variation found by calculation was small ($\delta \approx 0.3$ mm), therefore an average of the

height at the sides and in the middle was used when calculating the engineering strain. The response of sandwich 1 and 2 was almost identical and sandwich 3 had a higher response curve. This was expected because of its higher deformation rate, set to $\dot{u} = 20$ mm/min.

(a) *Force - displacment*   **(b)** *Engineering stress - engineering strain*
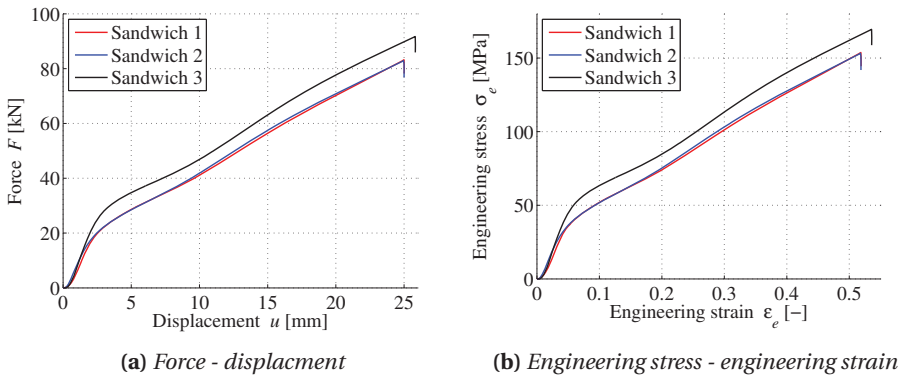
Figure 6.19: *Response from the sandwich compression tests.*

A comparison between the engineering stress-engineering strain curves from the sandwich specimens and coating specimens was done even though the sandwich tests are component tests and the PP foam tests are material tests. Hopefully it will still give some insight in how the outer shield layer and inner solid PP layer affects the overall response of the coating.

In Fig. 6.20, we see that the sandwich specimens are much tougher than the coating specimens. The main reason is probably the fact that the sandwich specimens are more restricted from horizontal expansion than the foam specimens. A number of reasons may play a role in this, some listed below.

- The geometry of the specimens are not alike (cylinder versus a sort of cube), this may cause some boundary effects.

- The top and bottom layers keep the PP foam from expanding perpendicularly to the load direction. I.e. the friction between the PP foam and outer and inner layers in the sandwich is much higher than for the friction between the PP foam and steel cones in the PP foam material tests.

- The sandwich is not flat at the bottom and this hinders the component to expand as well.

- The foam probably had less friction between the cones because of the tape and lubricant, compared with the rougher material of the sandwich.

True stress-true strain was not calculated since it was not going to be used for any particular purpose. Only the force-displacement curve was used in the factorial design. Obtaining the true stress-true strain would probably have been difficult without using DIC. This is because of the boundary issues of the specimens. The three different layers create a nonuniform deformation and the specimen is also curved.
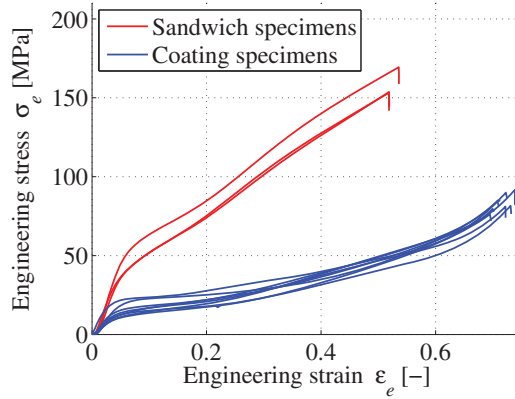
Figure 6.20: *Engineering stress - engineering strain from the sandwich specimens versus the coating specimens.*

7 | Factorial Design of Sandwhich Component

A parameter study using an approach called Factorial Design was conducted. The motivation was to get a better understanding of how different variables affected the coating model. The coating layer was chosen for this study, due to the fact that the steel pipe itself has been studied extensively in previous research. This section is divided in two parts. The first part explains what factorial design is and how to utilize it. In the last part, the factorial design is used on the sandwich component compression test. The theory in this section is based on the work by Box et al. [36].

7.1 General Factorial Design

A common method to study how variables affect a simulation or experiment, is the "One-factor-at-a-time" method. This method provides an estimate of the effect of a single variable at selected fixed conditions of the other variables. For this method to be useful, it is necessary to assume that the effect would be the same at other settings of the remaining variables. This means that the variables that are varied has to act on the response additively. If the variables do not act additively, this "One-factor-at-a-time" method fails to detect and estimate the interactions that measure the non-additivity.

On the contrary, the factorial design makes it possible to estimate how the variables interact. It requires fewer runs than varying one factor at a time. In fact, for a two-level factorial design, the number of runs needed to conduct a study is 2^k, where k is the number of variables chosen. Being able to look at how the variables interact as well as saving computational time, the factorial design was the chosen method for this study of the coating.

A fixed number of variables are chosen. These variables can be both quantitative and qualitative. For each of these variables, different levels have to be established. In this thesis, it was decided to run a two-level factorial design with three variables. As well as limiting the runs needed, it makes it easy to interpret and present the output in e.g. a cube plot. A two-level design means having one high and one low level of each of the chosen variables. These different levels are conveniently coded by a minus and plus

sign in the following. After establishing which variables to vary, a response output has to be chosen. This output is the one used to characterize the effect of the variables.

Example of a Two-Level Factorial Design with Two Variables.

In order to explain how the main and interaction effects are found, a two-level factorial design with two random variables, A and B, is established.

The different combinations of high and low values may be presented in a table, see Table 7.1. This virtual analysis needs $2^2 = 4$ simulation runs. The table gives an overview of what variables are used in each simulation run, and how this affects the output response. By interpreting the output from each simulation run, the main effects and the interaction effects can be calculated.

Table 7.1: *Example of a Two-Level Factorial Design with Two Variables.*

Run number	Variable A	Variable B	Response	A × B
1	+	+	Output 1	+
2	+	-	Output 2	-
3	-	+	Output 3	-
4	-	-	Output 4	+
Main effect	Main A (Eq. (7.1))	Main B		Interaction (Eq. 7.2)

The main effect may be explained by looking at how the variation in response changes when moving from the high level to the low level of one single variable. It is a measure of the average effect of one variable over all conditions of the other variables. The main effect of variable A in this case is calculated as:

$$\text{Main effect of variable A} = \frac{(\text{Output 1} + \text{Output 2}) - (\text{Output 3} + \text{Output 4})}{2} \tag{7.1}$$

In Table 7.1, Output 1 and Output 2 represent the output where variable A is at its high level, whereas variable B vary between its high and low level. Subtracting these two outputs from each other yields a difference in the response, going from a high to a low level. Similarly, Output 3 and Output 4 represent the output where variable A is at its low level, and variable B varies. Again, subtracting these two outputs from each other gives a difference in the response when going from a high to a low level. The average of these two differences is called the interaction effect, mathematically given in this case as:

$$\text{Interaction effect A} \times \text{B} = \frac{(\text{Output 1} + \text{Output 4}) - (\text{Output 2} + \text{Output 3})}{2} \tag{7.2}$$

This value supported by an interaction effect plot, seen in e.g. Fig. 7.12a, may be used to interpret how variables interact. In practice, obtaining the interaction effect starts by multiplying the + and - from each variable. The common multiplication rules are valid and a new + and - listing emerges, seen in column number 5 in Table 7.1. The

interaction effect may then be calculated by averaging the outputs related to the + rows and subtracting the average of the outputs related to the - rows.

7.2 Factorial Design of the Component Test

The motivation to conduct a factorial design study was to see which and how variables influenced the coating model. The numerical model of the coating consisted solely of one layer with material properties based on the PP foam. However, the real coating consisted of three layers (of significant thickness) with different material properties.

7.2.1 Choosing the Response Outputs

It was of importance to find a sensible output response that could be used in the further analysis. Two different outputs were chosen, and are explained in the following.

The first output included measuring the lateral displacement at the maximum and minimum point of the test. For the component test, this was done by using DIC and creating a vector at both the maximum and minimum section, illustrated for maximum displacement in Fig. 7.1a. The length of this vector in pixels was converted to physical units of length, lateral displacement in mm in this case. From the FE analysis, the node consisting the maximum and minimum displacement, respectively, was identified and the displacement in the lateral direction logged, see example in Fig. .
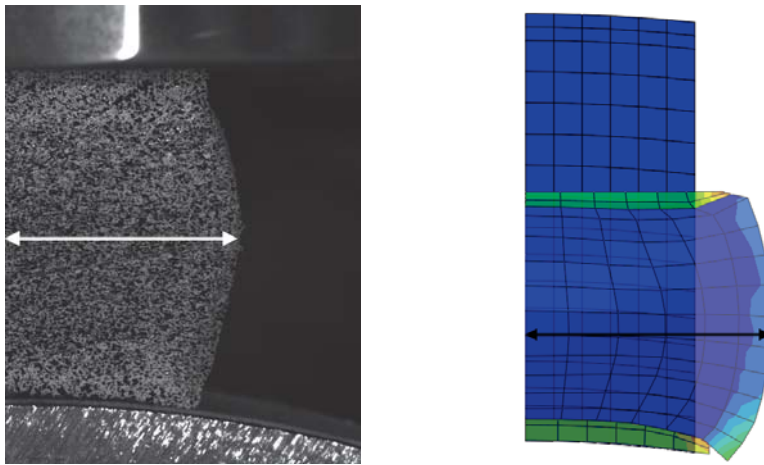
(a) *Maximum displacement for sandwich component*
(b) *Maximum displacement in one of the numerical models*

Figure 7.1: *Illustrations of the maximum lateral displacement of the component and in the FE analysis.*

The lateral displacement was compared at two stages of the compression, namely at 11 and 22 mm. Logging the response from the FE simulations at two different stages of

deformation, both maximum and minimum displacement, gave a lot of data to interpret. Out of these four different outputs, the maximum lateral displacement at 22 mm compression was chosen for further analysis. This output showed the largest trends and was thus easier to present. To relate the response from the FE simulations to the physical compression test, the lateral displacements from the FE simulations were divided by the lateral displacement obtained from the component test. This gave a percentage deviation in the maximum lateral displacement from the component.

The second output was chosen from an energy perspective. The force-displacement curves from the numerical simulations were compared with the force-displacement curve from the experiment, see an example in Fig. 7.2a. The trapezoidal rule was used to integrate the area between the two curves. Regardless of whether the numerical curve was above or below the experimental curve, the area was added up. Solely an energy deviation may be hard to interpret. By dividing the energy deviation by the total displacement, an average force deviation was obtained. An example of how the average force deviation can be illustrated is shown in Fig. 7.2b.
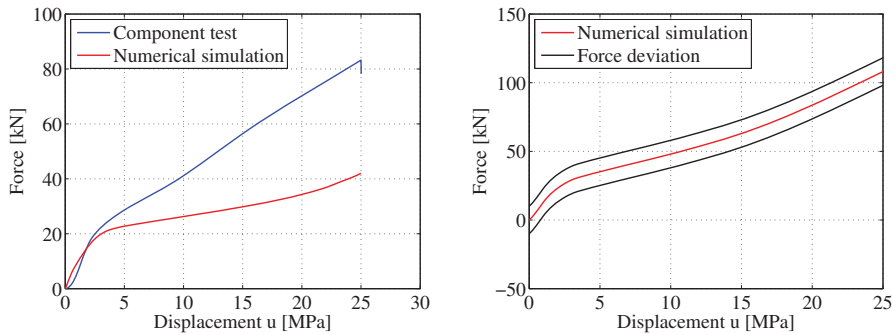
(a) *The total energy deviation is the total area between the curves*

(b) *Average force deviation is the total energy deviation divided by the total displacement*

Figure 7.2: *Illustration of the energy comparison and the average force deviation.*

7.2.2 Choosing the Variables

There were several aspects to take into account when choosing which variables to include in the study. Because of the time frame of the project, a limit of three variables was chosen. Going from e.g. three to four variables would double the number of simulation runs needed. Using three variables also makes it easier to present the results. Further, it was important to choose variables so that they made a difference in the output, but not exaggerating and making one single variable dominant.

Research done by Ilstad and Liu [37], showed that the yield strength of the same type of coating varied a lot in the different tests conducted. To see the importance of this variance, the yield stress, denoted σ_y, was chosen as a variable. Two different levels of the yield stress had to be determined. A high and low value was chosen and can be seen in Fig. 7.3. Fig 7.3b illustrates that the values were made so that they enclosed the

data from the experiments that was used to establish the material model, recall Chapter 5.

(a) *The coating material model and the high and low values of the yield stress*

(b) *The experimental data and the high and low values of the yield stress*
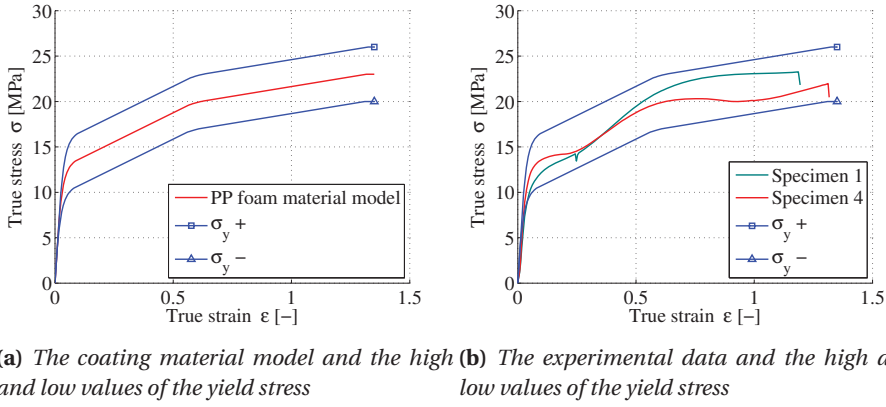
Figure 7.3: *Levels of σ_y compared to the material model and the experimental data.*

The hardening, denoted *H*, of the PP foam material was an important variable to include in the study. One high and low level of hardening was chosen with the similar justification as the yield stress. Fig. 7.4 shows the two levels of hardening. The low level is almost an elastic-perfectly plastic model. The high level is an 30% increased version of the hardening model used in the coating material model. The amount of hardening was also chosen based on enclosing the data equally high and low. Meaning the deviation from the initial material hardening was approximately the same in both extremities.

(a) *The coating material model and the high and low values of the hardening*

(b) *The experimental data and the high and low values of the hardening*
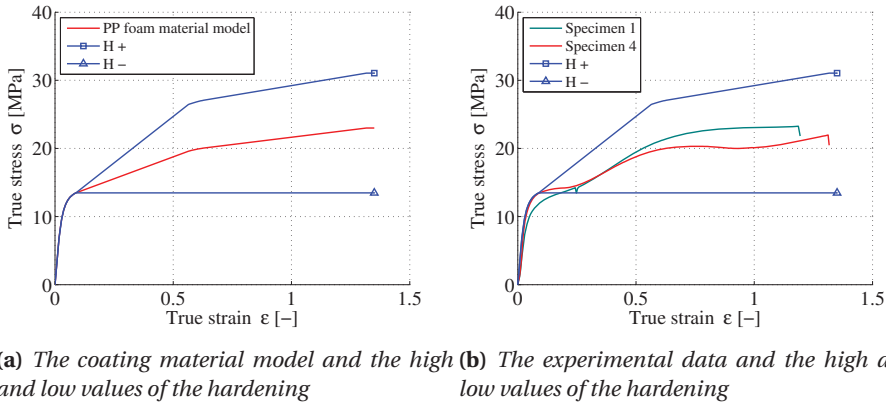
Figure 7.4: *Levels of hardening compared to the material model and the experimental data.*

The coating consisted of one layer with a material model established solely from the PP foam data. It was of great importance to see how using three layers would affect the response. The number of layers, denoted *L*, was the third and last variable chosen. The

high and low value of this variable, was simply going from three to one layer, defining this as a qualitative parameter. The two different models are shown in Fig. 7.5. Material models obtained from Polanco-Loria [31] were used for the outer and inner layer. These layers were both characterized as significantly stiffer than the PP foam. The outer shield layer was 3 mm and the inner solid PP layer was 6 mm.

(a) *Low level layer, L-*   **(b)** *High level layer, L+*
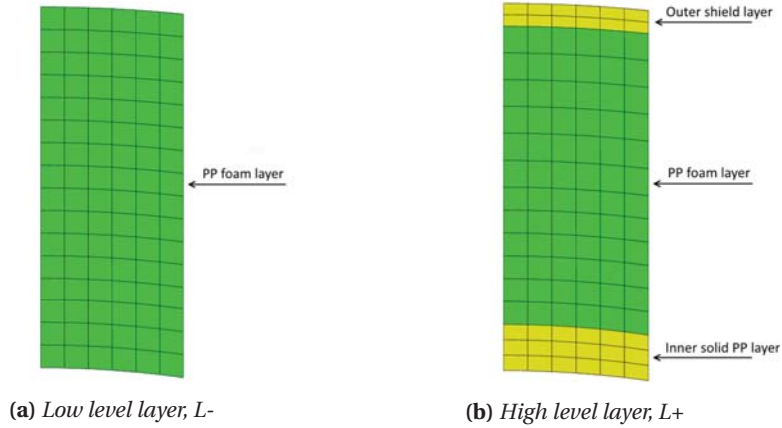
Figure 7.5: *Explanation of the high and low level of the layer variable.*

7.2.3   Sources of Error

Several aspects about the numerical model may have introduced errors or had a bad effect on the results. As seen in Fig. 7.6, the deformation shape in the model was highly dependent on conducting the analysis with one or three layers.

(a) *Run with three layers, L+*   **(b)** *Run with one layer, L−*
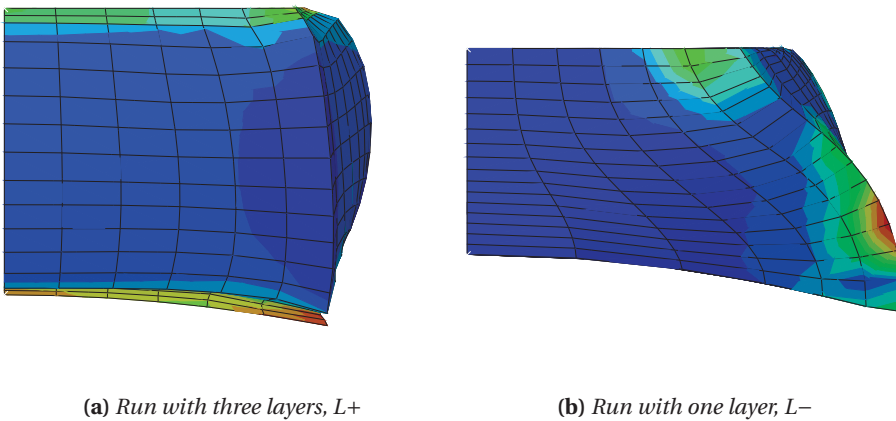
Figure 7.6: *Lateral deformation pattern obtained in FEM analysis for different levels of layers.*

When utilizing only one layer, the foam would expand along the bottom plate, rather

than obtain the barreling effect seen in the experiments. A possible way to avoid this could have been to increase the friction coefficient between the bottom plate and the coating. In retrospect, the friction that was present in laboratory was probably higher than the one used in the numerical model ($\mu = 0.025$). Without having the stiffer outer layers holding it together, it could seem like the foam did not obtain the deformation pattern from the experiment. Fig. 7.6a shows the result containing three layers, and how the stiff outer layers made it barrel, rather than expand along the bottom steel plate.

In the two different models, the foam layer does not have the same size. The foam makes up 100% of the height when having one layer, and about 80% of the height when having three layers, while the total height is the same. Altering the hardening and yield stress in the model with only one layer has a bigger impact than altering the variables on the three-layer model. I.e. since it is the foam material properties that is being varied, the alteration does not affect the same amount of volume in both cases.

It is assumed that the volume is preserved in the numerical model, although this is probably not reality. The pores in the material which contained air, were probably compressed and this was not taken into account in the material model.

Creating a vector that went exactly from edge to edge in the pictures from the experiment, yielded a source of error as well.

7.3 Results and Discussion

In this section the resulting output responses will be presented and discussed. The factorial design was done in the statistical software Minitab [38] and the plots are generated with the same program.

7.3.1 Percentile Deviation from Maximum Lateral Displacement

In Table 7.2 the results from the simulation runs are presented. The + and - signs denote the high and low level of each variable. From the table both the main effects and interaction effects can be seen on the bottom row. The output in this table is the percentile deviation of the maximum lateral displacement obtained from the experimental data. The lateral displacement from the numerical models were all larger than the one from the experiment.

A cube plot for the different responses is shown in Fig. 7.7. A cube plot is a way to present the output in a way that visualize both the main effects and interaction effects. Each corner represents the response that was obtained from the combination of levels at this corner. Moving along one axis makes it easier to establish trends and interpret the output response.

Table 7.2: *Results from the percentile deviation in width output.*

					Interaction effects		
Run number	**L**	**σ_y**	**H**	**Output [%]**	**L × σ_y**	**L × H**	**σ_y × H**
1	+	+	+	8.4	+	+	+
2	+	+	-	2.6	+	-	-
3	+	-	+	2.7	-	+	-
4	+	-	-	9.2	-	-	+
5	-	+	+	14.4	-	-	+
6	-	+	-	24.9	-	+	-
7	-	-	+	13.5	+	-	-
8	-	-	-	24.0	+	+	+
Main Effects	-13.5	0.3	-5.4		-0.7	5.1	3.1
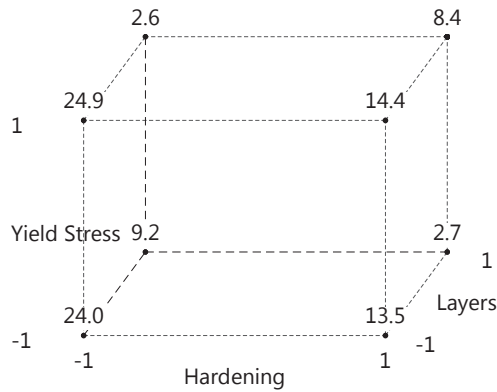
Figure 7.7: *Cube plot.*

Main Effects

In Table 7.2 the main effects can be found at the bottom row. The main effect for the yield stress is small and close to zero. This means that the average response whether the yield stress is high or low is approximately the same. This can also be seen by looking at how the middle line in Fig. 7.8 is almost constant regardless of level.

On the other hand, the main effect for the layer is relatively big at -13.5. Going from a high to a low level yields a significantly lower deviation in width. This can be underlined by looking at the right part of Fig. 7.8, and how far the points are apart going from the low to the high level. The main effect for the hardening (-5.4), shows a vague but present trend that increased hardening yields a smaller deviation on average.
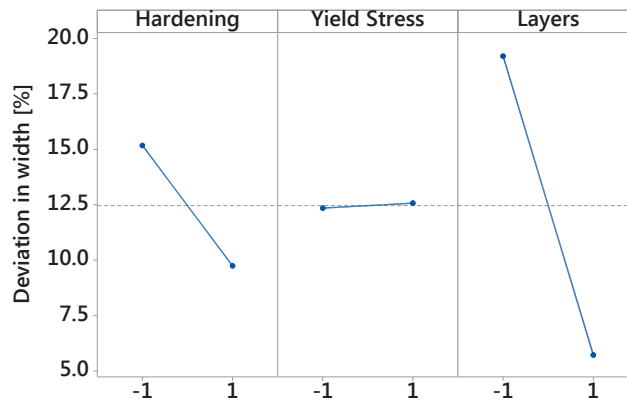
Figure 7.8: *Visualisation of the main effects for deviation of the maximum lateral displacement output.*

Interaction Effects

Fig. 7.9a shows how the layer and yield stress parameter interact. Moving along the horizontal axis means moving from a low to a high level of the yield stress. Looking at the blue curve it can be seen that whether the yield stress is at a high or low level, the response is approximately the same. A low or high value of the layer variable was what dictated the response, regardless of the yield stress. A three-layer model yielded a much smaller maximum lateral displacement than the one-layer model. Supported by both Fig. 7.9a and the interaction effect being 0.3, the interaction between the two can be seen as almost non existent.

The interaction between the number of layers and the level of hardening is shown in Fig. 7.9b. The blue curve shows how varying the hardening, while having a model with only one layer, changed the response. An increased hardening gave a markedly smaller lateral displacement. The red curve shows how the response varies when increased hardening is introduced on the three layer model. The response changed marginally going from the low to the high hardening. It may seem like the hardening had an impact together with the one-layer model. However, combined with the three-layer model the hardening did not seem to dictate the response to the same extent. This means that the response is approximately the same regardless of the two levels of hardening when having a three-layer model. As seen in the previous interaction plots as well, introducing three layers once again yielded a result that is closer to the experimental data. It may seem like the increased hardening holds the sandwich tighter together when the outer layer and inner layer are absent.

Fig. 7.9c shows how the hardening and yield stress interact. Regardless of the yield stress, having an increased hardening gave a better result. When the hardening was low, an increased yield stress only gave a marginally better result. At a high level of hardening, increasing the yield stress actually gave a bigger deviation than at a low yield stress. The reason is unclear.
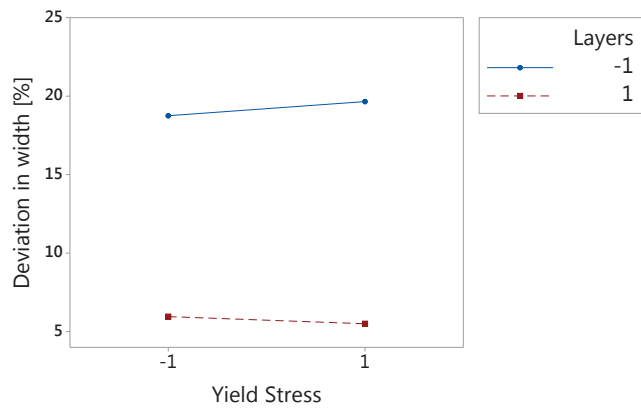
(a) *Yield stress and Layers*
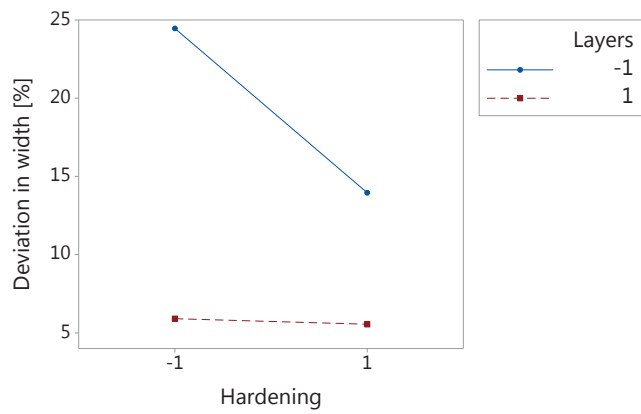
(b) *Hardening and Layers*
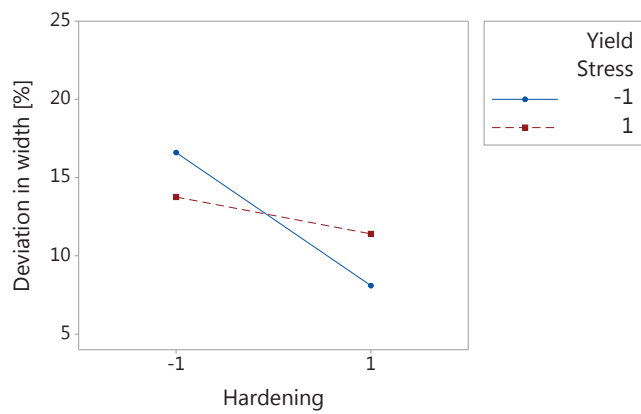
(c) *Hardening and Yield Stress*

Figure 7.9: *Interaction effects for the deviation of the maximum lateral displacement.*

7.3.2 Average Force Deviation

In Table 7.3 the results from the test runs are presented. The + and - signs denote the high and low level of each variable, respectively. The output in this table is the average force deviation from the experimental results.

Table 7.3: *Results from the average force deviation output.*

					Interaction effects		
Run number	L	σ_y	H	Output [kN]	L $\times$ σ_y	L $\times$ H	$\sigma_y \times$ H
1	+	+	+	9.6	+	+	+
2	+	+	-	10.4	+	-	-
3	+	-	+	4.1	-	+	-
4	+	-	-	20.5	-	-	+
5	-	+	+	6.5	-	-	+
6	-	+	-	12.4	-	+	-
7	-	-	+	8.3	+	-	-
8	-	-	-	23.6	+	+	+
Main Effects	-1.6	-4.4	-9.6		2.1	1.0	6.3

The cube plot in Fig. 7.10 illustrates the results as well.
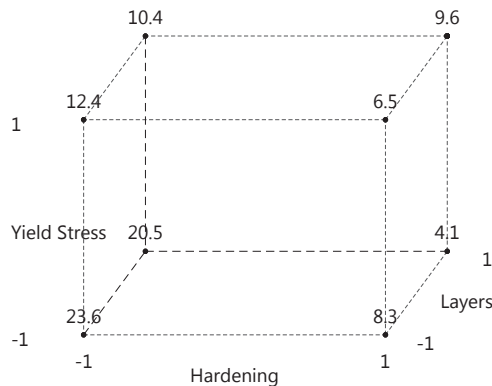
Figure 7.10: *Cube plot of the average force deviation.*

Main Effects

The main effect for the three variables can be seen in Table 7.3 and Fig. 7.11. On the basis of the main effects, the layers seemed to have the lowest effect on the energy aspect with a main effect of 1.6. Both the yield stress and hardening variable had a relatively high main effect, at 9.6 and 4.4. This means that using a high level of these two variables gave less deviation in the average force throughout the numerical simulation. In

the cube plot in Fig. 7.10, the left and right side represents high and low hardening, respectively. By comparing the left side to the right side, the main effect of the hardening can be seen. The left side has a distinctively higher deviation than the right side. The most severe response is seen when both yield stress and hardening are low. Merely by looking at the cube, the layer variable seemed to have less impact on the output in general.
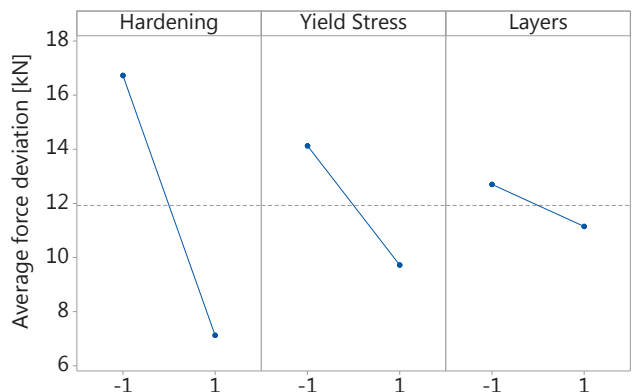
Figure 7.11: *Main effects for the average force deviation output.*

Interaction Effects

In Fig. 7.12a the interaction between the yield stress and the layers is shown. A high level of the layer variable combined with a high level of yield stress gave a smaller deviation. The importance of using the one-layer model or three-layer model seemed to be dependent on the yield stress. This can be seen by inspecting the plot where the yield stress has a low value. Introducing three layers at this point gave a smaller deviation. However, when the yield stress was high, the response seemed independent of having one or three layers.

The interaction between the hardening and layers can be seen in Fig. 7.12b. A high level of hardening improved the response greatly. The level of layers did not seem to impact the response significantly. Going from one to three layers had the lowest impact at the high level of hardening. Both lines, each representing different levels of layers, gave somewhat the same result. This means that the layer variable had little impact on the energy aspect. The interaction between the two variables was small and had a value of 1 kN.

The yield stress and hardening were the two variables that showed the largest interaction, with an interaction effect of 6.1. Looking at the interaction plot, there are several aspects to discuss. When the hardening was at its low level, increasing the yield stress from high to low gave a big impact on the average force deviation. However, when the hardening was at its high level, increasing the yield stress actually gave a bigger average force deviation. This means that a high level of hardening with a low yield stress,

gave an energy curve that was more similar to the one obtained from the experimental data.
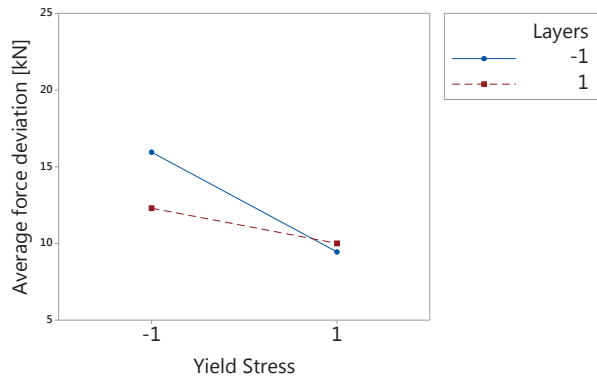
(a) *Yield stress and Layers*
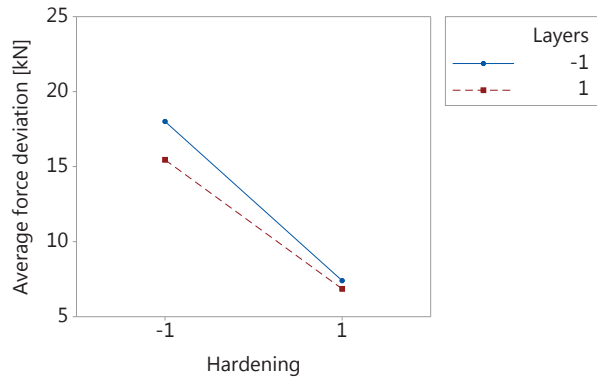
(b) *Hardening and Layers*
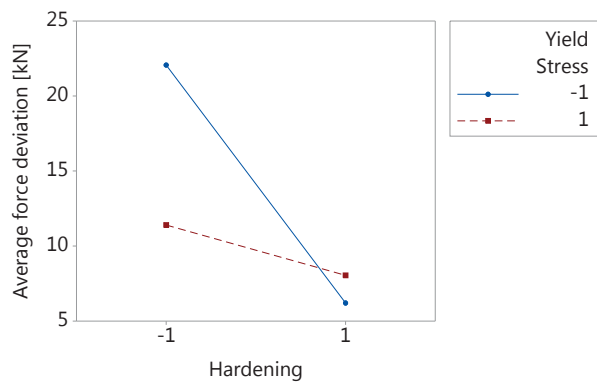
(c) *Hardening and Yield Stress*

Figure 7.12: *Interaction effects for average deviation in force.*

7.4   Concluding Remarks

When using the initial material model based on the PP foam for the component sandwich, the force-displacement curve was found to underestimate the response. Therefore, the result showing that increased hardening and yield stress gave a better correlation with the experiment was expected to some extent. It was nonetheless important to get a better understanding in the numerical study and quantify the effect.

When defining the high and low level of the three variables, the levels were chosen based on enclosing the data in both extremities. A smaller deviation from the initial material model could possibly give different results if the values were more or less exaggerated.

The important thing in the factorial design was not to alter the numerical simulations to fit the actual response. The motivation was to see the *change* in varying the different variables, and how they possibly interacted together.

Polymers in compression may have pores filled with air that compress and change the volume of the polymer throughout the test. The numerical model did not include this potential change in volume.

A few results are summarized below.

- Increased hardening had a larger effect on the maximum lateral displacement when utilized with the one-layer model than with the three-layer model.

- The lack of friction may have played an important role in the maximum lateral displacement comparison.

- Increased yield stress had little influence on the maximum lateral displacement.

- Using one or three-layers did not change the average force deviation significantly.

- To obtain the barreling effect the three-layer model had to be utilized.

8 | Numerical Simulations

In order to get a better understanding of the denting of the pipes, numerical simulations were of interest. Creating a robust model of the coated pipes, would give an important base for further discussions and parameter studies.

The Finite Element Analysis (FEA) program Abaqus/Explicit was used for this purpose. Due to the big displacements and large plastic deformation in the coating, it was expected that the coated pipes would be harder to simulate compared to the uncoated ones.

Simulations of the uncoated steel pipes were pretty straightforward and the results correlated well with the experimental data. However, the coated pipes were more complicated. Severe contact and distortion issues were still a problem after more than 60 different simulations. Unfortunately, the simulations did not render a good result.

8.1 General Set-up

This section contains information which is consistent for all the simulations unless otherwise is specified later in the chapter.
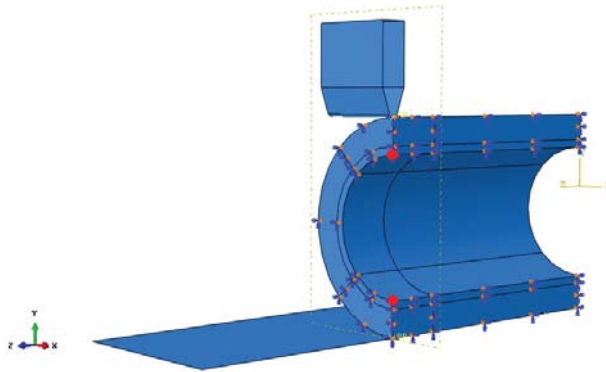

Figure 8.1: *General set-up of the numerical models.*

The model consisted of three parts: the rigid indenter, the rigid base plate and the pipe itself as shown in Fig. 8.1. The z-axis ran along the pipe's longitudinal axis and together with the x-axis, created the horizontal plane. The y-axis was normal to this plane.

The indenter could only move in the y-direction and was given a time scaled displacement. The displacement amplitude was done with a smooth step to damp dynamic effects as much as possible. The step time was between 0.1-0.3 s, depending on the total displacement for each analysis. The geometry of the indenter can be found in Fig. 6.3 in Chapter 6. The same base plate and indenter were used in all the simulations, regardless of whether the pipe was modelled as a quarter pipe or half a pipe. Hence, one plane of symmetry was exploited when creating the indenter and the base plate. The base plate and the indenter was given a mass of 250 kg to prevent an ill-conditioned mass matrix. For the base plate all 6 degrees of freedom were fixed.

For the pipe itself, standard reduced integration elements C3D8R were utilized. The geometry for pipe S and pipe L with and without coating is found in Appendix-A. To save CPU-time, exploiting both one and two planes of symmetry to create the model was done. The models of $\frac{1}{2}$ and $\frac{1}{4}$ of the pipe were used depending on different problems occurring during the simulations. After some experience, only $\frac{1}{4}$ of the pipe was used in the simulations. The boundary conditions used for the pipe were x- and z-symmetry.

The simulations in this chapter were run with the dynamic explicit solver because of the amount of non-linearity and contact in the problem. The dynamic effects are also taken into account using this solver. To be able to compare the results obtained in the simulations, reaction force and displacement in the y-direction were taken from the indenter. Displacement was also taken in the y-direction from the inner pipe nodes, indicated with red dots in Fig. 8.1. The deformation of the node at the bottom was subtracted from the deformation of the node at the top. This was done to calculate the inner displacement of the pipe, in the same way it was measured in the experiments.

8.2 Pipe without Coating

Pipes without coating have been simulated numerous times before in previous master's theses. Creating a good model was fairly straightforward.

8.2.1 Numerical Model

How the model is divided in segments and an example of the mesh of pipe S can been seen in Fig. 8.2. Specifics about the mesh can be read in Table 8.1. The basis model was modeled with the penalty contact method.

(a) *Mesh segments*

(b) *Mesh of pipe S*
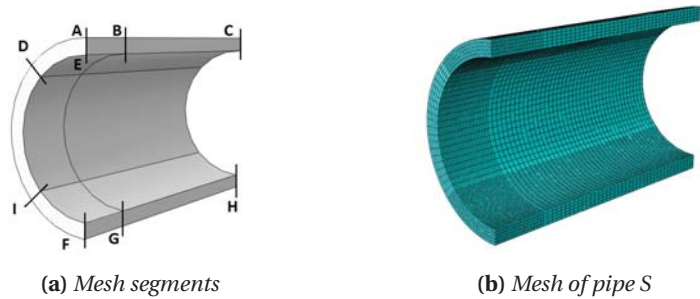
Figure 8.2: *Illustration of mesh segments and mesh of bare steel pipes.*

Table 8.1: *Mesh information of steel pipe S and L.*

	Pipe S and pipe L		
Segment	**Segment size**	**# of elements**	**Uniform or bias**
AB	100 mm	26	Biased (3mm-5mm)
FG	100 mm	26	Biased (3mm-5mm)
BC	400 mm	40	Uniformed
GH	400 mm	40	Uniformed
AD	45 °	20	Uniformed
IF	45 °	20	Uniformed
DI	90 °	20	Uniformed
AE	14.3 and 25.5 mm	5	Uniformed

8.2.2 Results

As seen in Fig. 8.3 and 8.4, the numerical models showed good agreement with the experimental tests.
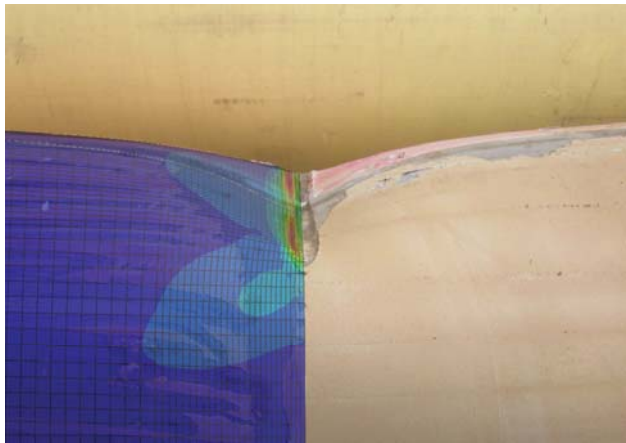
Figure 8.3: *Mesh and deformation of pipe S*
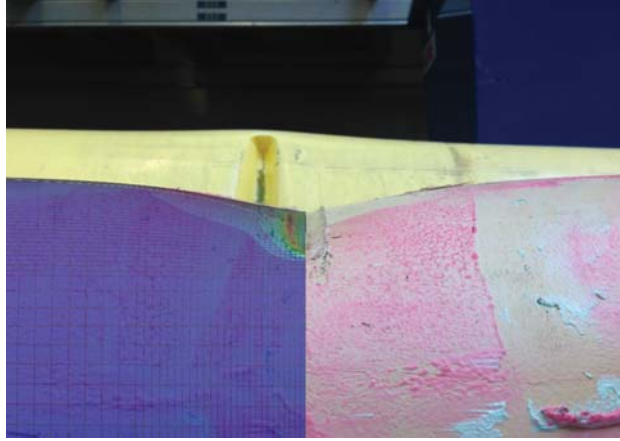
Figure 8.4: *Mesh and deformation of pipe L*

The force-displacement curves for pipe *S* correlated well with both the inner and the outer displacement of the experiments, see Fig. 8.5. Inspecting the force-outer displacement for pipe *L*, the simulation overestimated the experiment towards the end, as indicated in Fig. 8.6a. For the force-inner displacement, the response from the simulations was a little too stiff in general, see Fig. 8.6b. These deviations may come from some kinematic hardening in the steel from the loading and unloading. The deviation may also come from some difference in the thickness of the modeled pipe compared to the real pipe.

Two new models were made to exclude some possible numerical explanations for this deviation. A remeshed model with 8 elements over the height instead of 5, as well as a simulation where the contact method was changed from penalty to kinematic contact were conducted. These results are shown in Fig. 8.6a. They did not yield different results, and the original model was employed when simulating pipe *L* with coating.

(a) *Force - outer displacement of pipe S*

(b) *Force - inner displacement of pipe S*
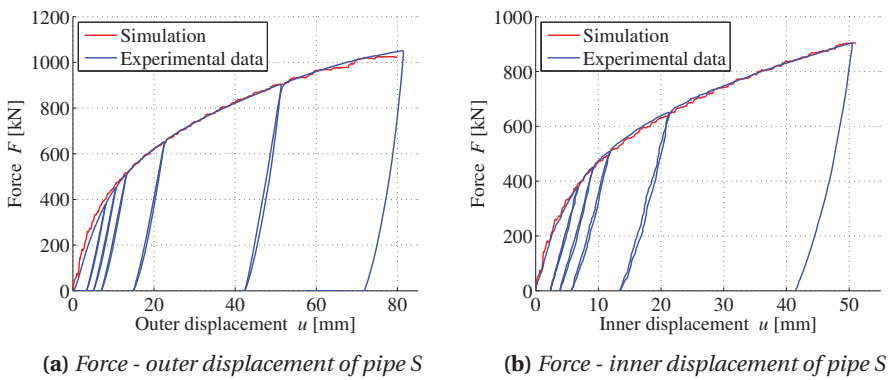
Figure 8.5: *Simulation versus experiment of pipe S.*

(a) *Force - outer displacement of pipe L* (b) *Force - inner displacement of pipe L*
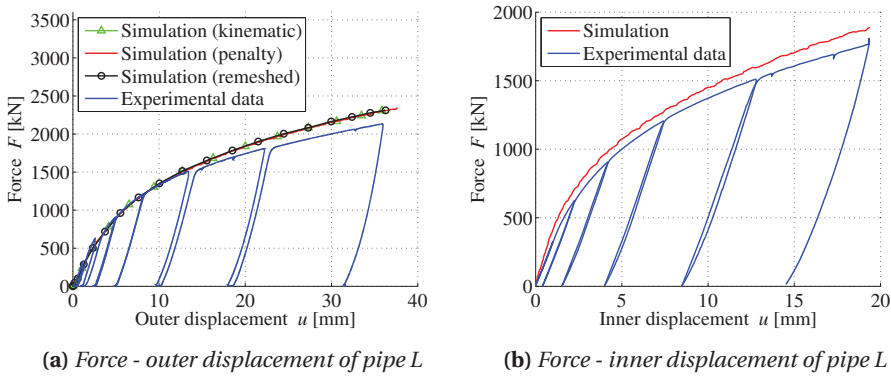
Figure 8.6: *Simulation versus experiment of pipe L.*

8.3 Pipe with Coating

Creating a numerical model for the pipes with coating was more challenging. This section consists of a recapitulation of the steps towards finding a satisfactory numerical model and the results of the analysis carried out.

8.3.1 Numerical Model

Introduction to the Problem

From the experiments conducted in the laboratory, some physical obstacles for the numerical simulations were obvious:

- The coating thickness was relatively large. 48 mm for pipe *S* and 80.4 mm for pipe *L*. The big deformations in the coating could create numerical problems in the simulations.

- The coating consisted of several layers with different material properties.

- Because the diameter of the coated pipes was bigger than the length of the indenter, the indenter did not only dent the coating, but also cut into it, see Fig. 8.7a.

- The coating fractured during the tests, see Fig. 8.7b.

The model of the pipes was created as one part with two layers. A layer of steel and a layer of coating, both based on the material models for each respective material from Chapter 5. The indenter was made discrete rigid to create a closed solid part, see Fig. 8.8a. Another option was to to create the indenter analytical rigid as seen in Fig. 8.8b. However, analytical rigid indenter is not closed at all four sides. This could have created contact problems at the back where the indenter cuts into the coating.

(a) *Penetration of the indenter*   **(b)** *Fracture of the coating*

Figure 8.7: *Penetration and fracture of the coating.*
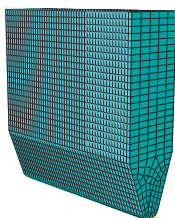
(a) *Discrete indenter*   **(b)** *Analytical indenter*
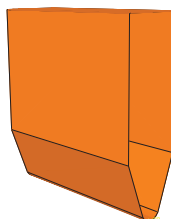
Figure 8.8: *The two types of the rigid indenter used.*

First Models and Contact Problems

Fig. 8.9 shows the first model made. A closer look at the deformation showed a lot of mesh distortion from the big deformations, see Fig. 8.10a.

The next model had a refined mesh and created with the Arbitrary Lagrangian-Eulerian formulation (ALE). As see in Fig. 8.10b, ALE improved the mesh significantly in longitudinal symmetry plane of the pipe. It is worth noting that in the comparison in Fig. 8.10a, the mesh size is not the same. This may have contributed in creating a better mesh as well. However, the refinement of the mesh and the use of ALE did not solve the contact problems that occurred at the back where the indenter cut into the coating.

(a) *Before deformation*   **(b)** *After deformation*
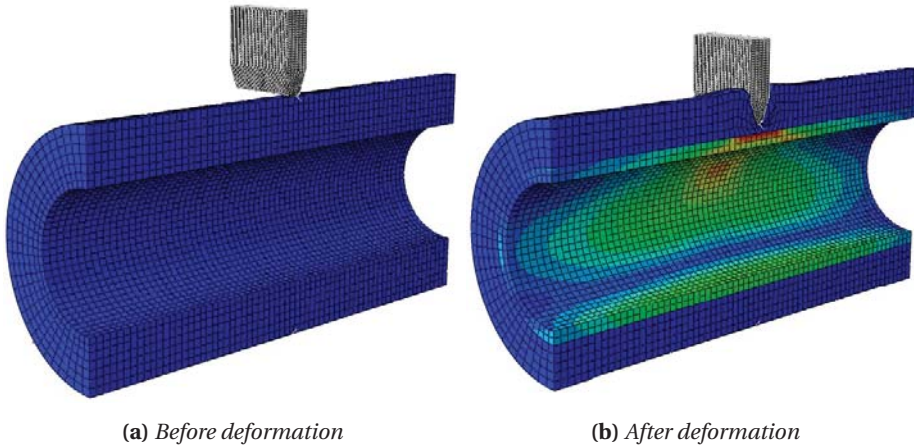
Figure 8.9: *The first pipe model.*

(a) *Without ALE*   **(b)** *With ALE*
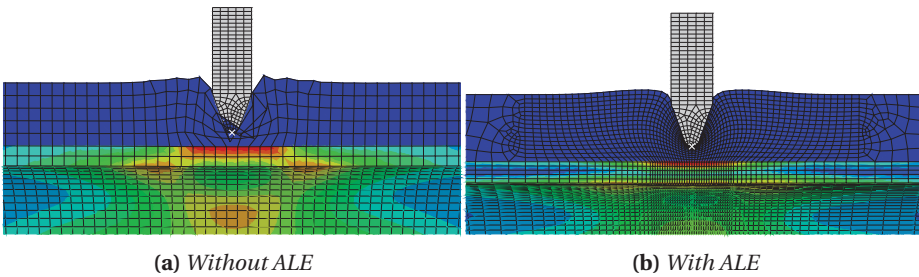
Figure 8.10: *A clear difference in the mesh with and without ALE.*

Fig. 8.11 shows the back of the pipe when the simulation terminated. The critical distorted element is marked in red. Refining the mesh gave simulations with a CPU-time of 10 hours and ODB-files in the size range of 1-2 GB. However, it did not solve the problem entirely. Neither enlarging nor increasing the area of the ALE mended the problem. Nor did changing the frequency of remeshing for the ALE area.

(a) *Contact problems behind the indenter*   **(b)** *Distorted element in red*
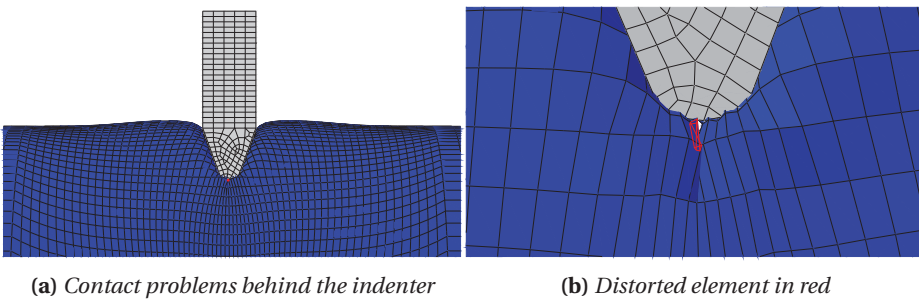
Figure 8.11: *ALE created distorted elements behind the indenter.*

The contact properties was changed from surface-to-surface, to general contact: all-with-self. The fracture criterion Johnson-Cook was employed to provoke fracture in the coating. Setting the Johnson-Cook input parameter $d1 = k$ and the rest to 0 made equivalent plastic strain, PEEQ, the only thing generating fracture. This implicates that the fracture criterion was simply a constant strain failure criterion. Since the Johnson-Cook criterion was well established in Abaqus/Explicit, the constant strain failure criterion was employed by altering the input parameters in the already established Johnson-Cook formulation. This way fracture should occur in the elements when $PEEQ = k$. In the following section when the Johnson-Cook formulation is mentioned, it is merely a constant strain failure criterion that is employed.

(a) *d1 = 1. Too many elements deleted*   **(b)** *d2 = 2. No elements deleted*
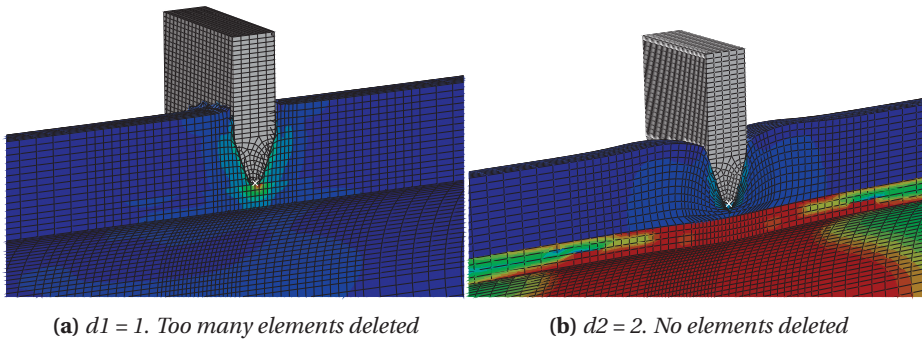
Figure 8.12: *Simulations with Johnson-Cook damage criterion.*

Either too many elements or none were deleted when employing the fracture criterion. This is illustrated for two different values of the failure strain in Fig. 8.12. Tuning the PEEQ to delete a sensible amount of elements was hard. It seemed that Abaqus/Explicit deleted "all or nothing". The failure criterion was eventually removed completely when it was understood that the Johnson-cook formulation does not work with the surface-to-surface contact algorithm, as explained in the next paragraph.

Employing the fracture criterion, while at the same time changing the the contact algorithm turned out to be a mistake. ALE can not be used in combination with general contact: all-with-self, only surface-to-surface [21]. With Johnson-Cook it is the complete opposite. Johnson-Cook need to be used with general contact: all-with-self because when elements at a surface is deleted, contact needs to be defined for the elements underneath [39]. This was not known beforehand and it created a lot of confusion about whether or not ALE was actually implemented in a lot of the simulations.

Fig. 8.12b shows a simulation where $PEEQ = 2$ and the ALE remeshing technique was employed. However, one of the reasons for the confusion in whether the ALE actually worked or not is explained in the following. Looking at the mesh at the final deformation step, it was hard to see if the result came from the fact that Johnson-Cook and ALE in the same analysis was a bad combination, or whether the ALE technique was excluded from the analysis due to the fracture criterion.

This confusion also created a lot of problems when trying to solve the problem of the distorted elements. An attempt to deal with this, was done by only simulating $\frac{1}{4}$ of the

pipe. Hourglass modes and distortion under the indenter became a big problem without ALE, as seen in Fig. 8.13. This problem was tried mended by different hourglass controls and different coefficients of distortion control with no success. The fully integrated version of the elements, C3D8, were not an option as they are not compatible with explicit analyses [40].

(a) *Hourglass and distortion 1*   **(b)** *Hourglass and distortion 2*
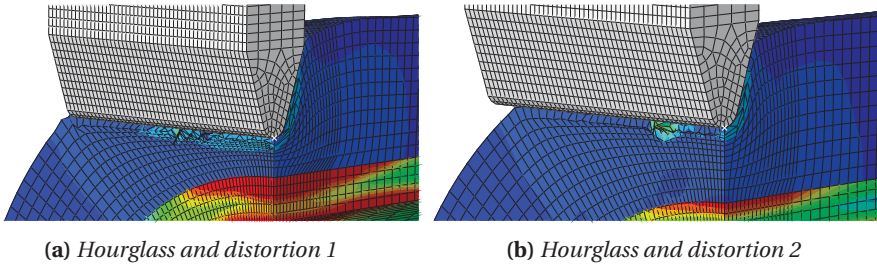
Figure 8.13: *Hourglass and distortion under the indenter.*

The problems at the back of the indenter were solved with general contact: all-with-self. As mentioned earlier, ALE could not be employed with general contact and this was something that caused a bad mesh.

Another contact algorithm called self-contact, was tried in an attempt to solve the problem. A combination of the Surface-to-surface algorithm and the self-contact algorithm was therefore attempted. However, as Fig. 8.14 shows, self contact did not render the same deformation as general contact: all-with-self and elements still became distorted.

(a) *Deformation using all-with-self contact*   **(b)** *Deformation using self-contact*
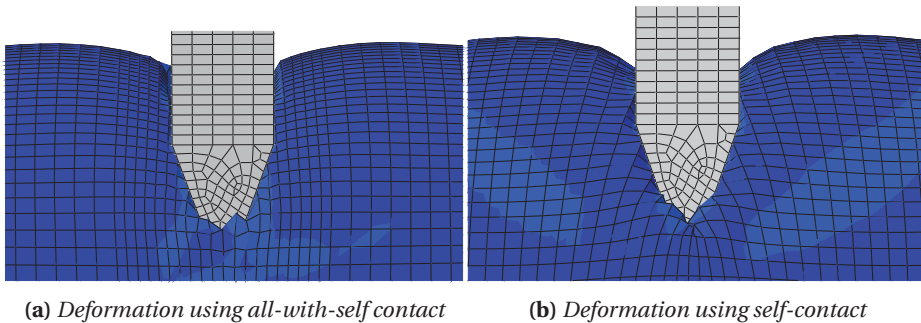
Figure 8.14: *Different deformation when using all-with-self versus self-contact.*

To simulate the front area where the indenter hits the pipe with surface-to-surface, and the rest with general contact: all-with-self was tried as well. Fig. 8.15 shows the result which was better than the previous results, but not satisfying.
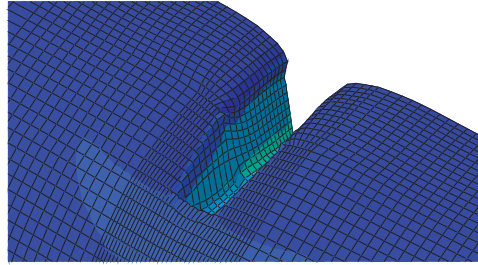
Figure 8.15: *Deformation using all-with-self and surface-to-surface.*

A summary of the contact methods and which problems they solved and created can be seen in Table 8.2.

Table 8.2: *Pros and cons with different contact algorithms.*

Contact algorithm	Pros	Cons
Surface-to-surface	Could use ALE	Distorted elements where indenter cut into coating
General contact: all-with-self	No distortion where indenter cut into coating	Does not work with ALE
Surface-to-surface + self-contact	Could use ALE	Distorted elements where indenter cut into coating
General contact: all-with-self + surface-to-surface	Could use ALE in some areas. No distortion where indenter cut into coating	The mesh was not as good as it should be

Simulation Techniques from the Statoil Report

A report [37] from Statoil on simulation techniques of coated pipes became available. The report consisted of simulations on a similar pipe, only with a thinner layer of coating. A pipe with the same geometry and properties was attempted to simulate to see if it coincided with the report.

The indenter was made analytical rigid as opposed to discrete rigid in hope of improvement concerning the contact problems. By using a thinner layer of coating and with ALE, it was possible to get basically the same visual deformation as the one obtained in the report from the Statoil. However, the force-displacement curve was not completely the same. The distinct kink from when the indenter hits the steel was missing. This might have had something to do with the penalty contact method, since the coating is penetrating the indenter. The coating did not penetrate the indenter if the kinematic contact method was used. However, with the kinematic contact method, the simulation terminated when the indenter hit the steel. Fig. 8.16 shows how the simulation looks like with both the kinematic and penalty method at their termination point.

(a) *Simulation with kinematic contact*   **(b)** *Simulation with penalty contact*
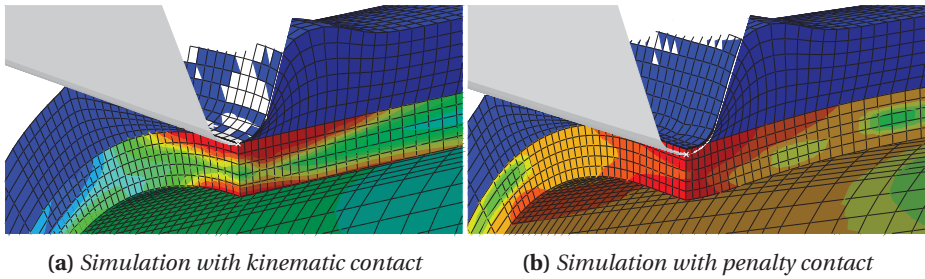
Figure 8.16: *Simulations of pipes with thinner layer of coating.*

The force-displacement curves from both simulations can be seen in Fig. 8.17. It could seem like the simulation with the kinematic contact experienced some numerical instabilities. The curve from the penalty method is smooth, however it lacks the distinct kink found in the experiments seen in Chapter 6 (and in the Statoil Report).
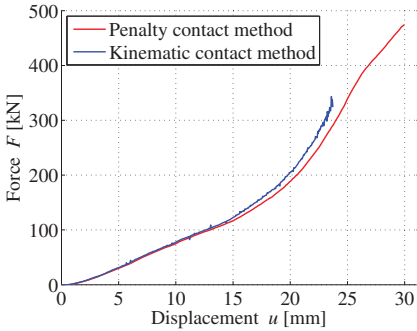
Figure 8.17: *Force - displacement from simulations of pipe with thinner coating.*

The Final Models

The numerical models of the coated pipes were divided into segments and meshed with different properties found in Fig. 8.18 and in Table 8.3. Some abbreviations were made in the table: seg.=segment and el. = element.
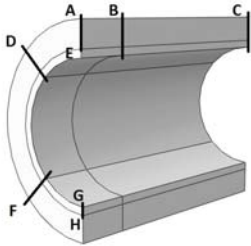
Figure 8.18: *Mesh segments for the coated pipes.*

Table 8.3: *Mesh information of coated pipe S and L.*

	Pipe S			Pipe L		
Seg.	Seg. size	# of el.	Uniform/bias	Seg. size	# of el.	Uniform/bias
AB	100 mm	26	Biased	150 mm	26	Biased
BC	400 mm	40	Uniformed	350 mm	35	Uniformed
AD	45 °	30	Uniformed	45 °	30	Uniformed
DF	90 °	20	Uniformed	90 °	20	Uniformed
AE	48 mm	15	Uniformed	80 mm	20	Uniformed
GH	14.3 mm	5	Uniformed	25.5 mm	5	Uniformed

Fig. 8.19 shows pipe *S* simulated with both the penalty and kinematic contact method. Problems occurred when simulating with the penalty contact method, and can be seen in Fig. 8.19a. The coating went through the indenter walls and the steel. This made the simulations terminate because of distortion of coating elements between the indenter and the steel. In the simulations with the kinematic contact method, as seen in Fig. 8.19b, the coating elements do not go through the indenter. However, the problem with distortion of elements before the indenter hit the steel was still present. Examples of these distorted elements can be seen in Fig. 8.20.

(a) *Penalty. Elements penetrates the indenter*   **(b)** *Kinematic. Contact problems by indenter*
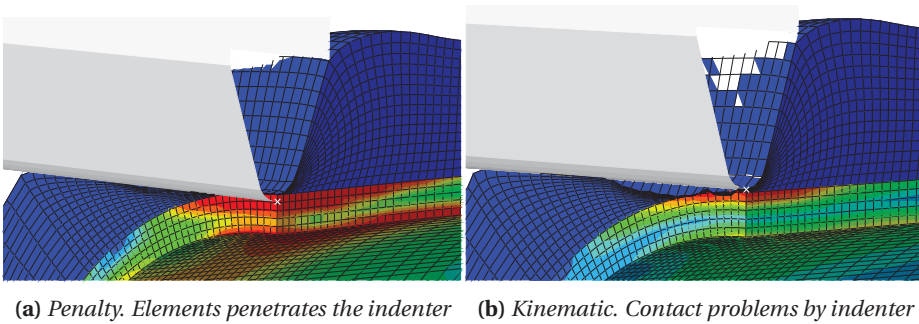
Figure 8.19: *Pipe S. Penalty and kinematic contact creates different problems.*

Remedies tried without any success:

- Scaling the critical time step with factors of 0.75, 0.6 and 0.5.

- Defining the area of the pipe where the indenter hit the coating as a node region instead of a surface.

- Changing distortion control from default to off.

- Letting the indenter have a constant speed instead of constant deformation. This created a high peak force at det start of the simulations, probably because of dynamic effects.

- For the penalty contact method; changing the weighting factor from default to 1.

- Changing the initial mesh sweeps, number of mesh sweeps and frequency of the sweeping for the ALE. The inital values were: initial mesh sweeps = 100, number

of mesh sweeps = 3 and frequency = 5.
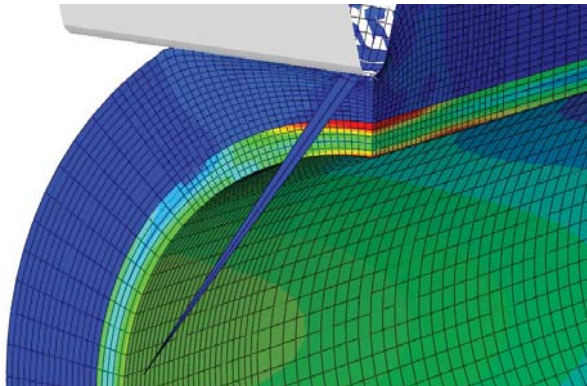
(a) *Distorted element.*
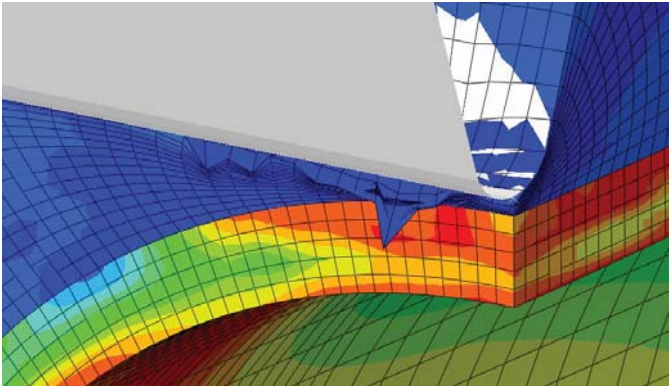
(b) *Distorted element 2*
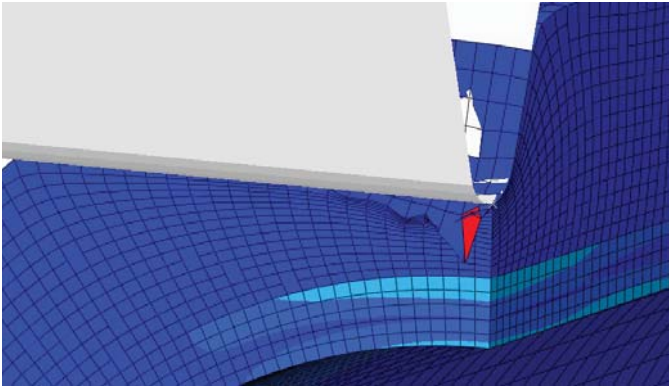
(c) *Distorted element 3*

Figure 8.20: *Typical kinematic contact problem for different simulations. In theses cases, different scaling of the critical time step was employed.*

8.3.2 Results

An overview for the finished simulation of pipe *L* can be seen in Fig. 8.21. As indicated, the simulation stopped for both pipe *S* and pipe *L*, when the indenter penetrated the steel. Fig. 8.22b shows a close up of the indenter at the point in the simulation where it terminates. Since the problem was the same for both pipes, pipe *L* was chosen for illustration. In Fig. 8.22a it can be seen that distorted elements behind the indenter was no longer an issue. However, the simulations did not cut into the coating as seen in the experiments, recall Fig. 8.7a.

(a) *Overview*   **(b)** *Close up*
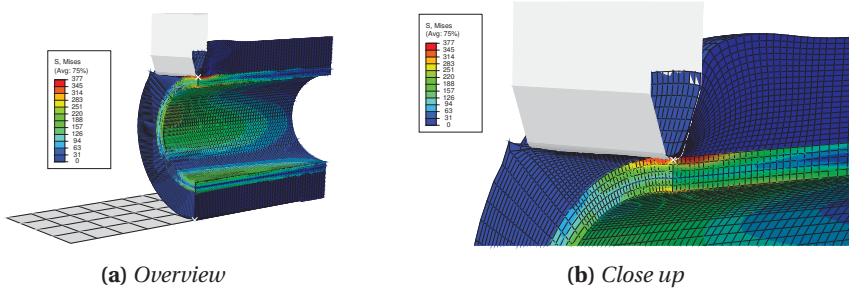
Figure 8.21: *Simulation of pipe L with coating.*

(a) *Behind the indenter*   **(b)** *Problems with penalty contact*
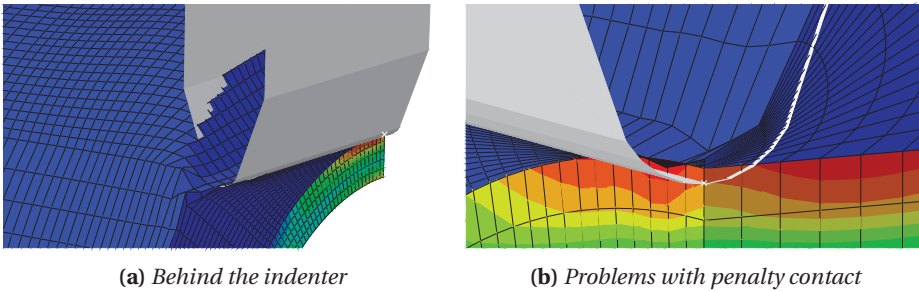
Figure 8.22: *Close up of simulation of pipe L with coating.*

The force-displacement curves from the experiments and simulations of pipe *L* and *S* can be seen in Fig. 8.23 and Fig. 8.24, respectively.

The force-outer displacement of pipe *L* in Fig. 8.23a shows how the model underpredicted the strength of the coating. This may indicate that yield stress and the hardening in the material model is a little low. An indicitation of this was also discussed in the Factorial Design, see Chapter 7. However, in the beginning of curve, the simulation overestimated the experiments. This probably comes from contact issues at the start of the simulation. The simulations terminated almost at the same displacement and same force level as where the indenter hit the steel in the experiments.

The force-inner displacement of pipe *L* from the numerical simulation is seen in Fig. 8.23b. The curve followed the experimental curve to some extent up until the analysis got terminated. Most of the inner displacement of the pipe occurred after the indenter had cut through the coating. Hence, it seemed valid that the simulations terminated at

an inner displacement of about 3-4 mm. The same effect can be seen for the force-inner displacement from pipe *S* as well, Fig. 8.24b.

Simulations with both penalty and kinematic contact were conducted for pipe *S*. The force-outer displacement curves for both methods are shown in Fig. 8.24a. The response with kinematic conatct was noisy and terminated earlier than the one with penalty contact. These curves also underestimated the response from the experiment.

(a) *Force - outer displacement for pipe L*   **(b)** *Force - inner displacement for pipe L*
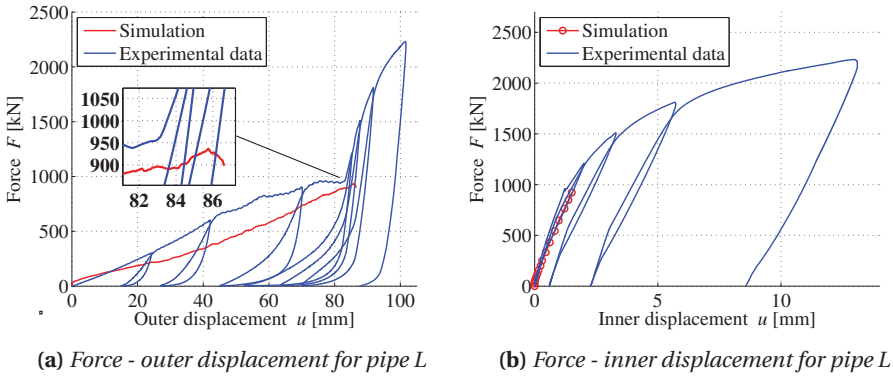
Figure 8.23: *Force - displacement curves for pipe L.*

(a) *Force - Outer displacement for pipe S*   **(b)** *Force - inner displacement for pipe S*
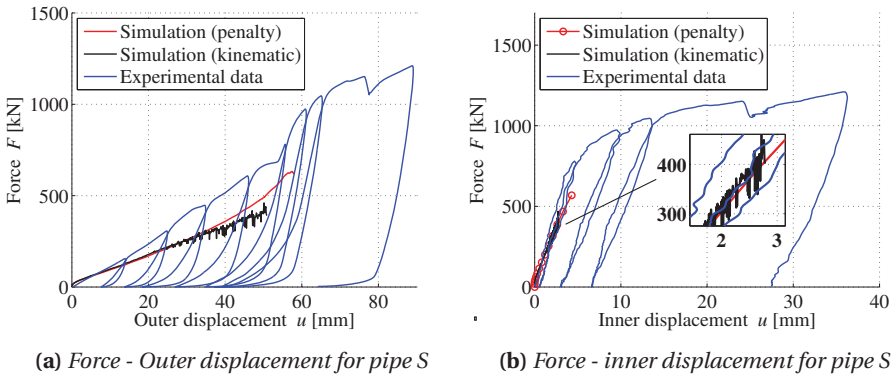
Figure 8.24: *Force - displacement curves for pipe S.*

8.4   Concluding Remarks

Finding a satisfactory numerical model in Abaqus/Explicit for the pipes with coating proved to be very difficult. Several weeks were spent and around 60 simulations were done trying to find a good model. The simulations each took from 1 to 4 hours. Parameters were constantly adjusted to find better solutions. All simulations were run on the computer cluster Snurre with 6 CPUs, except for a few that ran on NTNU's su-

percomputer Vilje, with 16 CPUs. However, Vilje did not give any significant gain in CPU-time.

The main problem was distortion of elements from contact issues. How to prevent the coating from penetrating the indenter remains unknown. A possible way might be to divide the coating and steel, and use a tie constraint. This way, surfaces can be created both between the coating and the indenter, but also between the coating and the steel. Maybe contact can be more easily described and defined this way.

The response from the simulations underestimated the response compared with the experiments. The material model was created on a basis of pipe *S*, and some deviation was expected for pipe *L*. However, not to this extent. In the reports provided by Statoil ([31], [37]), the correlation between the experiments and the numerical analysis was good, compared to the correlation obtained in this thesis. The material model in the report was established using the same approach, as well as the same finite element techniques. The reason that the same approach did not yield a good correlation in this case is unknown. However, the simulations of the coating sandwiches indicated that the material model did indeed underestimate the coating resistance. Since the factorial design in Chapter 7 showed that whether the inner solid PP layer and the outer shield layer was a part of the model or not, it did not affect the strength significantly. Since the sandwich coating itself underestimated the resistance, it may have affected the global response in the same way.

9 | Dent Estimations with DNV-RP-111

DNV-GL's recommended practice, DNV-RP-111 [9], offers a way to estimate the dent depth of a steel pipe from a trawl gear impact. However, this only applies to bare steel pipes or coated steel pipes where the coating is assumed stiffer than the steel, e.g. concrete coating. One of the motivations for this thesis, was to come closer to how softer coatings can be implemented in a recommended practice.

This chapter consists of two parts. First, a comparison between the dent depths of pipe S and L from the experiments and the ones estimated by DNV-RP-111 is given. Second, an idea of what a simple alternative model that includes the soft coating could look like is presented.

9.1 Estimations and Comparisons

In DNV-RP-111, the estimated permanent plastic dent depth, $H_{p,c}$, is estimated by subtracting the elastic dent depth, H_e, from the total dent depth (elastic and plastic), H_t.

$$H_{p,c} = H_t - H_e = D \cdot \left[\frac{F_{sh}}{m_p \cdot \alpha} \right]^{\frac{1}{\beta}} - \left[\frac{F_{sh}}{m_p \cdot 6 \cdot 10^3} \cdot \sqrt{\frac{D^3}{t}} \right] \tag{9.1}$$

F_{sh} is impact force experienced by the pipe. F_{sh} is based on the assumed energy transferred from the trawl gear to the pipe. It depends on the geometry, mass and velocity of the trawl gear. D is the pipe diameter and t is the pipe thickness. Eq. (9.1) is valid for pipes with $\frac{D}{t} < 50$. m_p is the moment capacity for a plate, calculated by:

$$m_p = \frac{1}{4} \cdot f_y \cdot t^2 \tag{9.2}$$

where f_y is the yield strength of the steel. α and β in Eq. (9.1), are constants calculated through the equations:

$$\alpha = 37 \cdot \left[ln\left(\frac{D}{t}\right) - \frac{1}{2}\right]$$ (9.3)

$$\beta = 0.125 \cdot \left[ln\left(\frac{D}{t}\right) + 1\right]$$ (9.4)

Fig. 9.1 indicates the deviation between the estimated total dent depth, H_t, and force-outer displacement from the experiments. The relation between the estimated force, F_{sh}, and H_t can be found from Eq. (9.1) and is expressed as:

$$F_{sh}(H_t) = m_p \cdot \alpha \left(\frac{H_t}{D}\right)^{\beta}$$ (9.5)

As seen in Fig. 9.1b, the DNV-RP-111 estimations correlate well with the experimental data up to approximately 20 mm for pipe S and 12 mm for pipe L. DNV-RP-111 only takes the initial geometry of the pipe into account, and this may lead to the deviation seen at large deformations. The numbers 1-6 in Fig. 9.1a is used later in this section and will be explained at that point.

(a) *Force - displacement for pipe S*

(b) *Force - displacement for pipe L*
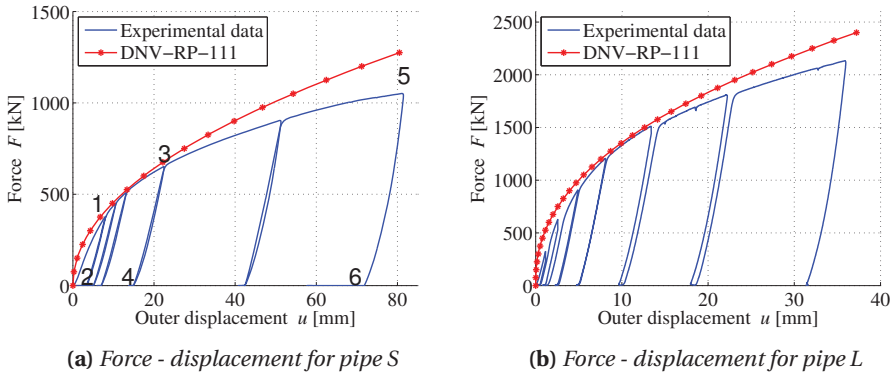
Figure 9.1: *Comparison of force-displacement from experiments and DNV-RP-111. Numbers 1-6 are positions where comparisons have been made, see the next sections and Table 9.1.*

The estimations from DNV-RP-111 gave a higher force for every displacement. This means that for a given amount of energy the pipe is suppose to absorb, the estimations from DNV-GL would give a non-conservative result, i.e. a smaller dent depth. However, impact events are dynamic events and the experiments done in this thesis are quasi-static. A dynamic test might render a curve above the estimations from DNV-RP-111.

The pipes were loaded in increments as indicated by the blue force-displacement curves in Fig. 9.1. The peaks of three increments are marked in Fig. 9.1a with numbers 1, 3 and 5. The forces and displacements were extracted from the blue force-displacement curve at these three points, and can be seen in Table 9.1. The estimated displacements at the same force levels were also found with DNV-RP-111. At the peaks, the deformation is

both elastic and plastic and can be estimated as the total dent depth, H_t. The result and the deviation from the experiments can be seen in Table 9.1.

At the bottom of a loading increment, the indenter applies no force to the pipe, i.e. F_{sh} is zero. Only plastic deformation is present in the pipes at this point. The three bottom points corresponding to the three peaks discussed in the paragraph above, are marked with the numbers 2, 4 and 6 in Fig. 9.1a. The deformation was extracted from the experiments and can be seen in Table 9.1. Since only plastic deformation is present here, the estimations through DNV-RP-111 were done by taking the total dent depth, H_t, corresponding to the force levels of 1, 3 and 5 and subtracting the elastic deformations, H_e, also corresponding to the force levels of numbers 1, 3 and 5. The full comparison can be seen in Table 9.1.

Table 9.1: *Experiments versus estimations using DNV-RP-111. Numbers 1-6 relate to force level at different positions in the blue curve in Fig. 9.1a.*

	Dent depths in pipe S			
#	**Force [kN]**	**Exp. [mm]**	**DNV-RP-111 [mm]**	**Δ [mm]**
1	380	8.1	6.9	1.2
2	0	3.3	3.9	-0.6
3	650	22.5	20.6	1.9
4	0	14.0	15.6	-1.6
5	1050	81.6	54.3	27.3
6	0	59	46.2	12.8

The results are the same as the graphical results from Fig. 9.1. The recommended practice works best at displacements up to approximately 15-20 mm (5-6 % of the steel diameter). They also indicated that the results correlate better after impact, when the force is zero and only plastic deformation is present. This comparison in Table 9.1 was only done using pipe S, but from the results in Fig. 9.1 it is assumed that the results would be more or less the same for pipe L.

9.2 Pipes with Soft Coating

As mentioned, the estimations done in the previous section only apply for bare steel pipes or coated steel pipes with coating stiffer than the steel, e.g. concrete. There are no existing recommended practice from DNV-GL on how to easily estimate the indentation of pipes with soft coating. When applying Eq. (9.5) on the coated pipes, the deviation was huge as indicated in Fig. 9.4. Bear in mind that applying this equation is mathematically wrong since it only takes information from the bare steel pipes into account. This is merely done to show what it would look like.

(a) *Force - displacement for pipe S with coating from experiments and DNV-RP-111*
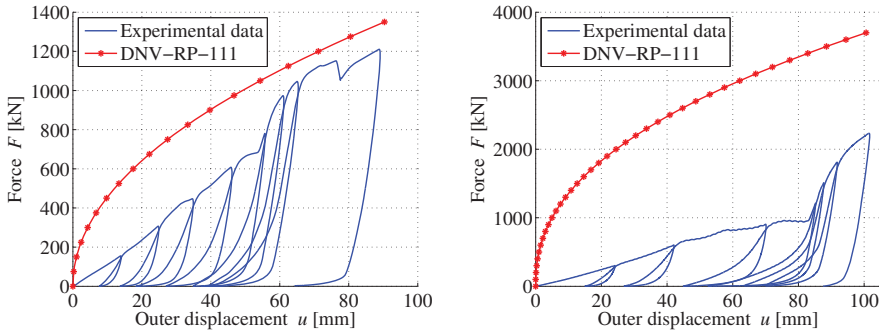
(b) *Force - displacement for pipe L with coating from experiments and DNV-RP-111*

Figure 9.2: *Comparison of force-displacement from experiments and DNV-RP-111.*

The reason that the deviation is smaller for pipe S than for pipe L probably comes from two things:

- The ratio $\frac{D}{t}$ is different for the two pipes. For pipe S, the ratio is $\frac{D}{t} = \frac{273.1}{14.3} = 19.1$. This is higher than the ratio for pipe L where $\frac{D}{t} = \frac{305}{25.5} = 11.9$. Higher ratio indicates a "softer pipe". This naturally makes the estimated force-displacement increase faster for pipe L.

- The fact that the thickness of the coating is much bigger for pipe L (80.9 mm vs 48 mm) gives the estimation of the force time to increase more.

Energy Measurements

The energy absorbed by a bare steel pipe is the area under the red estimation curves in the figures. In DNV-RP-111 it is given mathematically as:

$$E_{ab} = \int F_{sh} \cdot H_t \, dH_t \tag{9.6}$$

If the energy for a pipe with soft coating was to be calculated through integration by Eq. (9.6), the result would clearly be non-conservative. A different model estimating the energy absorbed by coated pipes is needed.

9.3 Simple Alternative Model

In this section, the ideas on how a simple alternative model could look like are presented. The alternative rheological model of the coated pipes is two separate springs working one at the time. First, only the stiffness from the coating gives any reaction force. The coating is eventually cut through, and the steel pipe is hit by the indenter. It is assumed that no force is transferred from the coating to the steel pipe.

I.e. the stiffness of the steel, K_{steel}, is assumed to be much higher than the stiffness of the coating, $K_{coating}$. So stiff that no deformation of the steel pipe happens during the indentation of the coating as indicated in Eq. (9.7). K_{tot} is the total stiffness and t_c is the coating thickness.

$$\frac{1}{K_{tot}} = \frac{1}{K_{steel}} + \frac{1}{K_{coating}} \approx \frac{1}{K_{coating}} \qquad [0 < H_t < t_c] \tag{9.7}$$

$$K_{tot} = K_{steel} \qquad [t_c < H_t] \tag{9.8}$$

This assumption is backed up by the fact that the inner displacement of the steel pipe is very small during the indentation of the coating. Fig. 9.3 shows the force-inner displacement for the coated pipes S and L. The red star indicates when the indenter hits the steel. This is found by plotting the load level at the distinct kinks that occur when the indenter hits the steel in Fig. 9.4.

(a) *Force - inner displacement for pipe S*   **(b)** *Force - inner displacement for pipe L*
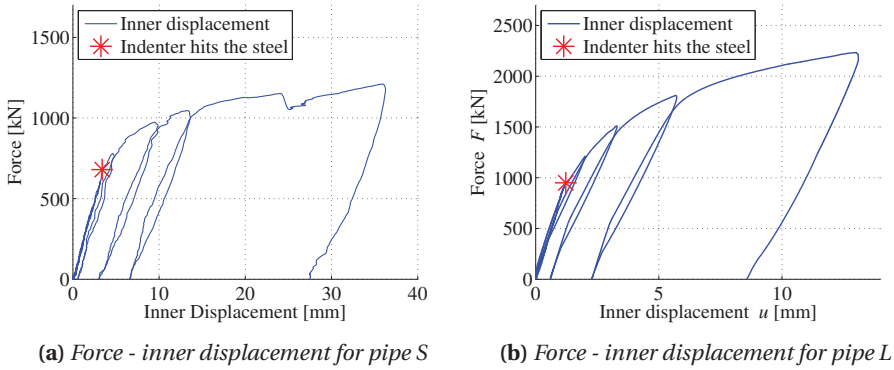
Figure 9.3: *Inner displacement in the coated pipes when the indenter hits the steel.*

As seen, the displacement is very small, 3.4 mm for pipe S and 1.2 mm for pipe L. It seems reasonable that pipe L has a smaller displacement since the $\frac{D}{t}$ ratio indicated that pipe L should be stiffer. Notice that pipe L is even subjected to a force of almost 250 kN more, at the time when the indenter hits the steel.

From the assumption of no deformation in the steel pipe during indentation of the coating, the total energy absorbed by the coated pipes, E_{tot} can be separated in two parts. Energy absorbed by the coating, $E_{coating}$, and the energy absorbed by the steel pipe, E_{ab}.

$$E_{tot} = E_{coating} + E_{ab} \tag{9.9}$$

The coating is assumed to work as a linear spring and the energy is thus estimated the following way:

$$E_{coating} = \frac{1}{2} \cdot K^*_{coating}(trawl, mat) \cdot H_t{}^2 \qquad [0 < H_t < t_c] \qquad (9.10)$$

where $K^*_{coating}(trawl, mat)$ is the perceived stiffness of the coating depending on the geometry, mass and velocity of the trawl gear, *trawl*, and the material properties, *mat*, of the coating. t_c is the coating thickness.

The steel is still assumed to work as a non-linear spring. However, it does not deform before the deformation is larger than the thickness of the coating. Mathematically, when $H_t > t_c$. The total energy is then estimated as:

$$E_{tot} = \frac{1}{2} \cdot K_{coating}(trawl, mat) \cdot t_c{}^2 + \int_0^{(H_t - t_c)} F_{sh}(H_t - t_c) \cdot (H_t - t_c) \, dH_t \qquad (9.11)$$

How this estimation could look like is illustrated in Fig. 9.4.
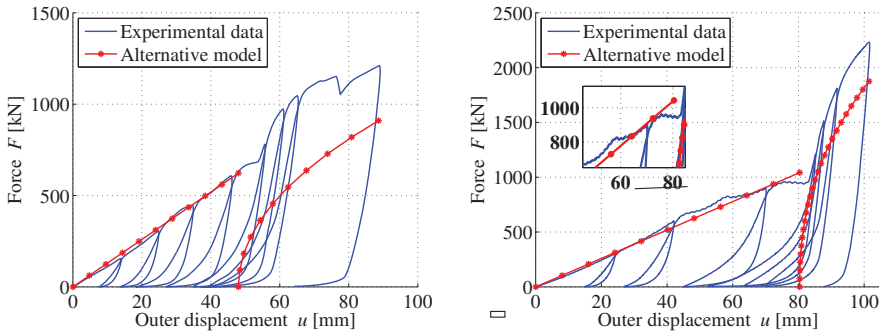
(a) *Alternative model for estimating the absorption of energy for pipe S*

(b) *Alternative model for estimating the absorption of energy for pipe L*

Figure 9.4: *Alternative models for estimating the absorption of energy.*

The $K^*_{coating}(trawl, mat)$ is in this thesis created to fit the experimental data for pipe *S*, however, the material properties for the coating of pipe *S* and *L* are nearly the same. The geometry and deformation speed of the indenter are also the same for the two pipes. For this reason, the $K^*_{coating}(trawl, mat) = 12.96$ is the same for the two pipes. It is therefore highly satisfying that the slope is spot on in *both* graphs. This may be another indication in favour of the assumption of no displacement of the steel, during the indentation of the coating. This parameter would be a problem to estimate in the case of lacking experimental data for different pipes.

Even though the displacements are very small, small displacements can yield large reaction forces in the steel. This is probably why the estimation of the energy of the steel is not particularly good. Pipe *S* is worse than pipe *L* and this may come from the fact that the displacement in the steel is larger in pipe *S*, recall 3.4 mm versus 1.2 mm for pipe *L*.

Adjusting the Alternative Model

It seems when assuming that F_{sh} starts at zero, the result is not satisfying. This especially goes for pipe S. Some amount of force, ΔF, is obviously transferred from the coating to the steel pipe. A way of estimating this ΔF, starts with plotting the force-inner displacements for the bare steel pipes from the experiments, see Fig. 9.5. Fig. 9.5a shows the force in pipe S without coating, when the inner displacement is $u = 3.4$ mm. Fig. 9.5b shows the force in pipe L without coating when the inner displacement is $u = 1.2$ mm. ΔF was found to be 250 kN and 400 kN for pipe S and L, respectively.

(a) *Force - inner displacement for pipe S without coating*

(b) *Force - inner displacement for pipe L without coating*
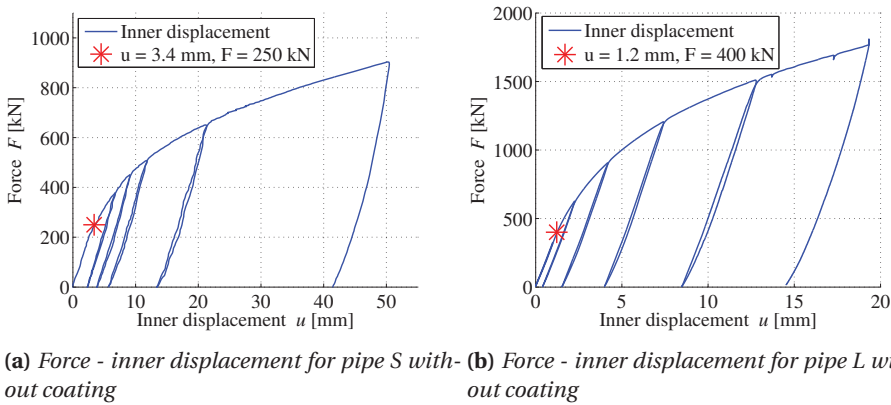
Figure 9.5: *Force - inner displacement of pipes without coating. Red start indicates force level for u=3.4 for pipe S and u=1.2 for pipe L.*

Fig. 9.6 shows how the adjusted models would look like.

(a) *Adjusted alternative model for estimating the absorption of energy (pipe S)*

(b) *Adjusted alternative model for estimating the absorption of energy (pipe L)*
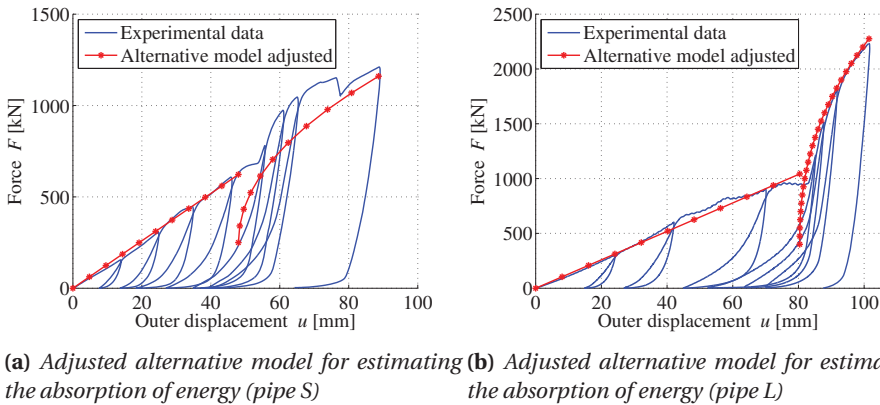
Figure 9.6: *Adjusted alternative models for estimating the absorption of energy.*

As seen, pipe S is still underestimating the steel somewhat, but pipe L is almost perfect. Finding ΔF would be a challenge without the experimental data. It might be possible to estimate it as a function of the $\frac{D}{t}$ ratio.

The energy equation for this adjusted model would be expressed as:

$$E_{tot} = \frac{1}{2} \cdot K_{coating}(trawl, mat) \cdot t_c^2 + \int_0^{(H_t - t_c)} [F_{sh}(H_t - t_c) + \Delta F] \cdot (H_t - t_c) \, dH_t \quad (9.12)$$

9.4 Concluding Remarks

DNV-RP-111 seems to estimate the energy from an impact with reasonable accuracy for moderate deformations.

The alternative models made in this chapter are meant as suggestions on how the basis for a model for pipes with soft coating could look like. There are probably other assumptions that need to be accounted for, and maybe it is more complicated than what is necessary. Still, a few results or maybe confirmations, can be seen in this chapter.

- The coating seemed more than soft enough for total stiffness equation, Eq. (9.7), to be a valid approximation, even though pipe S and pipe L had different $\frac{D}{t}$ ratios. However, for pipes with a higher $\frac{D}{t}$ ratio, the steel pipe might deform and effect the perceived stiffness of the coating to a higher extent.

- The stiffness of the seabed is not taken into account in the alternative models.

- It seems reasonable to model the coating as a linear spring, however, the geometry of the indenter may alter this.

10 | Discussions, Conclusions and Recommendations

10.1 Conclusions and Discussions

The conclusions presented in this section are based only on the few experiments conducted for this thesis. Several more experiments regarding the coating should be done before more resolute conclusions can be made.

Material tests indicated that:

- The steel from the seamless pipes is, as found by the previous theses, homogeneous across the cross-section and can be modeled as elasto-plastic with good results.

- True stress-true strain found when assuming volume preservation yielded a good result when simulating the material compression test of the PP foam. However, using this material model for the component tests did not yield good results. DIC is definitely recommended for future work.

The component tests showed that:

- The inner displacement is much smaller for coated pipes than uncoated pipes for an equal amount of energy absorbed by the pipes.

- Inner displacements of the pipes are almost negligible as long as the indenter is not in contact with the steel.

The Factorial Design indicated that:

- The material model based on the cylindrical compression tests of the PP foam was too weak. DIC should probably have been utilized. Deriving the true stress-true strain with the assumption of volume preservation is probably not the best solution.

- The factorial design method seems good at indicating main and interaction effects. However, it might give more interesting results for parameters that are not so obviously connected to the output. E.g. when increasing the hardening of the

coating specimen, it was logical that the total energy output increased accordingly.

- Modeling the coating as one layer seems to be a valid approximation. The strength did not increase notably when dividing the coating into three parts.

- Modeling the coating as three layers seemed to give a lateral displacement pattern more similar to the physical experiments. However, a higher friction coefficient between the coating and the steel in the numerical simulations may have altered this.

- All the numerical simulations experienced a larger maximum lateral displacement than the component from the experiments. This may be an indication that the assumption of volume preservation is not fortunate.

Numerical simulations showed that:

- The large deformation of the coating can create a lot of numerical problems.

- Contact issues between the indenter and coating was the main problem. This problem made the simulations terminate when the indenter hit the steel.

- ALE was of create advantage.

- ALE is not compatible with the general contact algorithm.

- The material model of the coating was too weak, as was also indicated when simulating the sandwich coating component.

- Using 16 instead of 6 CPUs did not speed up the numerical simulations significantly. The same simulation that took 2 hours and 22 minutes with 6 CPUs took 2 hours and 5 minutes with 16 CPUs.

Estimations with DNV-RP-111 showed that:

- The dent depth estimations for bare steel pipes corresponded well with the experiments, even though it overestimated the force somewhat. From displacement $u \approx 15$ mm the deviation got bigger. The overestimation may come from the fact that the impact is quasi-static in the experiments and not dynamic. The estimation only takes the initial geometry of the steel pipe into account. This may be a factor as well.

- The method was as expected not valid for the pipes with soft coating.

- The alternative model invented seemed to correspond with the experiments, especially for pipe L where the $\frac{D}{t}$ ratio is lower, indicating a tougher pipe.

- The initial response from the coated pipes followed the same linear slope both for pipe S and L. This indicates that only the geometry, mass and velocity of the indenter and the material properties of the coating affects this part of the force-displacement curve. I.e. the stiffness of the steel is so much higher than the stiffness of the coating that the $\frac{D}{t}$ ratio of the steel does not have a significant effect.

10.2 Recommendations for Further Work

There is a lot of work that can be done concerning the coating and coated pipes.

- Dynamic testing of pipes with coating was planned but not conducted due to postponed delivery of essential equipment. To know how the pipes absorb energy from a dynamic impact versus a quasi-static impact is of interest.

- An alternative material model for the coating should be applied. DIC is a recommended tool and anisotropy and volume change should be studied further. A fracture criterion is also of interest to employ.

- The numerical models in this thesis terminated when the indenter hit the steel. Creating a numerical model that is able to capture the force-displacement after this point should be made.

- Study of how a new recommended practice model can estimate the energy absorption and dent depth in pipes with soft coating would most likely be of interest for the industry.

- Experimental testing of the outer shield layer and inner solid PP layer to see what mechanical properties they might have. Factorial design could probably be a satisfying tool to find out how these layers interact with the foam.

- The pipes are welded together. These joints are of interest to examine concerning denting or impact.

- Study on how denting or impact affect the lifespan of the coated pipes in terms of incipient fracture and fatigue could be conducted.

References

[1] Small Gas Leak from Kvitebjørn Pipeline. http://www.statoil.com/en/NewsAndMedia/News/2008/Pages/gasleakkvitebjorn.aspx, 2015. Cited Date: [31 May 2015].

[2] K. Slåttedalen and A. Ørmen. Impact Against Offshore Pipelines. Master's thesis, Norwegian University of Science and Technology, 2010.

[3] J. Fornes and S. Gabrielsen. Impact Against Offshore Pipelines. Master's thesis, Norwegian University of Science and Technology, 2011.

[4] M. S. Hovdelien and V. Aune. Impact Against Offshore Pipelines. Master's thesis, Norwegian University of Science and Technology, 2012.

[5] T.I. Asheim and I. Mogstad. Impact Against Offshore Pipelines. Master's thesis, Norwegian University of Science and Technology, 2013.

[6] E. Jakobsen. Deformation of Pressurized Pipelines. Master's thesis, Norwegian University of Science and Technology, 2013.

[7] E. Digerud and K. Lofthaug. Bending of X65 Offshore Steel Pipes. Master's thesis, Norwegian University of Science and Technology, 2014.

[8] M. Kristoffersen. *Impact Against X65 Offshore Pipes*. PhD thesis, Norwegian University of Science and Technology, 2014.

[9] DNV-GL. Interference between Trawl Gear and Pipelines. *Recommended Practice DNV-RP-F111*, 2014.

[10] O.S. Hopperstad and T. Børvik. Lecture notes TKT4135 Mechanics of Materials. *Department of Structural Engineering, Norwegian University of Science and Technology*, 2014.

[11] A. Dahoun M. Ponçot, F. Addiego. True Intrinsic Mechanical Behaviour of Semi-Crystalline and Amorphous Polymers: Influences of Volume Deformation and Cavities Shape. *International Journal of Plasticity*, 40:126–139, 2013.

[12] T. Børvik. Lecture note TKT4135: The Tension Test. *Department of Structural Engineering, Norwegian University of Science and Technology*, 2012.

[13] S. Dey. *High Strength Steel Plates Subjected to Project Impact*. PhD thesis, Norwegian University of Science and Technology, 2004.

[14] G.E. Dieter. *ASM Handbook: Bend and Shear Testing Mechanical Behavior Under Tensile and Compressive Loads*, volume 8. AMS International, 2000.

[15] A. Dahoun M. Ponçot, F. Addiego. A Model of Ductile Fracture based on the Nucleation and Growth of Voids. *Acta Metallurgica*, 29:1509–1522, 1981.

[16] T. Børvik E. Fagerholt and O.S. Hopperstad. Measuring Discontinuous Displacement Fields in Cracked Specimens Using Digital Image Correlation with Mesh Adaptation. *Optics and Laser in Engineering*, 51:299–310, 2013.

[17] T. Børvik E. Fagerholt and O.S. Hopperstad. Investigation of Fracture in Small-Scale SENT Tests of a Welded X80 Pipeline Steel Using Digital Image Correlation with Node Splitting. *Engineering Fracture Mechanics*, 96:276–293, 2012.

[18] SIMULIA. Getting Started with Abaqus, 4.1.1. 6.14 Edition, 2014.

[19] SIMULIA. Abaqus Analysis User Manual, 27.1.4. 6.14 Edition, 2014.

[20] K. M. Mathisen. Lecture Notes TKT4197 Nonlinear Finite Element Analysis. *Department of Structural Engineering, Norwegian University of Science and Technology*, 2014.

[21] SIMULIA. Abaqus Analysis User's Guide, 12.2.3. 6.13 Edition, 2013.

[22] Lecture 4 - Contact. http://imechanica.org/files/l4-contact.pdf, 2015. Cited Date: [25 May 2015].

[23] SIMULIA. Abaqus Analysis User's Guide, 12.2.2. 6.13 Edition, 2013.

[24] B.C Koh and N. Kikuchi. New Improved Hourglass Control for Bilinear and Trilinear Elements in Anisotropic Linear Elasticity. *Computer Methods in Applied Mechanics and Engineering*, 65:1–46, 1987.

[25] SIMULIA. Getting Started with Abaqus, 9.6.1. 6.14 Edition, 2014.

[26] A. G. Hanssen, T. Auestad, T. Tryland and M. Langseth. The Kicking Machine: A Device for Impact Testing of Structural Components. *International Journal of Crashworthiness*, 8:385–392, 2003.

[27] A. Manes, R. Porcaro, H. Ilstad, E. Levold, M. Langseth and T. Børvik. The Behaviour of an Offshore Steel Pipeline Material Subjected to Bending and Stretching. *Ships and Offshore Structures*, 50:9–19, 2011.

[28] A. Ghiotti, S. Fanini, S. Bruschi and P.F. Bariani. Modelling of the Mannesmann Effect. *CIRP Annals - Manufacturing Technology*, 58:255–258, 2009.

[29] The Properties of Steel Grade X65. http://www.ehow.com/list_7492075_properties-steel-grade-x65.html. Cited Date: [27 May 2015].

[30] Polypropylene. http://en.wikipedia.org/wiki/Polypropylene. Cited Date: [26 May 2015].

[31] M.Polanco-Loria. Experimental Investigation of Indentation Problem on Steel Pipes with Polymeric Coating. *Internal Report, Statoil*, 2013.

[32] Thermotite - Polypropylene Insulation Systems. http://www.brederoshaw.com/solutions/offshore/thermotite.html, 2015. Cited Date: [24 May 2015].

[33] High Technology for Pipe Coating and Insulation. http://www.tenaris.com/shared/documents/files/CB804.pdf, 2015. Cited Date: [24 May 2015].

[34] A. Benallal O.S Hopperstad M. Fourmeau, T. Børvik. Anisotropic failure modes of high-strength aluminium alloy under various stress states. *International Journal of Plasticity*, 48:34–53, 2013.

[35] Hyperelastic Material. http://en.wikipedia.org/wiki/Hyperelastic_material. Cited Date: [22 May 2015].

[36] G. E. P. Box, W. G. Hunter and J. S. Hunter. *Statistics for experimenters*. John Wiley & Sons. Inc., 1978.

[37] H. Ilstad and J. Liu. Numerical Investigation on Indentation on Steel Pipe with Coating - Methodology and Techniques. *Internal Report, Statoil*, 2008.

[38] Minitab. http://www.minitab.com/en-us/, 2015. Cited Date: [04 June 2015].

[39] Lecture 9 - Damage and Failure. http://imechanica.org/files/l9-damage-failure.pdf, 2005. Cited Date: [22 May 2015].

[40] Lecture 2 - Elements. http://imechanica.org/files/l2-elements.pdf, 2005. Cited Date: [22 May 2015].

A | Pipe Measurements

The measurements and how they were conducted is the described in chapter 6. In this appendix the measured values are presented as a whole. The first number represent the pipe, whereas the latter number describes which end of the pipe.

It was conducted a study in the accuracy of the measurements by performing 30 measurements of the same thickness and diameter, respectively. The result is shown in Table A.1.
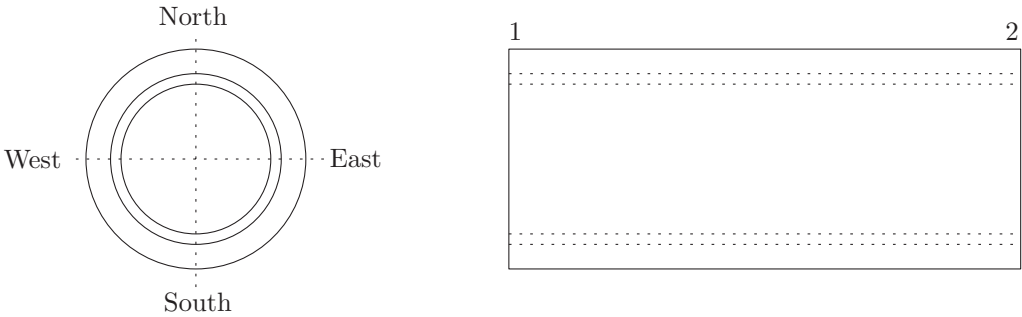
Figure A.1: *The locations where the measurements were taken.*

Table A.1: *Accuracy measurements.*

Test number	Thickness	Test number	Diameter
1	106.77	1	468.07
2	106.75	2	467.98
3	106.86	3	468.18
4	106.88	4	468.05
5	106.82	5	468.11
6	106.97	6	468.03
7	106.89	7	468.22
8	106.99	8	468.02
9	106.8	9	467.94
10	106.8	10	468.28
11	106.89	11	468.17
12	106.91	12	468.15
13	106.87	13	467.94
14	106.83	14	467.95
15	106.91	15	468.34
16	106.85	16	468.19
17	106.82	17	468.07
18	106.9	18	467.93
19	106.81	19	467.82
20	106.87	20	467.84
21	106.84	21	467.96
22	106.77	22	467.77
23	106.79	23	467.29
24	106.89	24	467.19
25	106.89	25	468.11
26	106.86	26	468.19
27	106.83	27	468.1
28	106.86	28	467.98
29	106.8	29	468.02
30	106.76	30	467.84
t_{avg}	106.85	D_{avg}	467.99
$Var(t)$	0.00339	$Var(D)$	0.06062
$Std(t)$	0.05825	$Std(D)$	0.24620

A.1 Steel Pipes without Coating

Table A.2: *Thickness of the steel pipes R1 and R2 mm.*

Pipe	North	South	East	West	Length [mm]	t_{avg} [mm]	Var (t) [mm^2]	St.Dev (t) [mm]
R11	13.87	15.12	14	15.11	1097			
R12	13.9	13.94	13.94	14.01	1097	14.24	0.26	0.51
R21	13.99	14.31	14.22	14.25	1101			
R22	14.3	14.09	14.31	14.75	1101	14.28	0.05	0.22

Table A.3: *Thickness the steel pipes R5 and R6 [mm].*

Pipe	North	South	East	West	Length [mm]	t_{avg} [mm]	Var (t) [mm^2]	St.Dev (t) [mm]
R51	25.33	25.05	25.06	24.65	999			
R52	24.7	25.24	25.31	25	999	25.04	0.07	0.26
R61	24.95	24.96	24.7	24.56	1005			
R62	25.12	24.68	24.43	24.77	1005	24.77	0.05	0.21

Table A.4: *Diameter of the steel pipes R5 and R6 [mm].*

Pipe	North-South	East-West	t_{avg} [mm]	Var (t) [mm^2]	St.Dev (t) [mm]
R11	274.13	274.20			
R12	273.67	274.01	274.00	0.06	0.24
R21	273.13	273.71			
R22	274.06	273.79	273.67	0.15	0.39
R51	305.84	305.50			
R52	305.74	305.09	305.54	0.11	0.33
R61	305.74	305.41			
R62	305.88	305.43	305.62	0.05	0.23

A.2   Steel Pipes with Coating

Table A.5: *Diameter of the coated pipes.*

| | D_{out} | | D_{inn} | |
Pipe	N-S	W-E	N-S	W-E
R31	369.06	369.83	245.41	244.98
R32	369.75	368.21	245.64	245.35
R41	368.86	371.7	245.62	245.09
R42	368.09	369.56	245.4	245.29
R71	466.62	468.75	256.59	255.89
R72	466.88	467.75	256.67	255.90
R81	466.21	465.36	255.18	255.02
R82	465.3	464.49	255.58	254.84

Table A.6: *Statistics for the coated pipes.*

| | D_{outer} | | | D_{inner} | | |
Pipe	D_{avg}	Var(D)	St.Dev	D_{avg}	Var(D)	St.Dev
R3	369.21	0.07	0.27	245.35	0.07	0.27
R4	369.55	2.41	1.55	245.35	0.05	0.22
R6	467.50	0.66	0.75	256.26	0.93	0.96
R7	465.34	0.17	0.42	255.16	0.49	0.70